NACA

RESEARCH MEMORANDUM

EXPERIMENTAL INVESTIGATION OF A FIVE-STAGE AXIAL-FLOW RESEARCH COMPRESSOR WITH TRANSONIC ROTORS IN ALL STAGES

IV - BLADE-ELEMENT PERFORMANCE

By Donald M. Sandercock

Lewis Flight Propulsion Laboratory
Cleveland, Ohio

NATIONAL ADVISORY COMMITTEE
FOR AERONAUTICS

WASHINGTON

May 7, 1957

NATIONAL ADVISORY COMMITTEE FOR AERONAUTICS

RESEARCH MEMORANDUM

EXPERIMENTAL INVESTIGATION OF A FIVE-STAGE AXIAL-FLOW RESEARCH COMPRESSOR WITH TRANSONIC ROTORS IN ALL STAGES

IV - BLADE-ELEMENT PERFORMANCE

By Donald M. Sandercock

SUMMARY

For analysis purposes as well as to provide a contribution to the growing body of information necessary for continuing improvement in the design system and understanding of the flow processes through multistage axial-flow compressors, the detailed blade-element performance of a five-stage axial-flow compressor is presented. The observed element performance for all rotor and stator blade rows is presented for three weight flows at five radial locations and speeds of 70, 80, 90, and 100 percent of design. The observed performance parameters are compared both with the design values and with quantities computed from more recent considerations of design variables. The stagewise progression of observed radial gradients of entropy is shown, and the effect of these gradients on the radial distribution of axial velocity and specific mass flow is considered.

Comparison of the observed performance at design speed with the compressor design values indicates that overcambering of the rotor blades and an excessive annulus area are instrumental in forcing the compressor to seek an equilibrium operating condition at a higher than design weight flow. Under these conditions, it is likely that the latter stages would stall before the compressor could be forced to operate at design weight flow. This conclusion verifies similar results obtained from considerations of stagewise variation of wall static pressures and individual stage equivalent performance curves. For convenience, the over-all compressor performance map and the individual stage equivalent performance curves are presented.

INTRODUCTION

In order to study some of the effects of combining stages with transonic rotor-inlet relative Mach numbers, a five-stage axial-flow compressor was designed and built at the NACA Lewis laboratory (ref. 1). Pertinent design values include a total-pressure ratio of 5 at a specific weight flow of 31 pounds per second per square foot of frontal area and an over-all efficiency of approximately 0.85. The feasibility of such a

design is reported in reference 2, which presents the over-all performance of the compressor when operated as a component of a current turbojet engine. At design speed the compressor produced design pressure ratio at a specific weight flow of 32 pounds per second per square foot of frontal area and an efficiency several points lower than the design value.

The next phase of this program was to obtain the detailed performance of each individual blade row. This was accomplished by running three series of tests, each covering a flow range from compressor choke to approximate compressor surge or limiting turbine-inlet temperature for tip speeds from 70 to 100 percent of design speed. Different stages were instrumented for each series. These interstage performance tests are described and the tabulated data obtained from the surveys are presented in reference 3.

The results of the latter phase of this investigation were intended to serve two purposes: (1) to analyze the flow occurring throughout this particular compressor, and (2) to contribute to a body of descriptive information applicable to multistage-compressor design. To achieve these aims, the detailed (blade-element) performance of each of the five stages is presented herein as radial variations of the conventionally used blade-element parameters. The observed parameters are compared with the values used in the compressor design (ref. 1) and also with values calculated from more recent design rules. Illustrations of boundary-layer correction factors and simplifying assumptions made to the equilibrium equations as applied to this particular compressor are presented.

SYMBOLS

A_F	compressor frontal area, 2.18 sq ft
c_p	specific heat at constant pressure
D	diffusion factor
g	acceleration due to gravity, 32.17 ft/sec^2
H	total or stagnation enthalpy
i	incidence angle, angle between inlet-air direction and tangent to blade mean camber line at leading edge, deg
J	mechanical equivalent of heat, 778.2 ft-lb/Btu
K_{bk}	weight-flow blockage factor
M	Mach number
N	rotational speed, rpm

[redacted]

P	total or stagnation pressure
p	static or stream pressure
R	gas constant, 53.35 ft-lb/(lb)(°R)
r	radius
S	entropy
s	blade spacing
T	total or stagnation temperature
U	rotor speed, ft/sec
V	air velocity, ft/sec
w	weight-flow rate, lb/sec
β	air angle, angle between air velocity and axial direction, deg
$\Delta\beta$	air turning angle, inlet-air angle minus outlet-air angle, deg
γ	ratio of specific heats
δ	ratio of total pressure to NACA standard sea-level pressure of 2116 lb/sq ft (or 29.92 in. Hg abs)
δ°	deviation angle, angle between outlet-air direction and tangent to blade mean camber line at trailing edge, deg
η	adiabatic efficiency
θ	ratio of total temperature to NACA standard sea-level temperature of 518.7° R
ρ	density
σ	solidity, ratio of chord to spacing
φ	blade camber angle, difference between angles of tangents to mean camber line at leading and trailing edges, deg
$\bar{\omega}$	total-pressure-loss coefficient

Subscripts:

a	stagnation conditions

[redacted]

4358

CJ-1 back

av	average
d	design value
e	equivalent, indicates that parameter to which it is affixed has been corrected to that which would be obtained at design speed
h	hub
id	ideal
k	known
M	momentum
m	measured value
m.a.	mass-averaged value
n	station number (fig. 1)
R	rotor
ref	reference
S	stator
t	tip
u	unknown
w	wake
wr	wake rake
z	axial direction
θ	tangential direction
0	bellmouth inlet (fig. 1)
1	compressor flow-measuring station
2	compressor first-rotor inlet
2-D	two-dimensional cascade value
3,5,7, 9,11	interstage measuring stations at exit of first, second, . . . fifth rotors (fig. 1)

[redacted]

4,6,8, 10,12 — interstage measuring stations at exit of first, second, . . . fifth stators (fig. 1)

∞ — free stream

Superscript:

' — relative to rotor

APPARATUS AND PROCEDURE

Experimental Procedure

The apparatus, instrumentation, and procedure used for these tests are described in detail in reference 3. Briefly, the five-stage 20-inch-diameter compressor was run as a component of a turbojet engine using ambient inlet conditions. Three series of tests were run during which a single stage or several stages were instrumented successively. By means of a variable exhaust nozzle, each series of tests covered a flow range from compressor choke to approximate compressor surge (or max. turbine-inlet temperature) for speeds of 70, 80, 90, and 100 percent of design. At equivalent speeds below 70 percent of design, increased compressor blade vibrations were observed, and extended operation in this speed range was deferred. Radii used in the radial surveys are listed in table I, and the axial locations of the radial surveys are shown in figure 1.

For use in appraising the reliability and accuracy of the data reported herein, the following curves are presented:

(1) Comparison of integrated weight flow at exit of each blade row with integrated weight flow at compressor-inlet flow-measuring station (station 1, fig. 1)(fig. 2)

(2) Comparison of mass-averaged temperature-rise and momentum efficiencies (fig. 3)

(3) Comparison of mass-averaged temperature ratios obtained across rotor with those measured across complete stage (fig. 4)

Calculations and Limitations

The equations used to compute the blade-element and over-all performance of the stages are presented in the appendix. The only departure from calculation procedures used in similar blade-element investigations is the method used to obtain average values of stator-outlet total pressures used in the calculation of stator blade loss coefficients. As

used herein, both an average free-stream and average stator-outlet total pressures are computed from the circumferential variation of total pressure obtained from a 19-tube wake rake (see ref. 3) according to the definition

$$P = \frac{\int_{\text{tube 1}}^{\text{tube 19}} P_{wr}\, ds - aP_c}{s} \tag{1}$$

where

P_{wr} pressures from wake rake

a difference between circumferential distance covered by wake rake and blade spacing ("a" varies with radius)

P_c average of several pressure probes located circumferentially about compressor at stator-discharge station

The average stator-outlet total pressure is obtained from equation (1) by integrating P_{wr} along the pressure values obtained in the wake, while the average free-stream total pressure is obtained from the same equation by integrating across the wake along a smooth faired curve connecting the free-stream values of pressure on the two sides of the wake. Figure 5 presents several examples of the circumferential variation of total pressure obtained from the wake rake illustrating the free-stream portions of flow on either side of the blade wake.

During the procuring and processing of this blade-element data, certain circumstances arose that tended to limit the amount and value of the results. Several of these are discussed briefly.

The compressor surge and choke limits restricted each individual blade row to operation over a relatively small portion of its flow range at a given speed, thus limiting the range of performance parameters as compared with that obtained from single-stage investigations. The range of operation of this compressor was further restricted at the higher compressor speeds, where a limiting turbine-inlet temperature was incurred before compressor surge (see ref. 2).

The computation of blade-element parameters requires the definition of a streamline across the blade row. Just as assumed in the design of this compressor (ref. 1), the airflow across each blade row was assumed to occur along conic surfaces, so that a streamline or blade element is defined by

$$\frac{r - r_h}{r_t - r_h} = \text{constant} \tag{2}$$

[redacted]

where r is the radius at which the streamline intersects the measuring plane. The flow parameter computed from data obtained at the intersection of the assumed streamline with the inlet and outlet measuring plane was then related to a given blade geometry.

The radial gradients of temperature and pressure observed in this investigation (ref. 3) suggest the possibility that mass-flow shifts which cause a deviation of the actual flow from the assumed streamline flow could result in an erroneous relation between the blade geometry and the airflow parameter. This type of error was investigated by comparing the assumed streamlines with those obtained from weight-flow considerations. The latter streamlines were obtained by computing the radial distribution of weight flow at each axial survey station as a percentage of the total weight flow integrated at that station. A so-called actual, or true, streamline was then assumed to intersect the measuring stations at the points of equal percentage of total weight flow. This procedure was carried out for a design-speed point, since at this speed the largest gradients of performance data were observed.

The differences between these two methods of computing streamlines were then used in conjunction with the data of reference 3 and the methods of reference 4 to obtain the effects on relative total-pressure-loss coefficients and efficiencies. The small changes in these performance parameters indicated that for this investigation radial mass-flow shifts could be neglected as a source of error.

In the calculation of the various blade-element parameters, it was tacitly assumed that the data used represent an average circumferential value. However, it is realized that, as the increased number of blade rows provide additional sources for accentuating the unsteadiness and circumferential variation of the flow, it becomes increasingly difficult to obtain average values of data with the type and number of instruments used in these tests (ref. 3). It cannot be determined at this time to what extent the observed data represent average circumferential values. This poses probably the most serious qualification of the performance data obtained downstream of the inlet stage.

PRELIMINARY CONSIDERATIONS

A multistage axial-flow compressor is evolved from the compounding of individually designed rotor and stator blade rows. The current method of designing an axial-flow-compressor blade involves a process of radially stacking individual airfoil shapes, or blade elements; and the proximity with which the actual performance approaches the design is contingent upon the accuracy with which the change in the velocity profile across each of these blade elements can be predicted. The basic information required by the design theory (especially for high inlet Mach number

stages) has been supplied principally from the observed flow characteristics measured in single-stage-compressor configurations. The significant blade-element performance parameters used both for analysis and to support the design theory employing this blade-element approach are discussed in detail in reference 5.

In addition to the blade-element data mentioned, the design technique utilizes certain assumptions and simplifications to permit solution of the fundamental flow equations. Reference 6 lists and discusses these simplifying assumptions in detail. In brief, reference 6 simplifies the calculation of the radial distribution of flow by considering conditions at axial stations between blade rows where equations for nonviscous axisymmetric flow are applied. Methods for considering the effects of wall boundary layers on required annulus area and mass-averaged stage performance are also presented.

Very little of the useful data available to the designer has been obtained from multistage-compressor investigations. Consequently, in the design of the intermediate and latter stages of a compressor, the designer has little experimental evidence from other than inlet-type stages to guide him in his choice of the quantitative values of the necessary design assumptions. The data presented herein provide the designer with one example of blade-element characteristics as observed through a multistage compressor and give some insight into the applicability of inlet-stage data to the analysis or design of later stages.

PRESENTATION OF RESULTS

Over-All and Stage Performance

For convenience, the over-all performance and equivalent stage performance plots are reproduced in figures 6 and 7. These results are discussed in detail in references 2 and 3, respectively.

Blade-Element Performance

Using the previously mentioned streamline definition and the data presented in reference 3, rotor and stator blade-element characteristics were computed for five streamline positions equally spaced across the passage. The blade-element characteristics chosen to present the detailed performance of each of the blade rows are listed in the following table:

Parameter	Rotor	Stator
Incidence angle, i	√	√
Deviation angle, δ°	√	√
Relative total-pressure-loss coefficient, $\bar{\omega}'_R$	√	
Wake and complete total-pressure-loss coefficient, $\bar{\omega}_w$ and $\bar{\omega}_S$		√
Diffusion factor, D (blade-loading parameter, ref. 7)	√	√
Ratio of outlet to inlet axial velocity	√	√
Inlet Mach number, M	√	√
Total-pressure ratio, P_n/P_{n-1}	√	
Adiabatic efficiency, η	√	
Work coefficient, $\Delta H/U_t^2$ (nondimensional temp. rise, appendix B of ref. 8)	√	

Because the restricted flow range of the individual blade rows precluded clear definitions of minimum-loss operating regions, the blade-element performance parameters are plotted against radius (or passage height) rather than in the conventional form as variations with incidence angle. Figures 8 and 9 present radial distributions of these parameters for the rotor and stator blade rows, respectively, of all stages at corrected rotor tip speeds of 70, 80, 90, and 100 percent of design. The three compressor modes of operation represented by the three points at each radial position are (1) maximum weight flow (open exhaust nozzle or min. back pressure), (2) near maximum compressor efficiency, and (3) minimum attainable weight flow (near compressor surge or max. turbine-inlet temperature).

For comparison and for aiding the blade-row performance analysis, the following quantities are included where applicable in figures 8 and 9:

(1) Design values (ref. 1)

(2) Minimum-loss incidence angles and deviation angles computed from recently developed design rules of reference 9

The methods of reference 9 for both minimum-loss incidence angles and deviation angles involve the computation of an angle based on low-speed two-dimensional-cascade data ($i_{2\text{-}D}$ and $\delta^{\circ}_{2\text{-}D}$) and a correlation between these values and those observed in a three-dimensional-compressor

[redacted]

environment. Because of the small amount of data from stator blades with circular-arc mean lines, the stator correlations are very incomplete; and, consequently, only the $i_{2\text{-}D}$ and $\delta^{o}_{2\text{-}D}$ for the stator blades can be presented.

Another method, known as Carter's rule (ref. 10), has been widely used for computing deviation angles. For the blades used in this compressor, deviation angles computed by Carter's rule proved to be very close to those obtained from the method of reference 9 (max. difference less than 2^{o} for both rotors and stators); consequently, only the latter are presented.

Figures 10(a) and (b) present, respectively, rotor and stator blade camber angles. These values may be used in conjunction with the incidence and deviation angles of figures 8 and 9 to obtain any desired air-turning angles.

Figure 11 shows circumferential variations of stator-discharge total pressure obtained from the wake rake at radial positions near the compressor hub, illustrating the regions of increased total-pressure loss found at this location.

The compounding effects of the individual blade-row performance at design speed are summarized in figure 12 by a comparison of the design and measured over-all performance from the compressor inlet to the exit of each successive blade row. Over-all total-pressure ratio, total-temperature-rise ratio, total-density ratio, and axial velocity ratio are presented at three radial positions (near tip, mean, and near hub) and compared with design values. Also, since the design stator-exit flow was axial in direction and the measured stator-discharge angles were very close to the design, at the stator-exit stations a comparison of design and observed static densities is indicated.

For use in discussing considerations of boundary-layer corrections and simplifications of the equilibrium equations, figures 13, 14, and 15 present radial distributions of entropy, specific mass flow ρV_z, and a comparison of measured and computed axial velocities, respectively.

DISCUSSION OF RESULTS

In general, since the curves of figures 8 and 9 are self-explanatory and the individual blade-element parameters have been discussed rather completely in the numerous single-stage investigations, only general observations are made.

Rotor Blade-Element Performance

Losses and incidence angle. - Aside from three-dimensional end effects, the principal factors that influence the loss across an individual rotor blade element are listed and discussed in reference 5 as (1) incidence angle of the approaching air, (2) relative inlet Mach number (compressibility and shock losses), (3) blade loading, and (4) Reynolds number. For this investigation, which was conducted with ambient-air inlet conditions and which utilized large-chord blades in all stages, the Reynolds number based on the blade chord is generally above the values where losses associated with Reynolds number become significant.

In general, the loss levels of the inlet stages shown in figure 8 can be explained from some combination of the factors listed. For example, at design speed the tip regions of the first and second rotors (figs. 8(d)(1) and (2)) exhibit all the flow conditions that tend toward the incurrence of high losses, including (1) incidence angles below the computed minimum-loss incidence angle, (2) high inlet relative Mach numbers, and (3) for the second-rotor row, especially, high diffusion factors (blade loading). A comparison of these same regions at part speed demonstrates the drop in loss level as the factors influencing the losses reach less critical values.

An attempt to demonstrate the relative importance and to provide an estimate of the magnitude of normal-shock losses resulting from high surface Mach numbers is presented in reference 11, which employs a simplified two-dimensional method and a certain assumed wave pattern to compute blade surface Mach numbers. Assuming that the inlet flow conforms to the necessary conditions, calculations indicate that the inlet relative Mach number and blade camber combine to give a surface Mach number of approximately 1.6 at the tip blade element ($16\frac{2}{3}$ percent of passage height from the outer wall) of both the first- and second-rotor blade rows. At these Mach numbers, normal-shock losses alone become significant, in addition to the detrimental effect of the shock on the blade surface boundary-layer growth.

Additional factors that may tend to complicate the loss picture are the interaction effects and the losses associated with the decay of blade wakes from preceding blade rows. Consequently, downstream of the first stage, the losses observed across a given blade row may not be related entirely to the flow processes about a particular blade row. Reference 12 reports some of the interaction effects observed behind a single-stage rotor preceded by a set of inlet guide vanes. From the investigation reported herein, no results on these effects can be presented. However, a summary of observed blade-element losses from all stages at points near the computed minimum-loss incidence angle indicated that, at the measured blade-loading levels (diffusion factor), the measured losses

at all radii fell within the range of loss reported in reference 12. For this select group of points, tip-element inlet relative Mach numbers and diffusion factors ranged from 0.75 to 1.00 and from 0.35 to 0.58, respectively. One exception to this observation was the high loss measured at the tip element of the fourth stage at design speed. However, the large difference between the average total temperatures measured in the tip region at the rotor and stator outlets (see ref. 3) leaves the accuracy of the rotor loss coefficients computed for this point somewhat in doubt. Unfortunately, the majority of this summary data for blade elements operating in a minimum-loss incidence angle region was necessarily obtained from test points at lower than design speeds.

Deviation angle. - The importance of obtaining the correct flow directions at the outlet of each blade row (considered in terms of deviation angle herein) is aptly illustrated in reference 5. Quantitative values of the effects of an error in the blade-outlet flow angle (deviation angle) on energy addition and blade loading (diffusion factor) may also be computed from plots in reference 4. Both reports indicate the increased deviation-angle sensitivity as the relative Mach number (wheel speed) and relative air angles are increased.

At the time this compressor was designed, no rules for computing deviation angle were known that had been proved accurate for this type of design. Consequently, the design deviation angles were obtained from the small amount of available data from the original single-stage transonic compressor of reference 8 (see ref. 1).

Differences between the design and measured deviation angles at design speed in figure 8 give an indication of the overturning (blade overcambering) that would have occurred if design incidence angle had been attained. Actually, the amounts of overturning, or overcambering, indicated by figure 8 are probably low, since, if design incidence had been met, the losses and consequently the deviation angles would have been lower, approaching the values computed from the method of reference 9.

Since the deviation-angle rule of reference 9 was empirically obtained from data observed at a reference or minimum-loss incidence angle, a comparison of measured and computed deviation angles can be made only at this particular operating point. However, curves of reference 9 indicate that, for the solidities employed herein, at least in the low-loss range the change of deviation angle with incidence angle is expected to be very small. In general, figure 8 shows that, for all rotor rows and at all blade speeds, whenever the observed incidence angles were close to the computed minimum-loss incidence angles, the observed and computed deviation angles were approximately equal. This indicates that for this compressor the deviation-angle rule of reference 9 is applicable to all stages.

Although either deviation angle or turning angle can be used for analysis purposes, in some instances it may be desirable to know the turning angle. Using the values of incidence and deviation angles from figure 8 and camber angle from figure 10(a), any desired turning angle may be calculated from the equation

$$\Delta\beta' = \varphi + i - \delta^{\circ} \tag{3}$$

Blade loading. - The parameter used herein to indicate the level of blade loading is the diffusion factor D developed and discussed in reference 7 and defined by equation (A4) of the appendix. Curves from reference 7, which represent a correlation of data obtained from single-stage investigations where shock losses are not excessive, indicate that the rotor tip-region diffusion factor is the principal determinant of the blade-row efficiency. Values of tip diffusion factor of 0.35 to 0.45 have been used in design of transonic stages as approximate limiting values for acceptable tip-element efficiency (approx. 0.90 or greater).

Some evidence from other multistage-compressor investigations indicates that, for stages other than the inlet stage, good efficiency (0.90 or greater) was observed in the tip region for diffusion factors greater than 0.50. Similar examples may be noted in the data presented herein. In most of these examples, the measured incidence angle is near (within approx. 2°) the computed minimum-loss value for the tip section. At present, however, the data are insufficient to determine whether these examples represent something which is universal or fundamental in nature.

One precaution necessary when comparing tip-element diffusion factors with those obtained from other investigations is to compare the distances from the outer wall (usually designated in percent of passage height) that define the tip element. For the investigation reported herein, the blade element nearest the outer wall at which element performance is presented is $16\frac{2}{3}$ percent of the passage height, whereas the values of reference 7 were generally from 10 to 12 percent of the passage height from the outer wall.

Stator Blade-Element Performance

Losses and incidence angle. - The total-pressure loss associated with the subsonic flow across a stationary blade row is the result of two separate effects: (1) a total-pressure loss due to boundary-layer buildup on the blade surfaces (wake loss), and (2) a decrease in free-stream total pressure due to turbulent mixing of the air leaving preceding blade rows (free-stream loss). Because of the difficulty of experimentally determining an accurate free-stream total-pressure drop, only the portion of total loss from the blade surface boundary-layer growth was

considered in the analysis of the few sets of stator blades tested as a component of a transonic stage. However, as a step toward eventually obtaining a body of information on losses from which some insight into the prediction of free-stream (mixing) losses may be obtained, total, or complete, losses measured across a stator row were also computed.

The wake loss is computed from the difference between the average free-stream total pressure and the average total pressures at the stator outlet. A detailed description of the method used to compute these average total pressures at the stator-outlet stations is presented in the APPARATUS AND PROCEDURE section of this report. The total, or complete, loss across a stator row is defined as the difference between the average total pressures measured at the rotor- and stator-outlet measuring stations. For comparative purposes, these total-pressure losses are presented in figure 9 in terms of a total-pressure-loss coefficient (eqs. (A5) and (A6) of the appendix), defined as the ratio of loss to inlet dynamic head. At radii where the complete loss across the blade row was smaller than or equal to the wake loss, only the latter is presented.

In general, the flow range covered by the stator rows was not large enough to define minimum-loss incidence angles. However, the portion of the loss-against-incidence-angle performance curve on which each stator row is operating and the range of incidence angle over which the various stator rows must operate for the range of speeds covered in this investigation are indicated in figure 9. When considering any relation of range, incidence angle, and loss, the following design information of reference 1 should be recalled:

(1) The first two stages have a circular-arc mean line plus circular-arc pressure and suction surfaces. The maximum thickness occurs at the 50-percent-chord position for this type of blade.

(2) The last three stages were constructed using a circular-arc mean line and a modified 65-series thickness distribution. The maximum thickness of this type blade occurs at the 40-percent-chord position. All pertinent blade data are listed in reference 1.

An interesting feature noted during the surveys with the wake rake at radii near the compressor hub was the presence of regions of low total pressure (sometimes called "cores") located between the stator blade wakes. References 13 to 15 present and discuss in detail similar results observed in a compressor cascade. Figure 11 presents a number of examples of the circumferential variation of total pressure obtained from the wake at radii near the compressor hub. All stages had a moving wall except the fifth stage, which had a stationary hub.

[redacted]

Deviation angle. - As discussed in reference 1, the stator deviation angles were computed from an empirical rule based principally on the data obtained from a low-cambered and a high-cambered set of stator blades tested in conjunction with the transonic rotor of reference 8. One departure from the rule occurred when it was decided to reduce the solidity of the second-stage stator row by 10 percent; and, since this row of stator blades was well along in the design proceedings, new deviation angles (camber angles) were not incorporated. Use of the lower solidity would have raised the design deviation angles slightly at all radii.

At points of low loss or points near the computed minimum-loss incidence angles, a comparison of the deviation angles measured and those used in the design with those computed from methods of reference 9 ($\delta^\circ_{2\text{-}D}$) gave the following results:

(1) At tip element:

$$\delta^\circ_m > \delta^\circ_{2\text{-}D} \quad \text{by approx. } 3^\circ \text{ to } 4^\circ$$

$$\delta^\circ_d > \delta^\circ_{2\text{-}D} \quad \text{by approx. } 1^\circ \text{ to } 3^\circ$$

(2) At mean element:

$$\delta^\circ_m \approx \delta^\circ_{2\text{-}D}$$

$$\delta^\circ_d \approx \delta^\circ_{2\text{-}D}$$

(3) At hub element:

$$\delta^\circ_m < \delta^\circ_{2\text{-}D} \quad \text{by approx. } 2^\circ$$

$$\delta^\circ_d < \delta^\circ_{2\text{-}D} \quad \text{from approx. } 4^\circ \text{ in first to } 2^\circ \text{ in fifth stage}$$

At the hub element of the fourth and fifth stages these values were exceeded somewhat, possibly because the hub element of these stages extended into the low-energy (core) regions and affected the angle readings of at least some of the probes. For the reason mentioned earlier, the comparisons of the design deviation angle do not apply to the second stage.

Comparison with Design

The numerous operating points necessary to construct a compressor performance map were obtained by successively decreasing the engine

exhaust-nozzle area until either compressor surge or a limiting turbine-inlet temperature was encountered. Following this procedure with the engine operating at design speed, an equilibrium operating condition was reached at which the compressor produced the over-all design total-pressure ratio (also the limiting turbine temp.). This point, represented by the diamond-shaped symbols in figures 8 and 9, was selected for comparison with the values used in the compressor design (ref. 1).

In summary, at this particular operating point the over-all performance (ref. 2) showed that the compressor produced design total-pressure ratio (approx. 5) at a higher than design weight flow and a lower than design over-all efficiency. Some insight into the operation of the individual stages was gained from the outer-wall static-pressure variation (ref. 2) and from the equivalent stage performance curves presented in figure 7 and discussed in reference 3. The curves of figures 8 and 9 probe more deeply into the flow processes at this operating point by presenting the performance of a number of blade elements (or streamlines) along the radial height of each blade row.

First stage. - Equation (A3b) of the appendix presents the work coefficient (measure of the energy addition) as a function of the axial velocity ratio and turning angle for a given inlet relative air angle. Equation (3) then relates the turning to the incidence and deviation angles. With the higher than design weight flow passing through the compressor, the first-rotor blade row operated at a lower than design incidence angle. However, the reduction in turning resulting from the lower than design incidence angle is balanced by an overcambering of the blade (measured deviation angle lower than design), so that the resulting turning of the air and axial velocity ratio combine to produce approximately the design energy input at all radial locations.

The efficiency of a blade element is a function of both the magnitude of loss in total pressures across the element and the work input level. Since the blade row produced approximately the design work input, at all radii the element efficiency (and pressure ratio) varied according to the radial distribution of loss. In the tip region, the observed losses resulted in below design performance. Single-stage performance indicates the sharp rise in loss that occurs at high inlet Mach numbers and incidence angles below the minimum-loss point. Also, reference 11 points out the probability of shock losses resulting from high surface Mach numbers, which in the tip regions of this blade row were computed to be approximately 1.6. Further, reference 7 indicates that in the low-loss range of incidence angle the anticipated losses would be on the order of 0.05 to 0.08 for the diffusion factors computed in this region.

In the hub and mean regions the low losses that resulted in higher than design efficiencies and pressure ratios reflect the use of design blade-element efficiencies that were low. When compared with the tip region, these regions demonstrate the increase in low-loss range of incidence angle as the inlet Mach number was reduced.

A comparison of measured and design deviation angles at the stator-exit station indicates that the air was discharged axially at all radii.

Second stage. - The higher than design weight flow, an average density rise below design across the first stage, and some shifting of the weight flow resulted in the radial distribution of incidence angle and inlet relative Mach number for the second stage shown in figure 8. The axial velocity ratio was approximately equal to the design value at all radii. Consequently, the incidence and deviation angles (again indicating an overcambering of the rotor blades) combined to produce the indicated radial gradient of energy addition.

The high losses measured across the second-rotor blade row are not unexpected, since the same conditions that usually lead to the formation of surface shocks and separation noted for the first stage were also present in this stage. In addition, the blade overcambering caused high values of diffusion in the tip region, and some unknown quantities of measured loss due to interaction effects and mixing from the preceding stage may have been present. The efficiency was lower than design at all radii except in the hub region, while the pressure ratio, which depends upon the energy addition as well as the efficiency, showed a gradient from hub to tip somewhat similar to that of the work input.

Flow across the stator row indicates that the desired turning was not obtained from the mean to the tip section. Velocity-diagram analysis indicates that this lower than design stator-outlet angle has the effect of diminishing the energy input level of the succeeding rotor blade row. This is accomplished by decreasing both the rotor incidence angle (and consequently the turning) and, at the lower inlet relative air angle, the change in tangential velocity that can be obtained for a given amount of turning. Quantitative values of these effects may be computed from plots of reference 4. As noted earlier, since the solidity of this stator row was lowered without computing new camber angles, the solidity and design deviation angles are not compatible with the empirical rule used in the design (see ref. 1).

Third stage. - The higher than design weight flow, the below design performance in the inlet stages, and the below design turning in the second-stage stators all combine to force the third-stage rotor to operate at incidence angles lower than the design values except at the tip element. Deviation angles again indicate a slight overcambering of the blades and combine with the incidence angles and axial velocity ratio to produce a gradient of energy addition in the tip region. Except in the tip region, the energy addition is below the design value.

Losses showed a decreasing trend from tip to hub and in general were higher than would be anticipated for the measured diffusion factors based on single-stage experience (ref. 7). Inlet relative Mach numbers

were below the range in which shock losses reach significant values. The increased loss appears to result from rotor operation at incidence angles lower than the computed minimum-loss incidence angle at all radii. However, this rotor was preceded by two stages both of which operated away from their best operating region and as a result produced high losses, especially in the tip region. In such an environment, interaction effects and circumferential variations of flow may become significant. Since these latter effects could not be evaluated, no specific sources of loss are pointed out for this rotor. The combination of work input and efficiency resulted in pressure ratios below design except in the tip region.

Considering all the test points presented, it is evident that, although the work input and pressure ratio were below design over most of the passage height, the axial velocity ratio was approximately equal to or lower than the design value. This indicates that the area ratio across this stage was larger than necessary to obtain the design performance or that the observed efficiency is higher than the design value. Since the efficiency over the major portion of the blade height was approximately equal to or lower than design, the increased area ratio apparently resulted from the use of an excessive wall boundary-layer allowance in the design. This design accounted for the effects of wall boundary layers on required annulus area by use of a weight-flow blockage factor (see ref. 1). From previous transonic-compressor experience, a value of 0.95 was used at the outlet of the first stage and an approximately linear variation was assumed to 0.90 at the compressor discharge.

Observed stator deviation angles were very close to design values, indicating that axial discharge was achieved. Wake losses appeared reasonable at all radii.

Fourth stage. - Incidence angles entering the fourth-stage rotor row were approximately equal to the design values. Since the average performance thus far has been below design, this also is an indication of an excessive passage area. Although the blade overcambering, as indicated by the difference between the design and observed deviation angles, and a slightly higher than design axial velocity ratio have opposite effects on the work input across a blade element, a higher than design energy addition was produced at all radii, with an increasing gradient from hub to tip.

The high losses observed across the fourth rotor are difficult to explain. The difference in the level of total temperature measured at the rotor and stator outlets (see ref. 3 and fig. 4) immediately suggests either temperature measurement errors or the inability to obtain circumferentially averaged values of performance data at this stage and speed. Assuming the results of reference 7 are applicable to this high-hub-tip-ratio blade row, a comparison with the losses associated with the flow about the blade elements of single-stage compressors indicates that the

magnitude of the observed loss coefficients was unusually high. Interaction effects provide an additional possibility as a source of loss. However, in view of the doubtful nature of the temperature measurements, no direct source of loss could be defined.

Although the high losses resulted in efficiencies lower than the design values at all radii, the increased work input produced a higher than design pressure ratio at all radial positions.

4358

Across the stator row the wake losses appear reasonable, while deviation angles were slightly higher at the tip and slightly lower at the hub than the design values.

Fifth stage. - Except for the measured losses, the performance of the fifth stage paralleled that obtained in the fourth stage, with incidence angles equal to or slightly higher than design, overcambering of the rotor blades at all radii, and a higher than design energy addition at all radial positions.

CJ-3 hack

Losses measured across the fifth-stage rotor appear low. Reference 3 shows that average temperatures measured at the rotor and stator outlets exhibit little difference. Comparison of the observed results with the values of reference 7 indicates that the measured losses were lower than those anticipated from this compilation of single-stage results. Assuming that the data represent circumferentially averaged values, the performance of this stage indicates that for this compressor even at design speed the results of the reference 7 may be applicable to stages downstream of the inlet stage.

The efficiencies were above design at all except the hub streamline, and pressure ratios were above design at all radial positions.

Summary remarks. - An over-all picture of the operation of this compressor at design speed and design pressure ratio is presented in figure 12. These over-all performance results are presented for three radial locations as the ratios of total pressure, total-temperature rise, total density, and axial velocity at successive measuring stations to their respective values at the compressor inlet (station 2).

Figure 12 indicates (1) that a radial gradient of energy addition was initiated in the second stage and maintained or slightly accentuated in the remaining stages, (2) that the stagewise distribution of the average over-all total-pressure ratio fell below design in the first three stages, but through the efforts of the exit stages attained the design level, and (3) that, in spite of the average lower than design values of total pressure and total density (which, where the velocities were of the order of magnitude of the design values, are indicative of static densities), averaged axial velocity from the second-stage exit

approached the design value and was lower than the design value at the compressor discharge. This stagewise distribution of axial velocity could only occur if the passage area over a portion of the compressor was larger than necessary. The indication of excessive flow area is further strengthened when it is recalled that a higher than design weight flow was obtained.

In summary, a comparison of the blade-element and over-all performance with the design indicates that, as reported in references 2 and 3, it is highly unlikely that this compressor could have operated at design weight flow. The increased performance of the inlet stages resulting from closer to design values of incidence angle and the overcambered blade sections coupled with the excessive values of passage area in the latter portion of the compressor would probably have forced the latter stages to operate at stalling angles of attack.

On the other hand, it may be speculated that, if the inlet stages had attained design incidence angles at design speed, these stages would have been forced to operate farther over on the stall portion of their performance curves (fig. 7) at the lower off-design speeds and may have made acceleration of the engine through these lower speeds questionable.

Comparisons of the measured incidence angles with the computed minimum-loss incidence angles verify the result concluded from the data of references 2 and 3 that the best matching of all stages occurred at some point between 80 and 90 percent of design speed.

Considerations of Boundary-Layer Blockage Effects

Since the design procedure involves the determination of velocities from the inner to the outer wall of the annular flow area, the incorporation of the effects of wall boundary layers into an accurate design system has long been a much sought after but elusive goal. Reference 6 discusses this problem in some detail and presents several methods of including the effects of the wall boundary layers in the design technique. In brief, these techniques involve the use of a radial distribution of loss, or entropy, from the inner to the outer wall, or the application of "gross" correction factors to correct for the effects of wall boundary layers on required annulus area and mass-averaged performance. Both of these techniques suffer from a lack of experimental results, especially from multistage compressors.

Entropy gradient. - To illustrate the stagewise progression of the radial distribution of entropy, figure 13 presents the radial variations of entropy measured behind the various blade rows of the five-stage axial-flow compressor. The entropy variations are plotted as the difference between the entropy at the exit of each blade row and the

entropy at an upstream reference point, which for this investigation was chosen as the inlet to the compressor (station 2). Entropy variations throughout the compressor are presented for operation near peak compressor efficiency for speeds of 80 and 90 percent of design and at design speed.

Weight-flow blockage factor. - The design of this compressor (see ref. 1) accounted for the effects of wall boundary layers on the required annulus area by utilizing a weight-flow blockage factor. This is one example of the uses of the gross correction factor discussed in reference 6. This technique considers the flow passage to be composed of a main or free-stream region and small boundary-layer regions at the inner and outer walls. An ideal weight flow is computed by extrapolating the free-stream values to the wall boundaries. The actual weight flow is then related to the ideal weight flow by means of the blockage factor K_{bk}. It should be noted that only blade-element losses are considered in the computation of free-stream conditions; thus, the blockage factor bears no relation to the free-stream efficiencies. The design recognized that, while this concept of the division of flow is probably satisfactory for the inlet stages, it may not be representative of the flow in the later stages. However, for simplicity, the concept was applied to the design of all the stages.

The radial distributions of specific mass flow ρV_z are presented in figure 14. As suggested in reference 1, figure 14 illustrates the tendency of the ρV_z product to approach a more parabolic form as the flow area decreases and the viscous effects extend over increasingly greater portions of the passage. At design speed the substantial gradient of loss, or entropy, produced in the inlet stages resulted in the formation of a parabolic form of radial distribution of ρV_z product in the second stage.

By use of the dashed lines shown in figure 14 as an extrapolation of free-stream conditions to the inner and outer walls, the following weight-flow blockage factors were computed for the first two stages:

$U_t/\sqrt{\theta}$, % design	Mode of operation	K_{bk} at station -			
		3	4	5	6
80	Near peak compressor efficiency	0.949	0.934	0.929	0.914
90	Near peak compressor efficiency	0.941	0.934	0.925	0.916
100	Design pressure ratio	0.937	0.945	0.943	0.942

It should be noted here that these values of blockage factor were obtained with the blade elements along the radial blade height of these several blade rows operating at various distances from their best operating regions. The values of blockage may have been lower with the blades operating closer to a minimum-loss region.

Summary remarks. - In view of certain limitations associated with the individual use of either entropy or gross correction factors to account for the wall boundary-layer effects, some combination of these methods may provide the design system with a satisfactory technique for predicting design requirements. Radial entropy variations over the major portion of the passage may be obtained from blade-element loss data. Examinations of measured entropy values across the passage from a number of compressors may then provide an empirical relation for extrapolating this variation to the inner and outer walls. However, a small gross correction may still be necessary to achieve the design weight flow. Unfortunately, the generalization of such a procedure for use in a design system would also require an examination of more extensive experimental results than are presently available.

Solution of Equilibrium Equation

The basic equations that apply to the flow of a real compressible fluid and the simplifying assumptions usually applied when considering the flow through an axial-flow compressor are discussed in reference 6. Several of these simplifications can be made in the radial-equilibrium equation that is used to compute the radial distribution of axial velocity. Both references 6 and 16 discuss these simplifications in some detail and indicate their fields of application. As explained in reference 6, the various forms of simplified-radial-equilibrium equations are (1) simple-radial-equilibrium equation neglecting entropy gradients, (2) simple-radial-equilibrium equation considering radial gradients of entropy, and (3) radial-equilibrium equation considering radial accelerations.

As an example of the effects of the various simplifications of the radial-equilibrium equation on the radial distribution of axial velocity, figure 15 presents a comparison at design speed of measured axial velocities with those computed (using the methods of ref. 16) from measured data and the equilibrium equations in forms (1) and (2). The difference between the measured axial velocities and those computed from the simple-radial-equilibrium equation considering radial gradients of entropy can be attributed to the neglect of the radial-flow term in the radial-equilibrium equation. As expected, neglect of the radial-flow term has a significant effect on the computed axial velocity only in the inlet stages (stations 3 and 5). The radial gradients of entropy associated with the axial velocity variations are shown in figure 13. Similar illustrations of the same effects computed from the results of other multistage-compressor investigations are recorded in reference 16.

CONCLUDING REMARKS

The need for more detailed measurements in multistage compressors both for use in the design systems and for an understanding of the internal flow in a multistage compressor is recognized. The material presented herein serves as one step toward filling this need. Since this is the observed performance of a specific compressor, no generalization can be made, or is intended, in this discussion. However, references that discuss the general aspects of the problems have been pointed out.

4358

As expected, certain limitations were encountered in securing and presenting the desired data. Some of these were noted, but not all could be evaluated at this time.

Because of the large amount of available reference material discussing specific blade-element parameters, only general remarks concerning the blade-element performance curves from this particular investigation were made. The rotor blade-element performance indicates

(1) Overcambering to some extent in all rotor blade rows

(2) Probable principal sources of loss observed at design speed in the first two stages, as evidenced by computed suction-surface Mach numbers of 1.6 along the tip element and a combination of high inlet Mach numbers and incidence angles below computed minimum-loss incidence angles, as well as large diffusion factors in the second-stage tip region

(3) For all stages, wherever the observed incidence angle was close to the computed minimum-loss incidence angle, measured deviation angles approximately the same as values computed from the latest design rule for deviation angle, and losses within the range of losses obtained from a compilation of inlet-type single-stage results.

The stator blade-element performance indicates

(1) With the exception of the second stage, measured deviation angles within approximately 2° of the design values at points showing a low loss, both design and measured deviation angles being from 1° to 4° higher at the tip and from 2° to 4° lower at the hub than deviation angles computed from a more recent design rule

(2) A division of stator losses into mixing and wake losses, although quantitative values for mixing losses show considerable scatter.

A comparison of the observed performance with design values verifies the conclusions reached from considerations of the stagewise variation of wall static taps and from individual equivalent stage performance curves. It appears highly unlikely that, with the overcambering of the rotor rows and an indication of an excessive annulus area, this compressor could have operated at design weight flow without blade stall in the latter stages. Unfortunately, a limiting turbine-inlet temperature prevented the compressor from operating any farther along its design-speed performance curve than the point at which design pressure ratio was obtained.

Lewis Flight Propulsion Laboratory
National Advisory Committee for Aeronautics
Cleveland, Ohio, February 15, 1957

APPENDIX - PERFORMANCE EQUATIONS

All equations used to compute the quantities presented in this report are listed in this appendix. The equations are developed and discussed in the references.

Blade-Element Computations

(1) Temperature-rise efficiency:

$$\eta = \frac{T_{n-1}\left[\left(\frac{P_n}{P_{n-1}}\right)^{\frac{\gamma-1}{\gamma}} - 1.0\right]}{T_n - T_{n-1}} \tag{A1}$$

(2) Rotor relative total-pressure-loss coefficient (ref. 12):

$$\bar{\omega}'_R = \left(\frac{P'_n}{P'_{n-1}}\right)_{id}\left\{\frac{1.0 - \left(\frac{P_n}{P_{n-1}}\right)\left(\frac{T_n}{T_{n-1}}\right)^{-\frac{\gamma}{\gamma-1}}}{1.0 - \left[1.0 + \frac{\gamma-1}{2}(M'_{n-1})^2\right]^{-\frac{\gamma}{\gamma-1}}}\right\} \tag{A2}$$

where

$$\left(\frac{P'_n}{P'_{n-1}}\right)_{id} = \left\{1.0 + \frac{\gamma-1}{2} M_R^2\left[1.0 - \left(\frac{r_{n-1}}{r_n}\right)^2\right]\right\}^{\frac{\gamma}{\gamma-1}}$$

For all computations used herein, $(P'_n/P'_{n-1})_{id}$ was taken equal to 1.0.

(3) Work coefficient (ref. 8):

$$\frac{\Delta H}{U_t^2} = \frac{gJc_p(T_n - T_{n-1})}{U_t^2} \tag{A3}$$

Equation (A3) can be written as a function of velocity-diagram parameters as

$$\frac{\Delta H}{U_t^2} = \left(\frac{r_{n-1}}{r_t}\right)^2 \left[\left(\frac{r_n}{r_{n-1}}\right)^2 - \left(\frac{r_n}{r_{n-1}}\right)\left(\frac{V_{z,n-1}}{U_{n-1}}\right)\left(\frac{V_{z,n}}{V_{z,n-1}}\right)\tan \beta_n' - \frac{V_{z,n-1}}{U_{n-1}} \tan \beta_{n-1}\right] \tag{A3a}$$

where n is the rotor-outlet station. For the special case of axial inlet flow which applies to the investigation herein, the work coefficient may be written in terms of axial velocity ratio, inlet relative air angle, and turning angle as

$$\frac{\Delta H}{U_t^2} = \left(\frac{r_{n-1}}{r_t}\right)^2 \left[\left(\frac{r_n}{r_{n-1}}\right)^2 - \left(\frac{r_n}{r_{n-1}}\right)\left(\frac{V_{z,n}}{V_{z,n-1}}\right)\frac{\tan (\beta_{n-1}' - \Delta\beta')}{\tan \beta_{n-1}'}\right] \tag{A3b}$$

(4) Rotor diffusion factor:

$$D_{R,n} = 1 - \frac{V_n'}{V_{n-1}'} + \frac{r_n V_{\theta,n} - r_{n-1} V_{\theta,n-1}}{(2\sigma_{av} r_{av})_R V_{n-1}'} \tag{A4}$$

(5) Stator total-pressure-loss coefficient (ref. 3):

(a) Wake loss:

$$\bar{\omega}_w = \frac{P_{n,\infty,av} - P_{n,av}}{P_{n-1} - p_{n-1}} \tag{A5}$$

(b) Stator total, or complete loss:

$$\bar{\omega}_S = \frac{P_{n-1,av} - P_{n,av}}{P_{n-1} - p_{n-1}} \tag{A6}$$

(6) Stator diffusion factor:

$$D_{S,n} = 1 - \left(\frac{V_n}{V_{n-1}}\right) + \frac{r_{n-1} V_{\theta,n-1} - r_n V_{\theta,n}}{(2\sigma_{av} r_{av})_S V_{n-1}} \tag{A7}$$

Mass-Averaged Computations

(1) Total-pressure ratio:

$$\left(\frac{P_n}{P_{n-1}}\right)_{m.a.} = \frac{\dfrac{\displaystyle\int_{r_{h,n}}^{r_{t,n}} \rho_n V_{z,n} r_n P_n \, dr_n}{\displaystyle\int_{r_{h,n}}^{r_{t,n}} \rho_n V_{z,n} r_n \, dr_n}}{\dfrac{\displaystyle\int_{r_{h,n-1}}^{r_{t,n-1}} \rho_{n-1} V_{z,n-1} r_{n-1} P_{n-1} \, dr_{n-1}}{\displaystyle\int_{r_{h,n-1}}^{r_{t,n-1}} \rho_{n-1} V_{z,n-1} r_{n-1} \, dr_{n-1}}} \tag{A8}$$

(2) Total-temperature ratio:

$$\left(\frac{T_n}{T_{n-1}}\right)_{m.a.} = \frac{\dfrac{\displaystyle\int_{r_{h,n}}^{r_{t,n}} \rho_n V_{z,n} r_n T_n \, dr_n}{\displaystyle\int_{r_{h,n}}^{r_{t,n}} \rho_n V_{z,n} r_n \, dr_n}}{\dfrac{\displaystyle\int_{r_{h,n-1}}^{r_{t,n-1}} \rho_{n-1} V_{z,n-1} r_{n-1} T_{n-1} \, dr_{n-1}}{\displaystyle\int_{r_{h,n-1}}^{r_{t,n-1}} \rho_{n-1} V_{z,n-1} r_{n-1} \, dr_{n-1}}} \tag{A9}$$

(3) Temperature-rise efficiency:

$$\eta = \frac{(T_{n-1})_{m.a.} \left[\left(\frac{P_n}{P_{n-1}} \right)_{m.a.}^{\frac{\gamma-1}{\gamma}} - 1.0 \right]}{T_{n,m.a.} - (T_{n-1})_{m.a.}} \tag{A10}$$

[redacted]

(4) Momentum-rise efficiency:

$$\eta_{O,M} = \frac{360gR\frac{\gamma}{\gamma-1}}{\pi N} \frac{(T_{n-1})_{m.a.}\left[\left(\frac{P_n}{P_{n-1}}\right)_{m.a.}^{\frac{\gamma-1}{\gamma}} - 1\right]}{\frac{\int_{r_{h,n}}^{r_{t,n}} \rho_n V_{z,n} r_n (r_n V_{\theta,n})\, dr_n}{\int_{r_{h,n}}^{r_{t,n}} \rho_n V_{z,n} r_n\, dr_n} - \frac{\int_{r_{h,n-1}}^{r_{t,n-1}} \rho_{n-1} V_{z,n-1} r_{n-1} (r_{n-1} V_{\theta,n-1})\, dr_{n-1}}{\int_{r_{h,n-1}}^{r_{t,n-1}} \rho_{n-1} V_{z,n-1} r_{n-1}\, dr_{n-1}}} \tag{A11}$$

Entropy

By the definition of stagnation conditions, stagnation entropy equals static entropy and is a function of stagnation pressure and temperature as follows (ref. 14):

$$S_n = S_{ref} + R \ln \left[\frac{\left(\frac{T_n}{T_{ref}}\right)^{\frac{\gamma}{\gamma-1}}}{\frac{P_n}{P_{ref}}} \right]$$

or, rearranging, as employed herein, with the compressor inlet (station 2) used as the reference station,

$$\frac{S_n}{R} - \frac{S_2}{R} = \ln \left[\frac{\left(\frac{T_n}{T_2}\right)^{\frac{\gamma}{\gamma-1}}}{\frac{P_n}{P_2}} \right] \tag{A12}$$

Simplified-Radial-Equilibrium Equation Including Entropy Gradient

The simplified-radial-equilibrium equation including an entropy gradient (ref. 14) is as follows:

[redacted]

$$V_u = \sqrt{\frac{V_k^2\left[1 + \left(1 - \frac{r_u}{r_k}\right)\sin^2\beta_k\right] + 2c_p(T_u - T_k) + \frac{\gamma-1}{\gamma}\left(\frac{S_k}{R} - \frac{S_u}{R}\right)\left[c_p(T_k + T_u) - \frac{V_k^2}{2}\right]}{1 - \left(\frac{r_k}{r_u} - 1\right)\sin^2\beta_u + \frac{\gamma-1}{2\gamma}\left(\frac{S_k}{R} - \frac{S_u}{R}\right)}} \quad \text{(A13)}$$

where c_p and R must have units of ft-lb/(slugs)($^\circ$R). A solution for the simplified-radial-equilibrium approximation may be obtained from equation (A13) by keeping the entropy constant radially (i.e., the term $S_k/R - S_u/R$ equal to zero).

4358

REFERENCES

1. Sandercock, Donald M., Kovach, Karl, and Lieblein, Seymour: Experimental Investigation of a Five-Stage Axial-Flow Research Compressor with Transonic Rotors in All Stages. I - Compressor Design. NACA RM E54F24, 1954.

2. Kovach, Karl, and Sandercock, Donald M.: Experimental Investigation of a Five-Stage Axial-Flow Research Compressor with Transonic Rotors in All Stages. II - Compressor Over-all Performance. NACA RM E54G01, 1954.

3. Sandercock, Donald M., and Kovach, Karl: Experimental Investigation of a Five-Stage Axial-Flow Research Compressor with Transonic Rotors in All Stages. III - Interstage Data and Individual Stage Performance Characteristics. NACA RM E56G24, 1956.

4. Jackson, Robert J., and Yohner, Peggy L.: Effects of Design and Measurement Errors in Compressor Performance. Ch. XVI of Aerodynamic Design of Axial-Flow Compressors, vol. III. NACA RM E56B03b, 1956.

5. Lieblein, Seymour: Review of High-Performance Axial-Flow-Compressor Blade-Element Theory. NACA RM E53L22, 1954.

6. Giamati, Charles C., Jr., and Finger, Harold B.: Design Velocity Distribution in Meridional Plane. Ch. VIII of Aerodynamic Design of Axial-Flow Compressors, vol. II. NACA RM E56B03a, 1956.

7. Lieblein, Seymour, Schwenk, Francis C., and Broderick, Robert L.: Diffusion Factor for Estimating Losses and Limiting Blade Loadings in Axial-Flow-Compressor Blade Elements. NACA RM E53D01, 1953.

8. Schwenk, Francis C., Lieblein, Seymour, and Lewis, George W., Jr.: Experimental Investigation of an Axial-Flow Compressor Inlet Stage Operating at Transonic Relative Inlet Mach Numbers. III - Blade-Row Performance of Stage with Transonic Rotor and Subsonic Stator at Corrected Tip Speeds of 800 and 1000 Feet Per Second. NACA RM E53G17, 1953.

9. Robbins, William H., Jackson, Robert J., and Lieblein, Seymour: Blade-Element Flow in Annular Cascades. Ch. VII of Aerodynamic Design of Axial-Flow Compressors, vol. II. NACA RM E56B03a, 1956.

10. Carter, A. D. S.: The Low Speed Performance of Related Aerofoils in Cascades. Rep. No. R.55, British NGTE, Sept. 1949.

11. Schwenk, Francis C., Lewis, George W., and Hartmann, Melvin J.: A Preliminary Analysis of the Magnitude of Shock Losses in Transonic Compressors. NACA RM E57A30, 1957.

12. Jahnsen, Lawrence J., and Fessler, Theodore E.: Experimental Investigation of Performance of Single-Stage Transonic Compressor with Guide-Vane Turning Counter to Direction of Rotor Whirl. NACA RM E57B04, 1957.

13. Dean, Robert C., Jr.: Secondary Flow in Axial Compressors. Gas Turbine Lab., MIT, May 1954.

14. Rohlik, Harold E., Kofskey, Milton G., Allen, Hubert W., and Herzig, Howard Z.: Secondary Flows and Boundary-Layer Accumulations in Turbine Nozzles. NACA Rep. 1168, 1954. (Supersedes NACA TN's 2871, 2909, and 2989.)

15. Herzig, Howard Z., Hansen, Arthur G., and Costello, George R.: A Visualization Study of Secondary Flows in Cascades. NACA Rep. 1163, 1954. (Supersedes NACA TN 2947.)

16. Hatch, James E., Giamati, Charles C., and Jackson, Robert J.: Application of Radial-Equilibrium Condition to Axial-Flow Turbomachine Design Including Consideration of Change of Entropy with Radius Downstream of Blade Row. NACA RM E54A20, 1954.

[redacted]

TABLE I. - RADII FOR RADIAL-SURVEY POSITIONS (REF. 3)

[Tip radius constant at 10 in.]

Radial position	Radius, r, in., at station -										
	2	3	4	5	6	7	8	9	10	11	12
1		9.900	9.900	9.900	9.900	9.900	9.900	9.900	9.900	9.900	9.900
2		9.850	9.850	9.850	9.850	9.850	9.850	9.850	9.900	9.900	9.900
3		9.650	9.600	9.650	9.700	9.750	9.750	9.750	9.800	9.800	9.800
4	9.167	9.250	9.350	9.450	9.500	9.600	9.600	9.650	9.700	9.700	9.700
5	8.750	8.850	9.000	9.200	9.300	9.400	9.450	9.500	9.550	9.550	9.550
6	8.334	8.500	8.700	8.900	9.050	9.150	9.250	9.350	9.400	9.400	9.400
7	7.501	7.750	8.050	8.400	8.550	8.750	8.850	9.000	9.100	9.100	9.100
8	6.668	6.950	7.400	7.850	8.050	8.350	8.500	8.650	8.850	8.850	8.850
9	6.251	6.600	7.050	7.550	7.850	8.150	8.300	8.500	8.700	8.700	8.700
10	5.835	6.200	6.700	7.300	7.600	7.900	8.100	8.300	8.550	8.550	8.550
11		5.900	6.550	7.150	7.450	7.800	8.000	8.200	8.450	8.450	8.450
12		5.700	6.350	7.000	7.350	7.700	7.900	8.150	8.400	8.400	8.400
Hub		5.456	6.064	6.764	7.102	7.502	7.720	7.976	8.114	8.250	8.250

4358

[redacted]

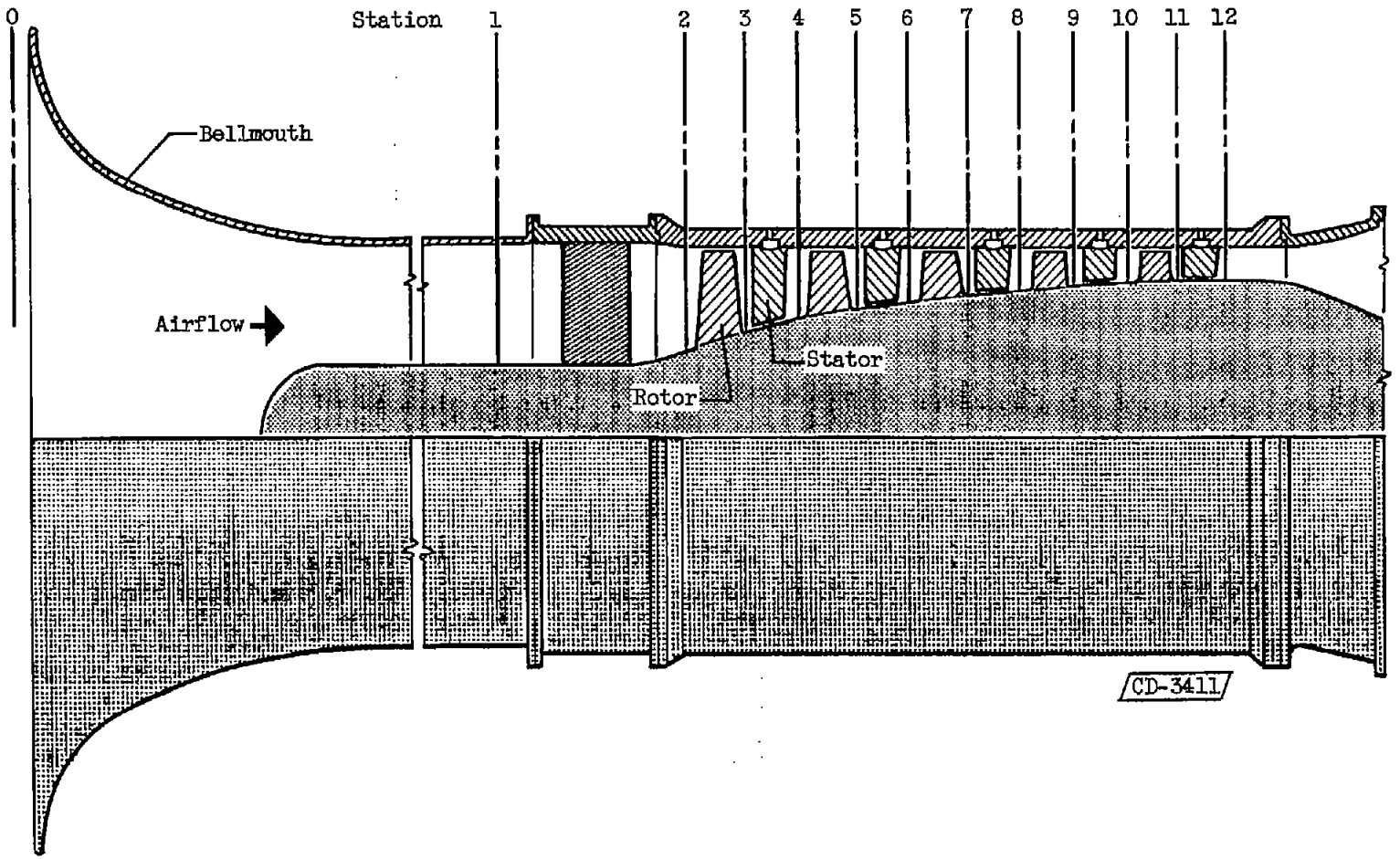

Figure 1. - Sketch of passage contour of five-stage axial-flow transonic compressor showing axial location of blade-row inlet and outlet stations.

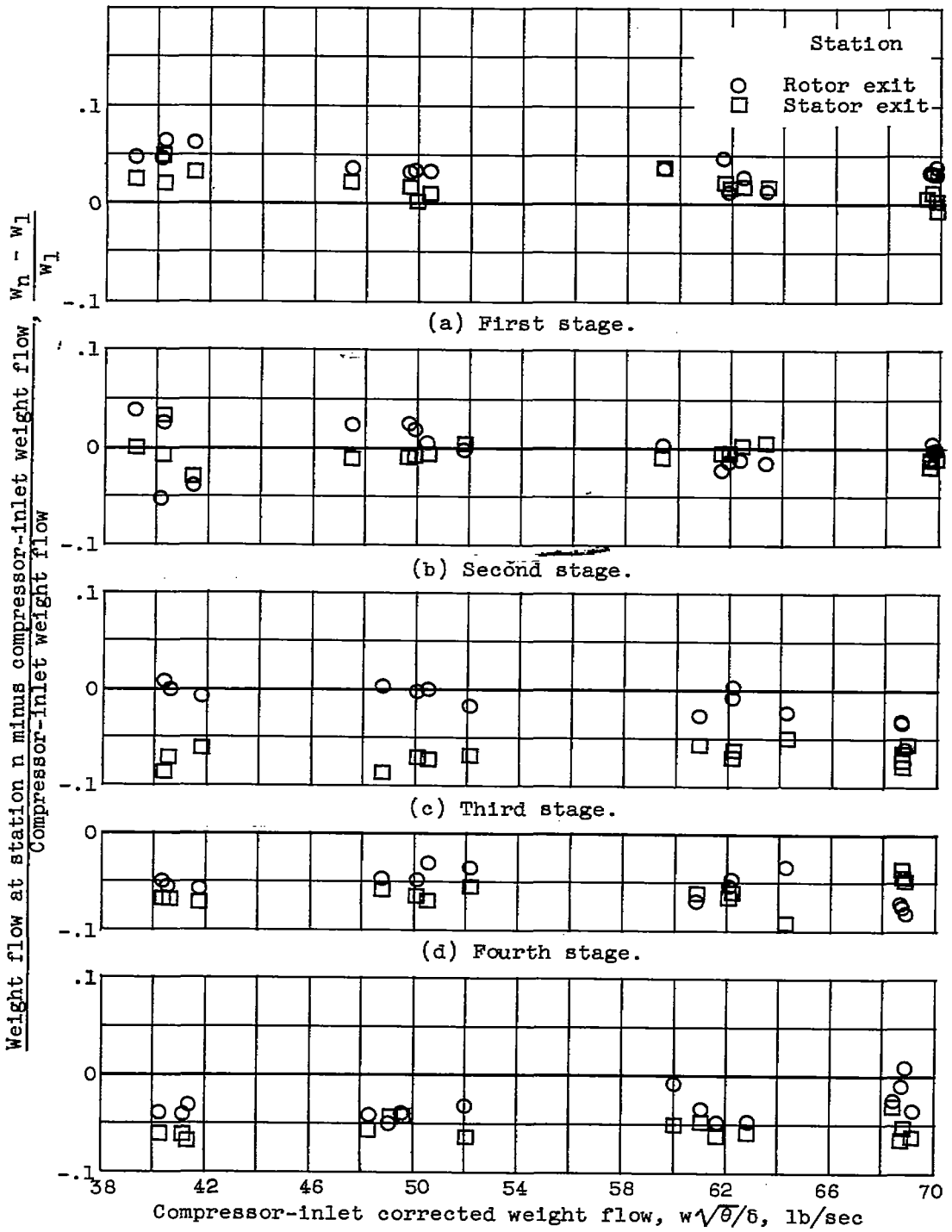

Figure 2. - Comparison of measured weight flows (ref. 3).

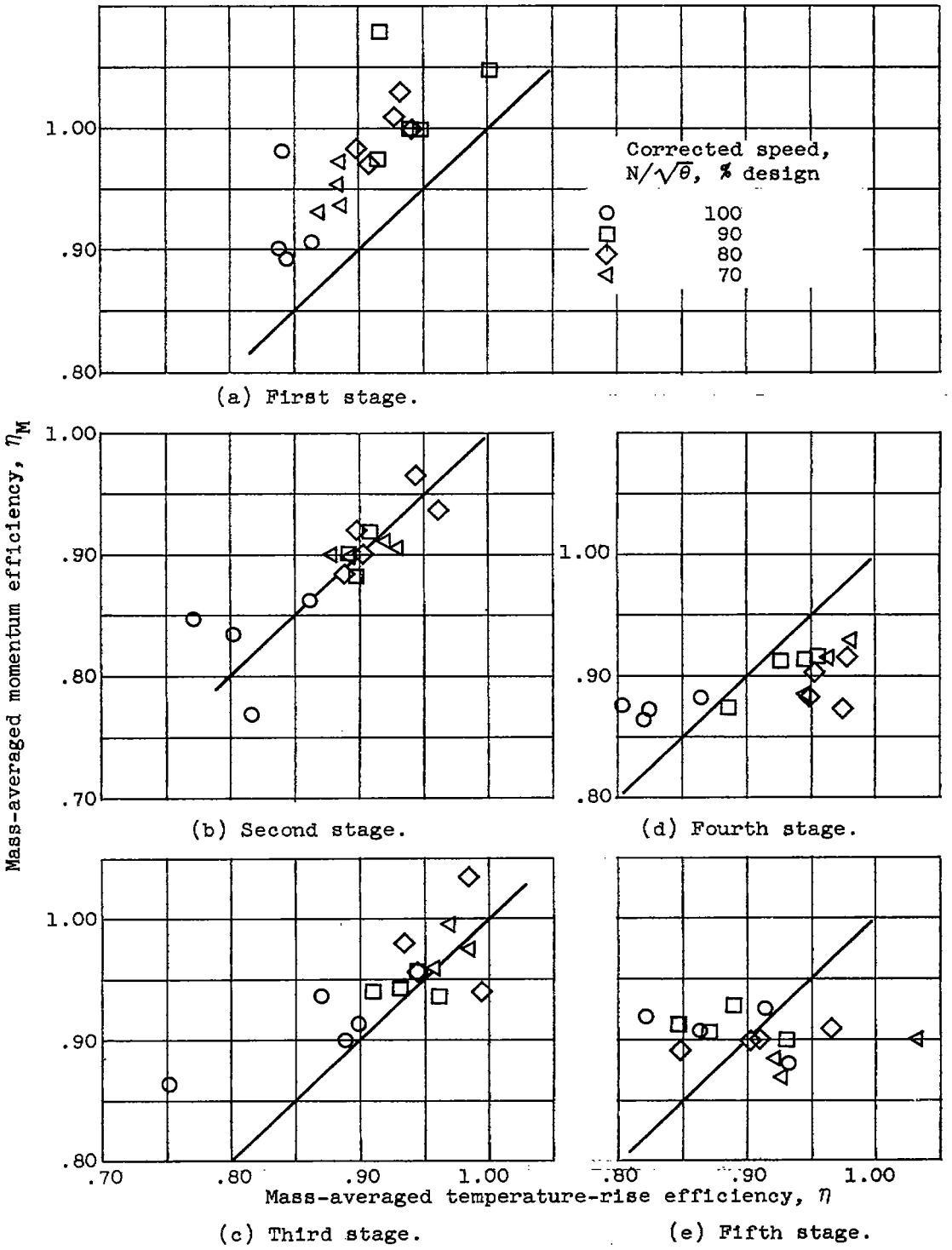

Figure 3. - Comparison of mass-averaged efficiencies (ref. 3).

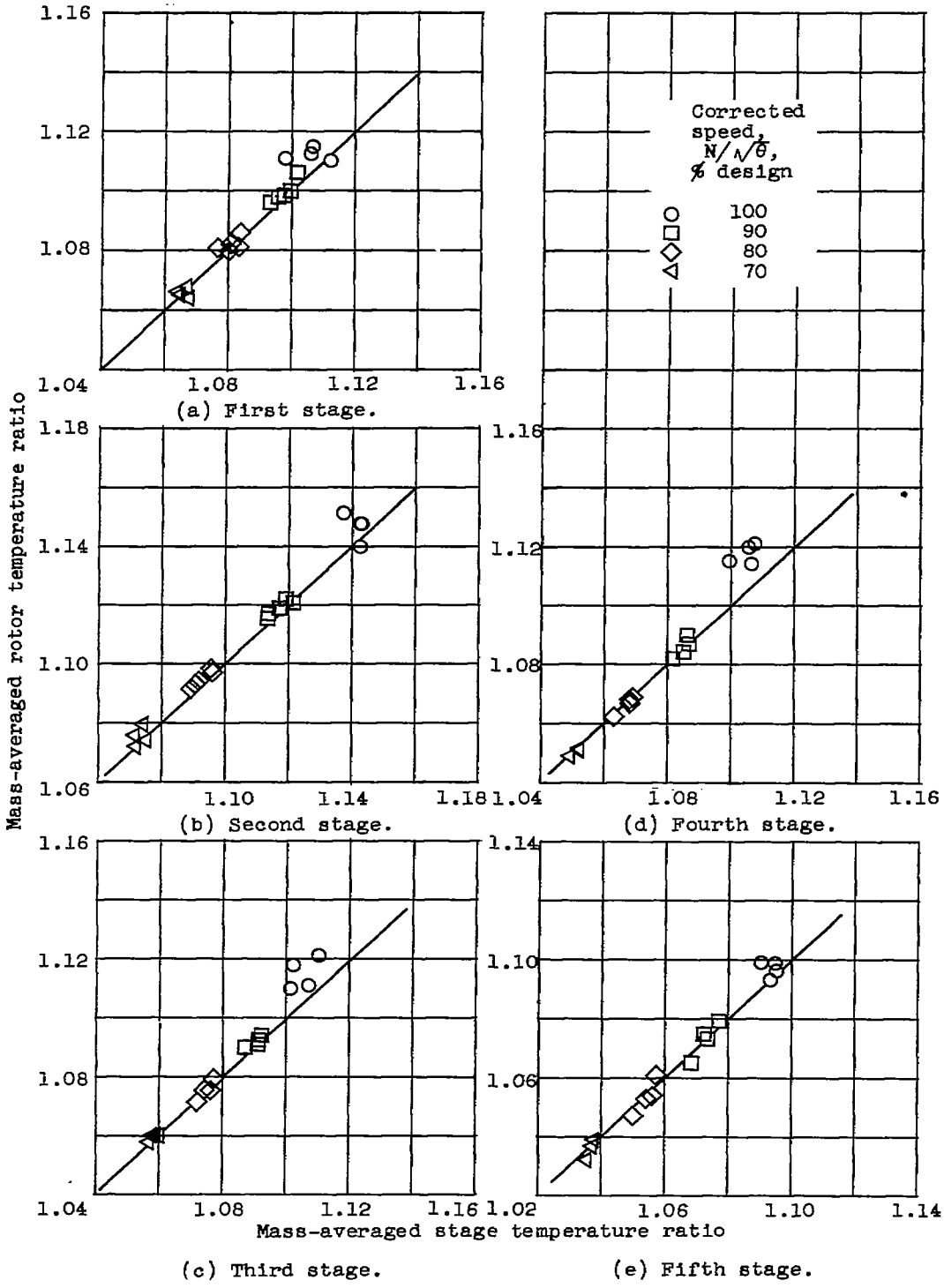

Figure 4. - Comparison of mass-averaged rotor and stage total-temperature ratios.

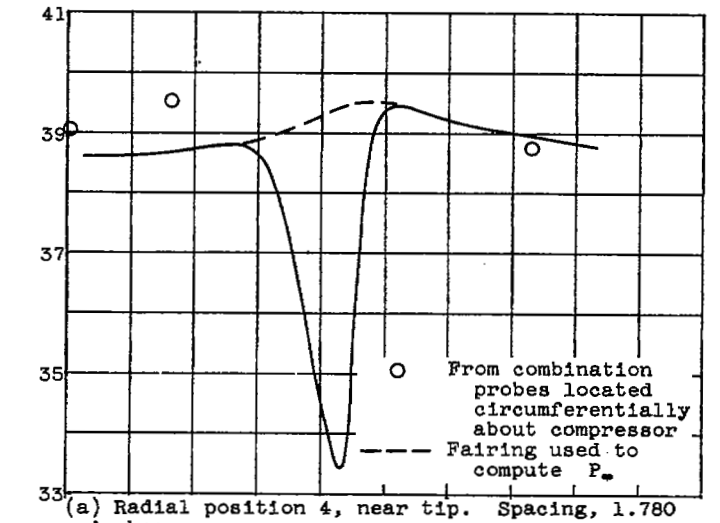

(a) Radial position 4, near tip. Spacing, 1.780 inches.

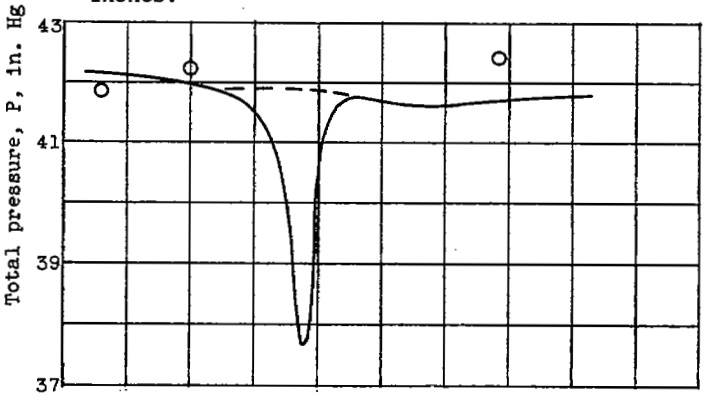

(b) Radial position 7, mean. Spacing, 1.533 inches.

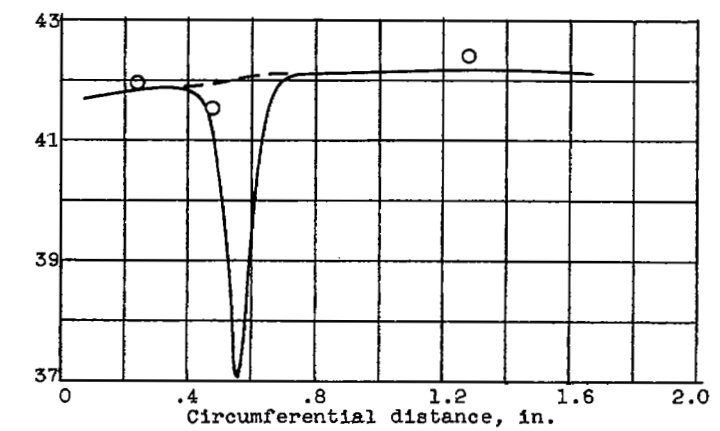

(c) Radial position 10, near hub. Spacing, 1.276 inches.

Figure 5. - Example of circumferential variation of total pressure measured on wake rake behind stator blade row.

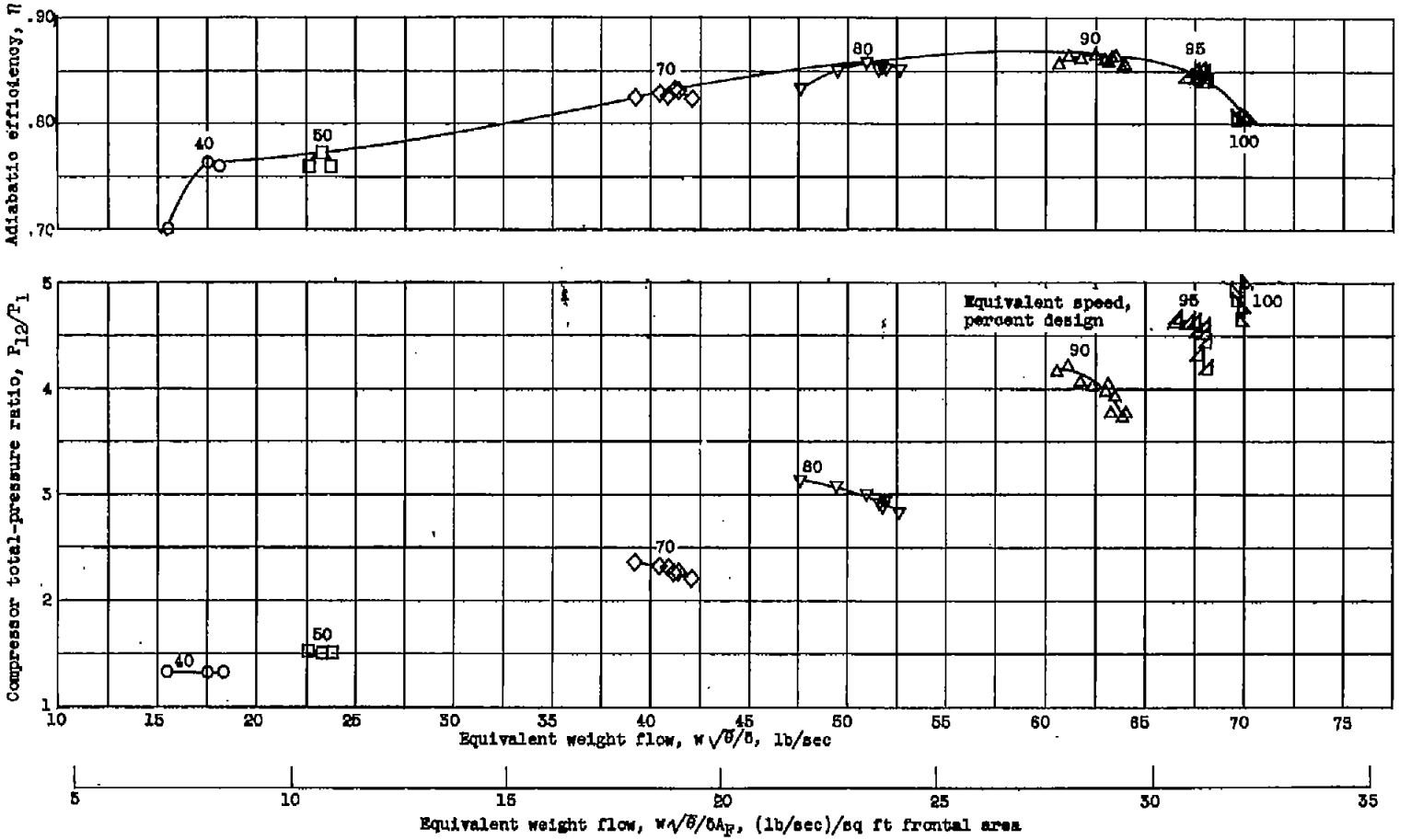

Figure 6. - Over-all performance characteristics of five-stage transonic compressor (ref. 2).

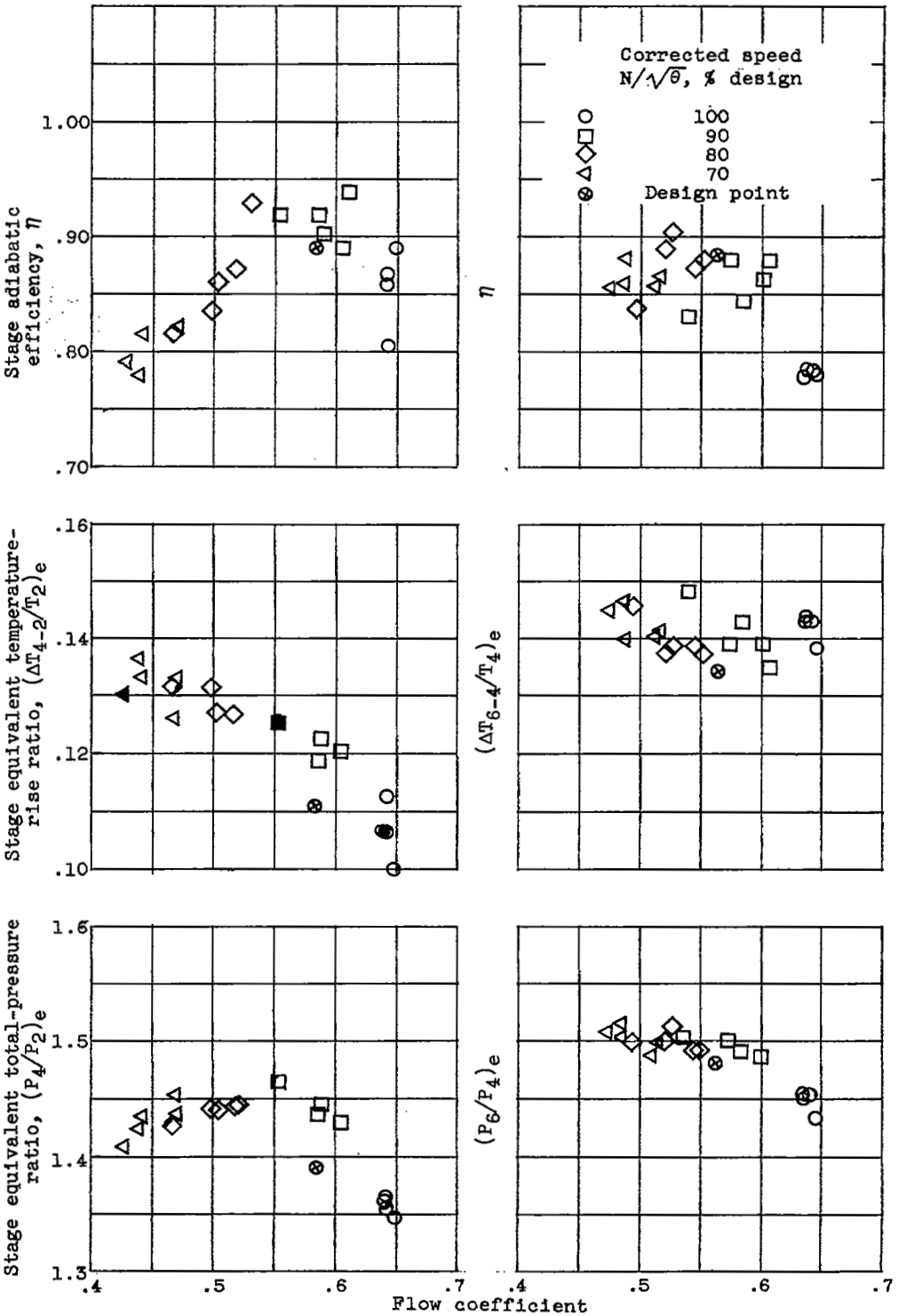

(a) First stage. (b) Second stage.

Figure 7. - Individual stage performance of five-stage transonic compressor (ref. 3).

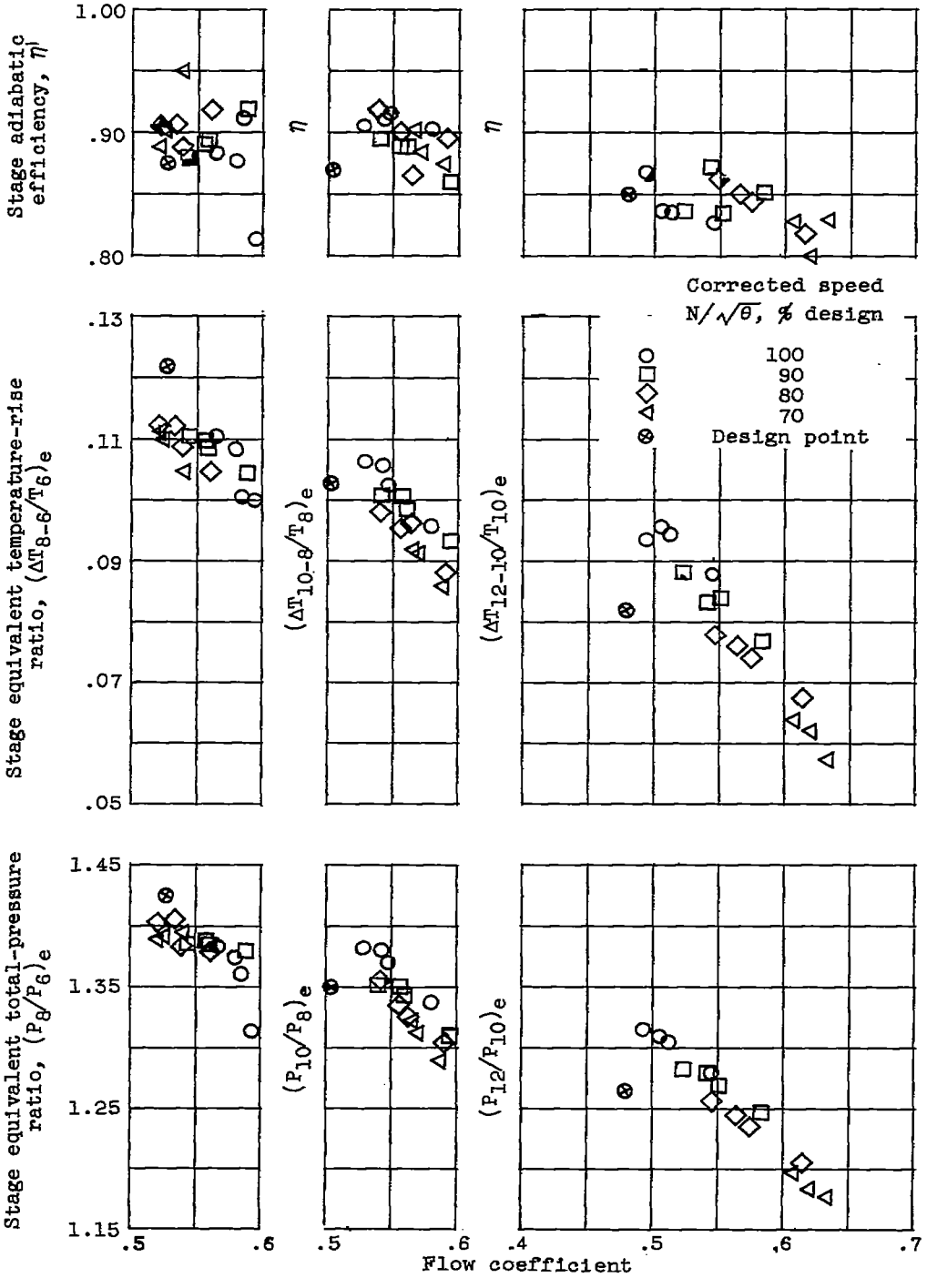

(c) Third stage. (d) Fourth stage. (e) Fifth stage.

Figure 7. - Concluded. Individual stage performance of five-stage transonic compressor (ref. 3).

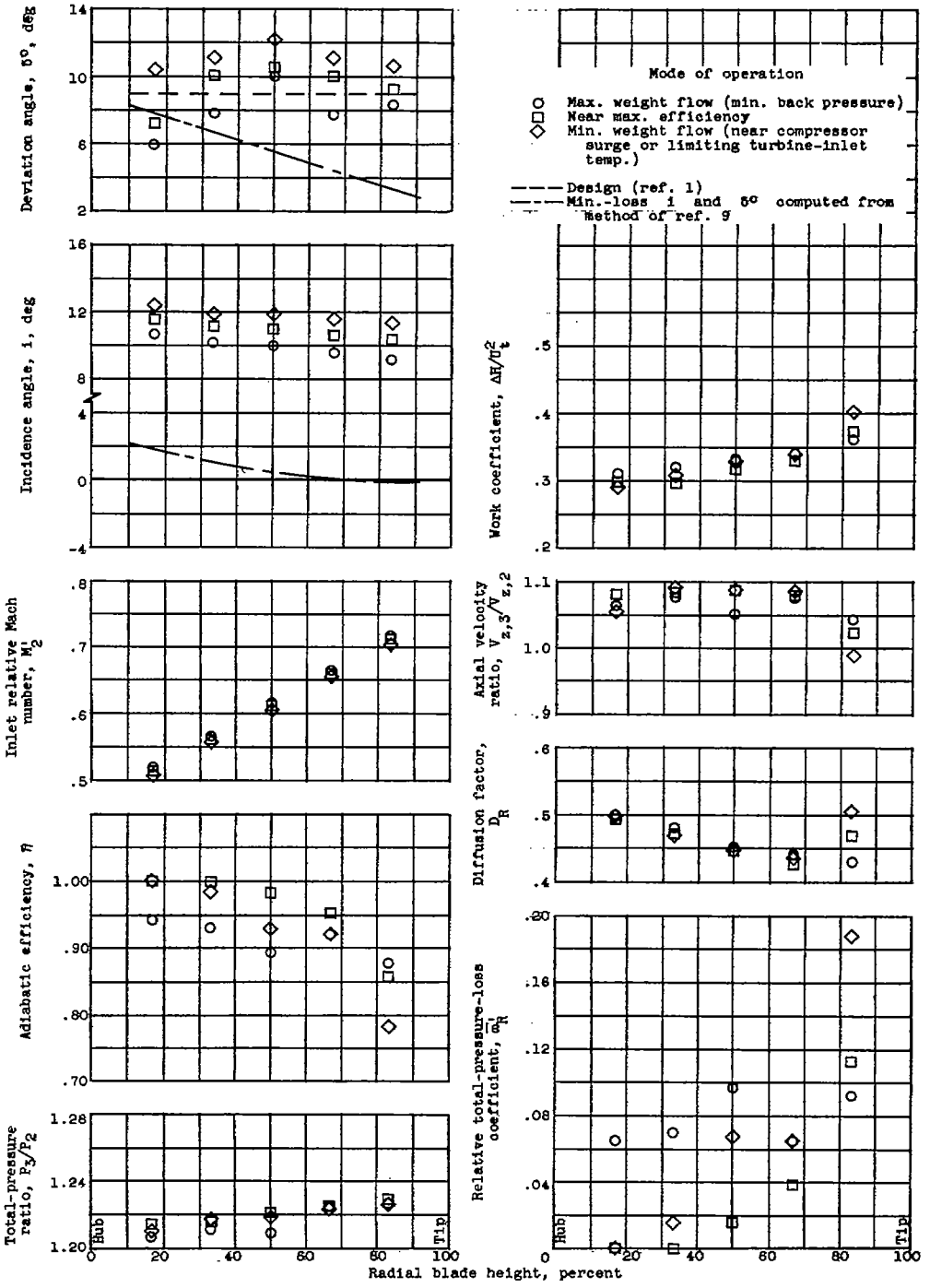

(1) First-stage rotor.

(a) Equivalent speed, 70-percent design.

Figure 8. - Radial variation of rotor blade-element characteristics.

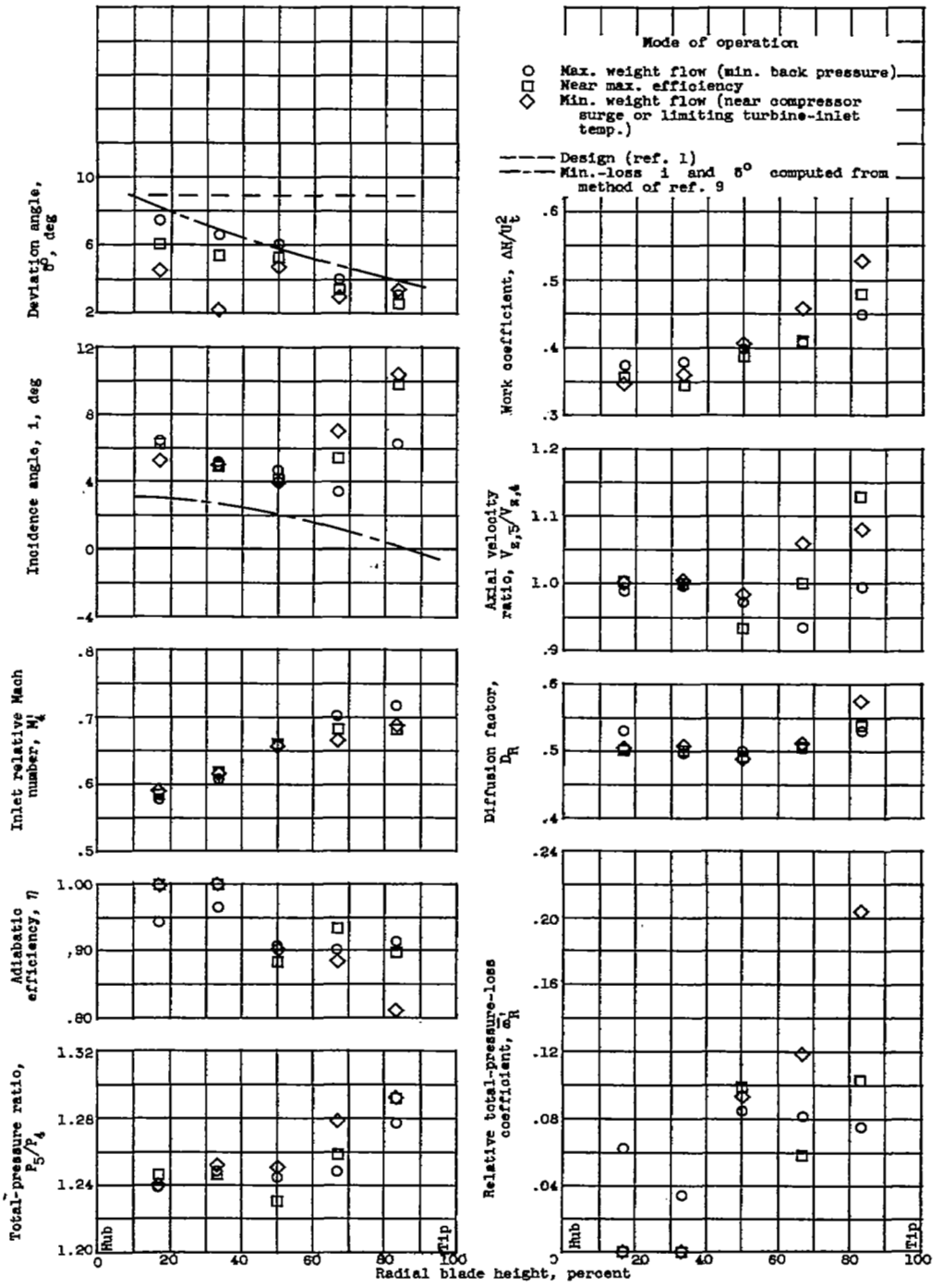

(2) Second-stage rotor.

(a) Continued. Equivalent speed, 70-percent design.

Figure 8. - Continued. Radial variation of rotor blade-element characteristics.

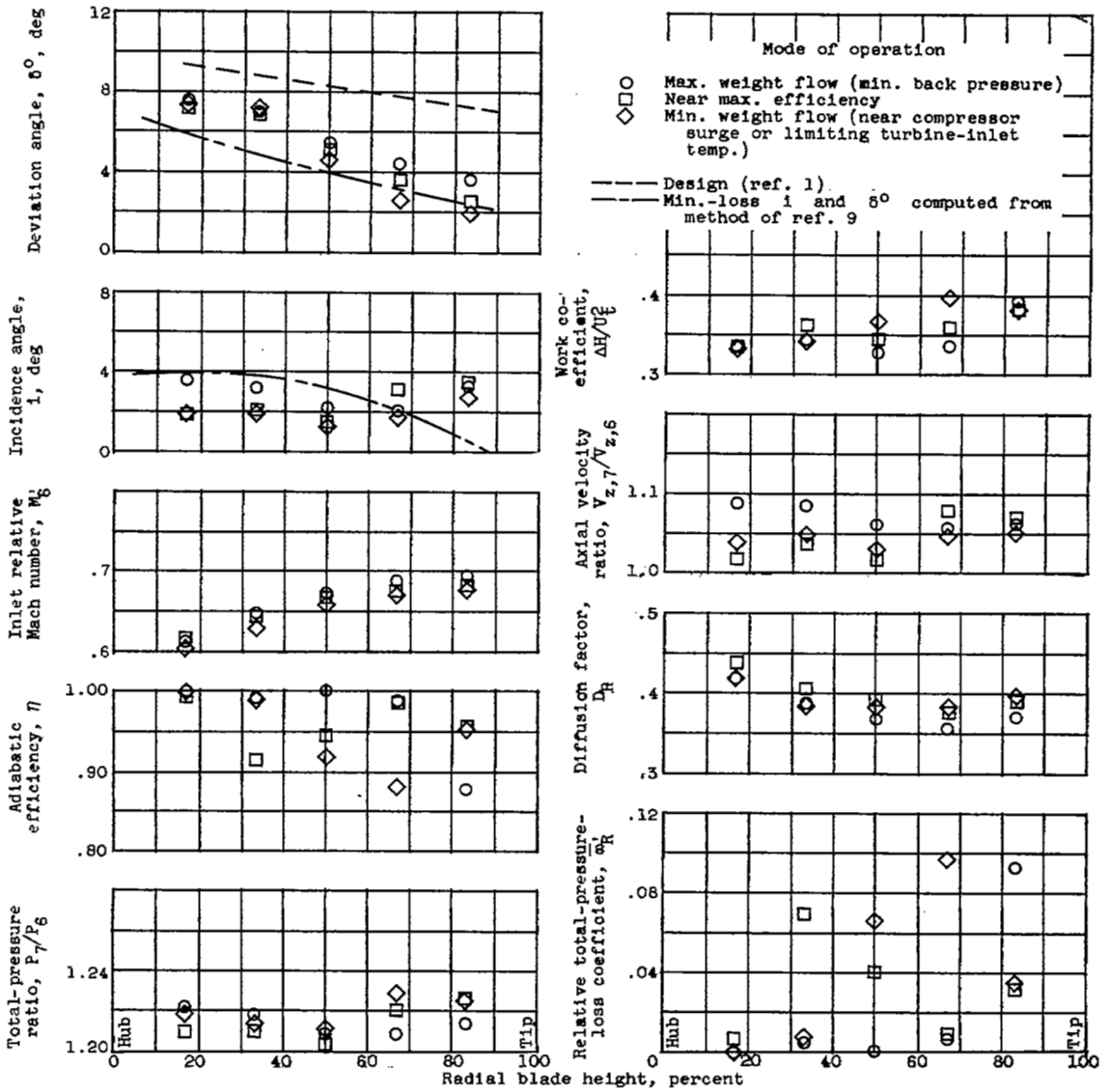

(3) Third-stage rotor.

(a) Continued. Equivalent speed, 70-percent design.

Figure 8. - Continued. Radial variation of rotor blade-element characteristics.

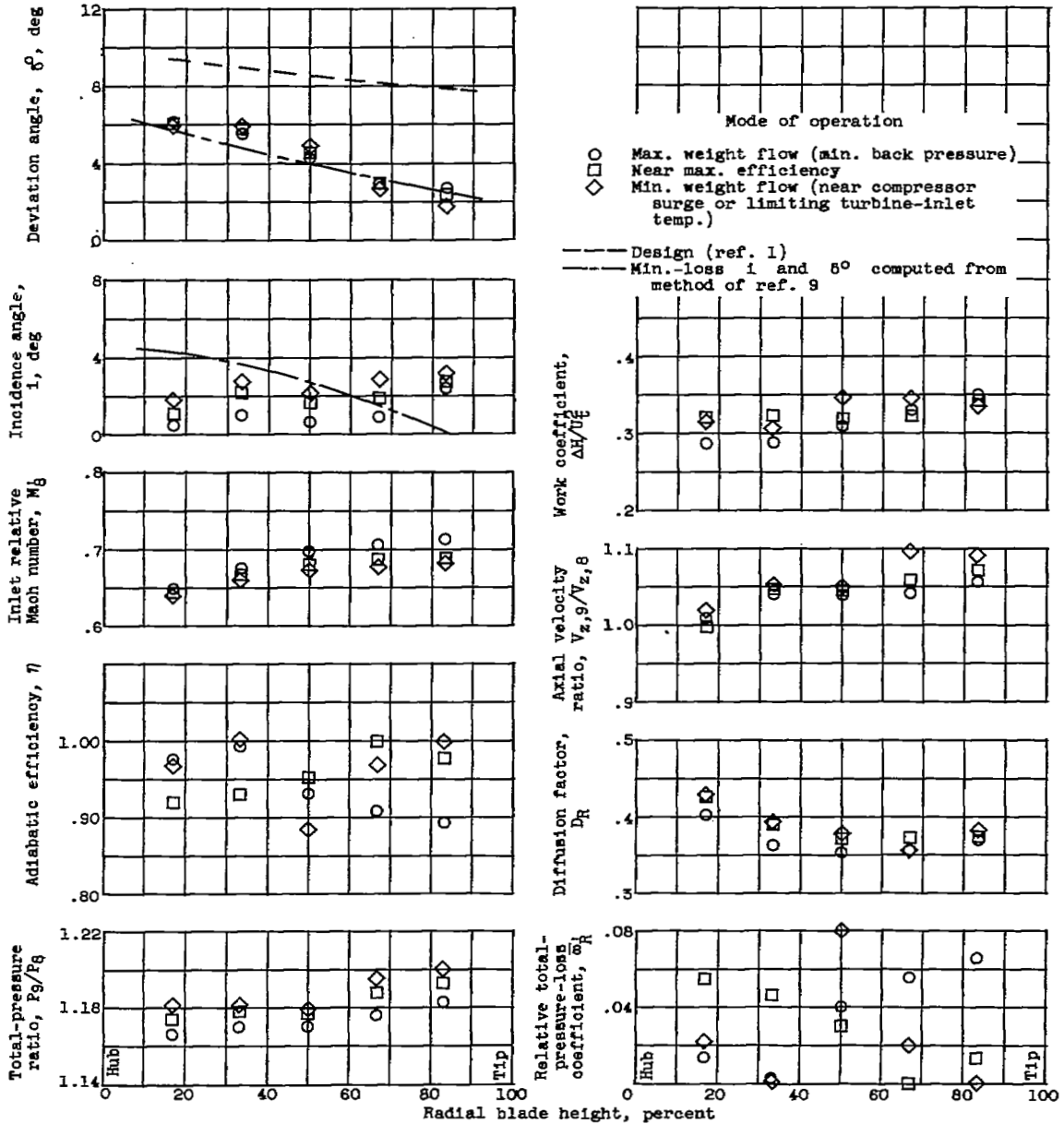

(4) Fourth-stage rotor.

(a) Continued. Equivalent speed, 70-percent design.

Figure 8. - Continued. Radial variation of rotor blade-element characteristics.

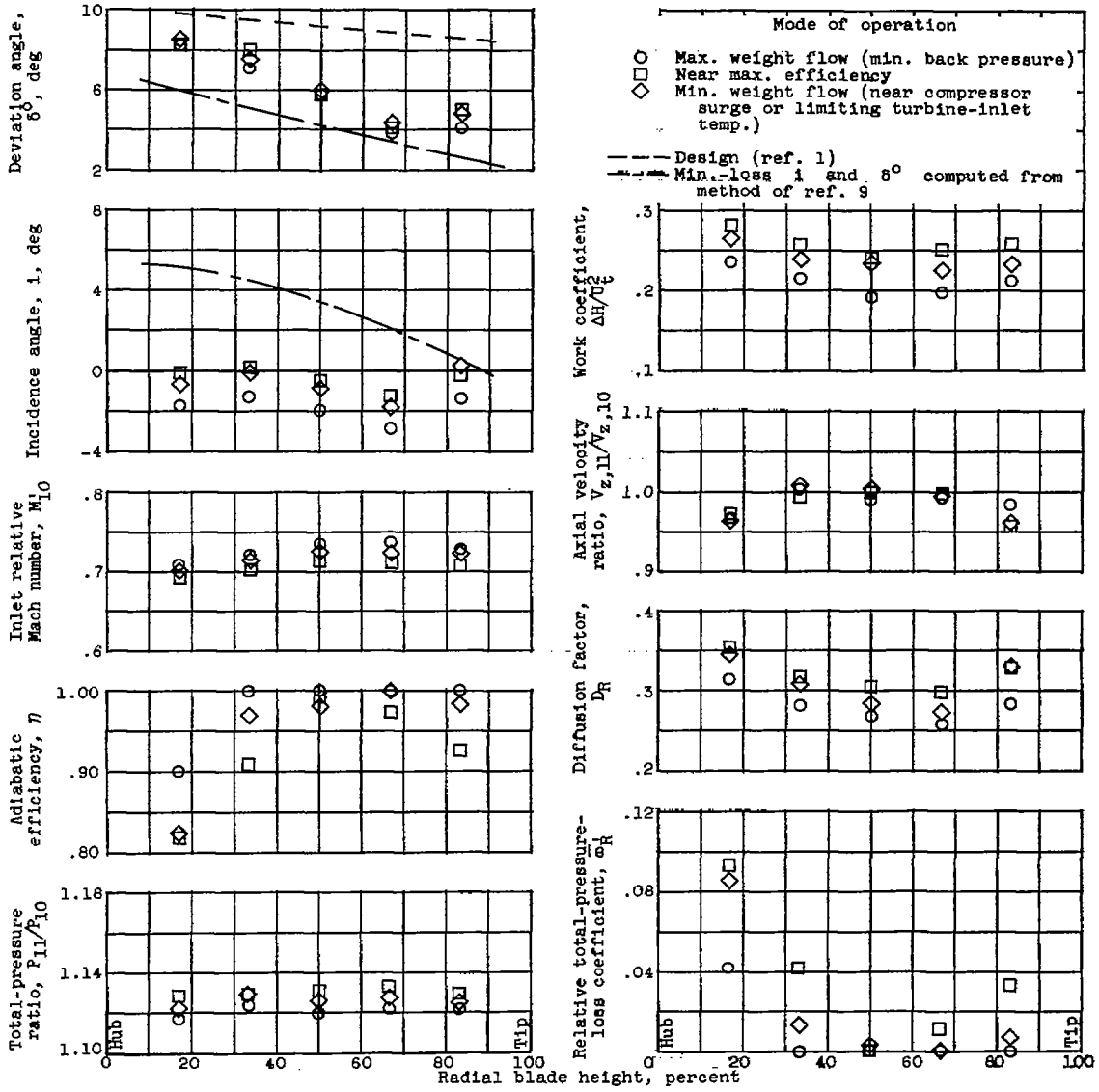

(5) Fifth-stage rotor.

(a) Concluded. Equivalent speed, 70-percent design.

Figure 8. - Continued. Radial variation of rotor blade-element characteristics.

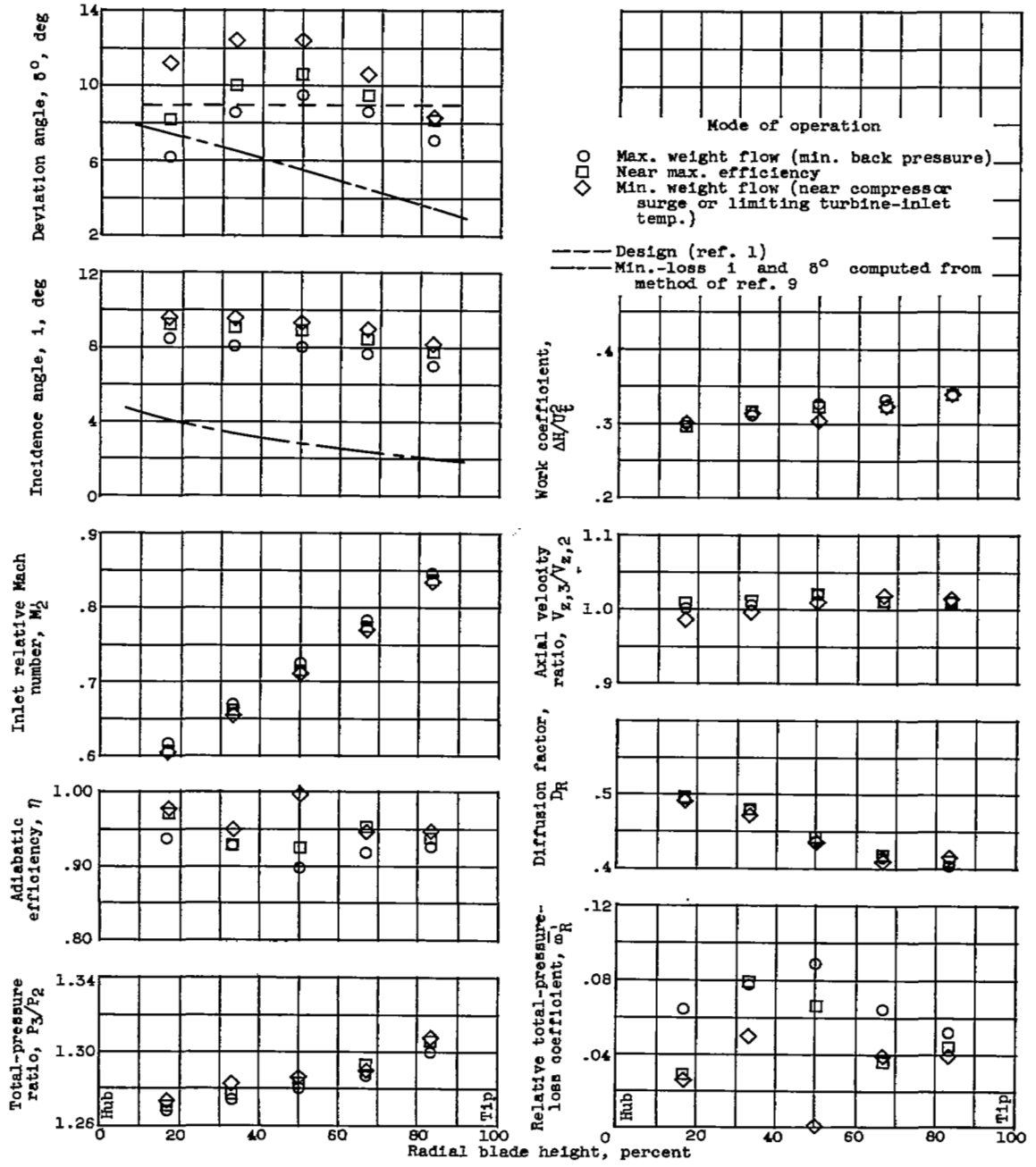

(1) First-stage rotor.

(b) Equivalent speed, 80-percent design.

Figure 8. - Continued. Radial variation of rotor blade-element characteristics.

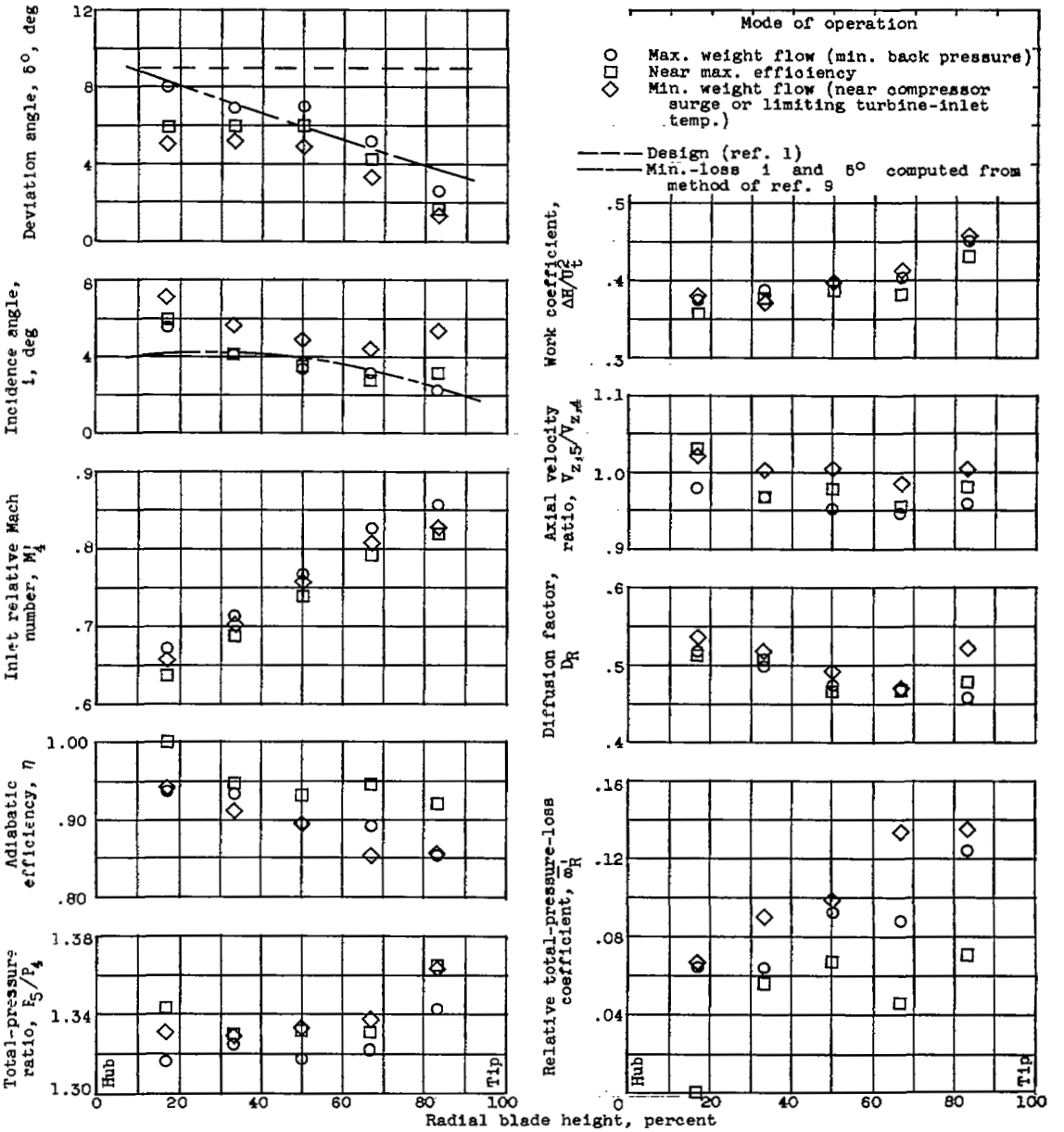

(2) Second-stage rotor.

(b) Continued. Equivalent speed, 80-percent design.

Figure 8. - Continued. Radial variation of rotor blade-element characteristics.

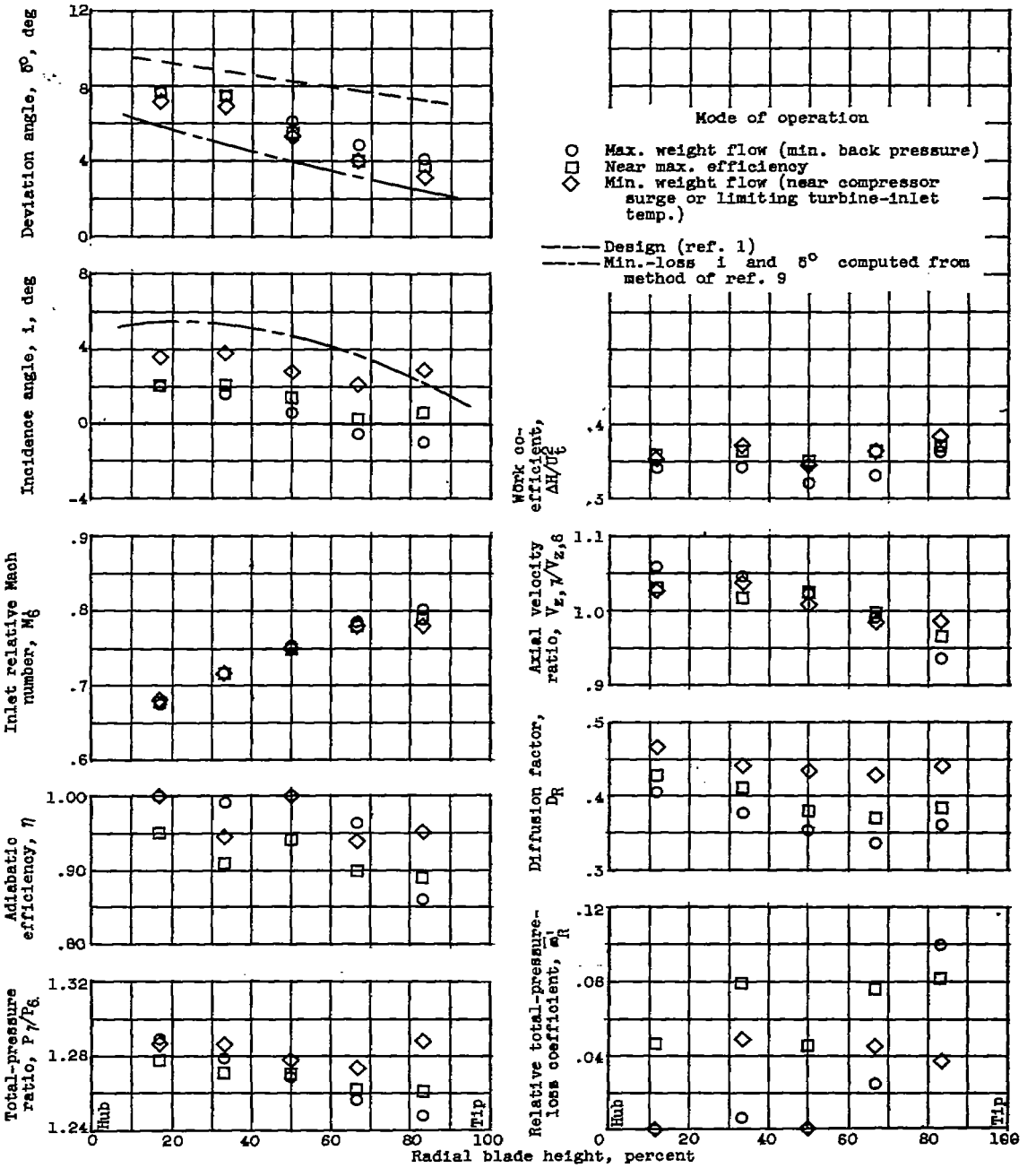

(3) Third-stage rotor.

(b) Continued. Equivalent speed, 80-percent design.

Figure 8. - Continued. Radial variation of rotor blade-element characteristics.

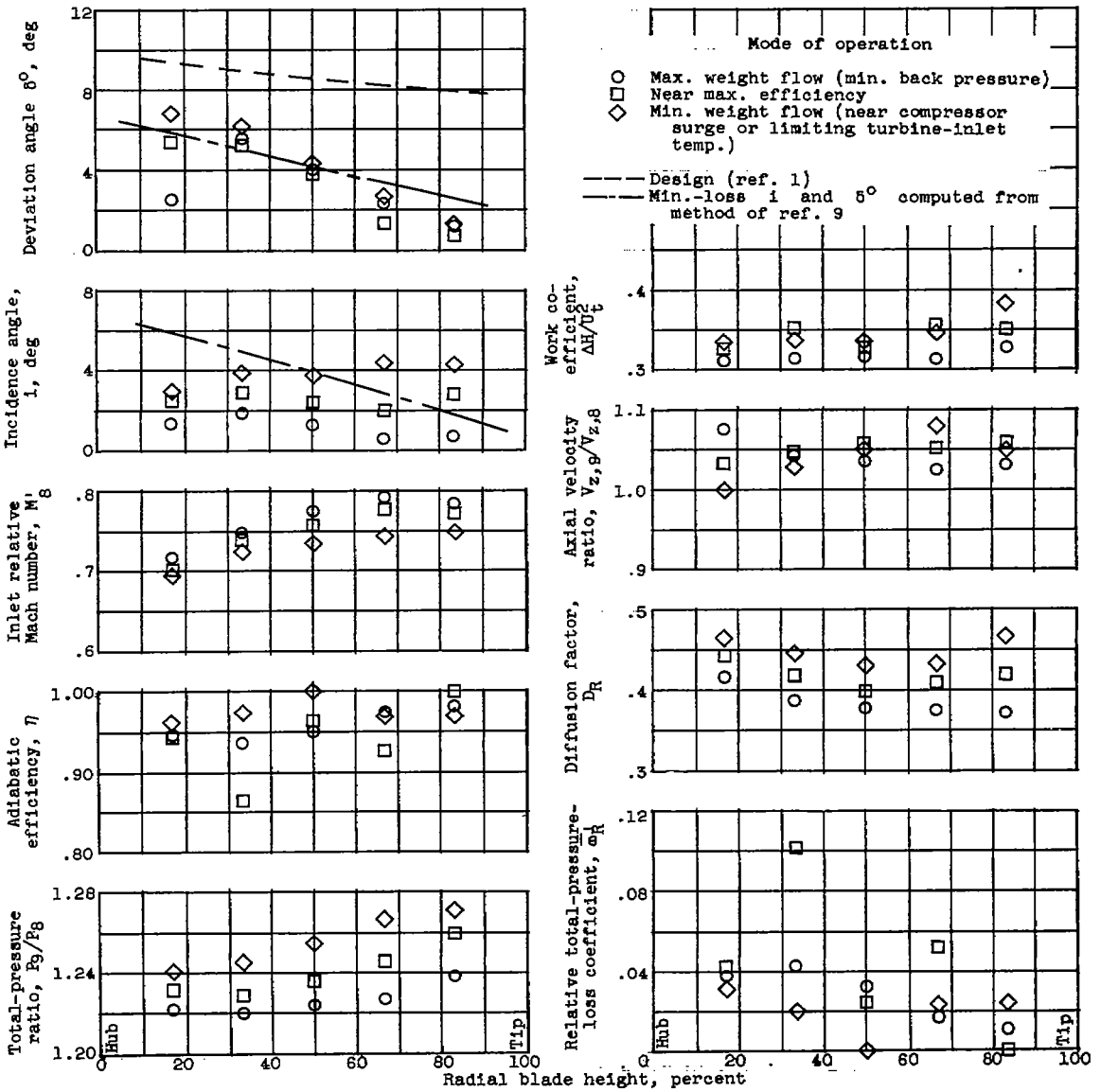

(4) Fourth-stage rotor.

(b) Continued. Equivalent speed, 80-percent design.

Figure 8. - Continued. Radial variation of rotor blade-element characteristics.

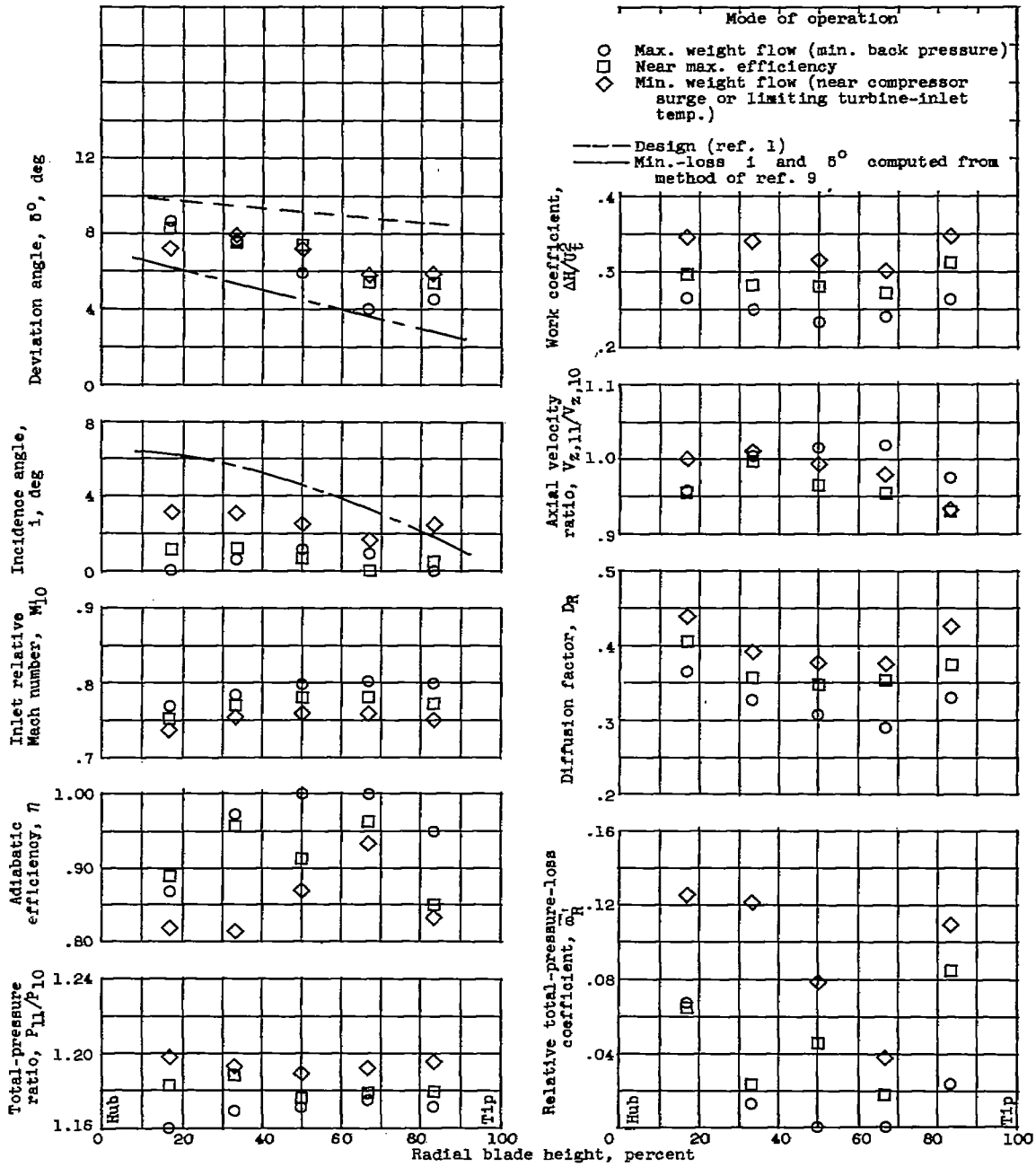

(5) Fifth-stage rotor.

(b) Concluded. Equivalent speed, 80-percent design.

Figure 8. - Continued. Radial variation of rotor blade-element characteristics.

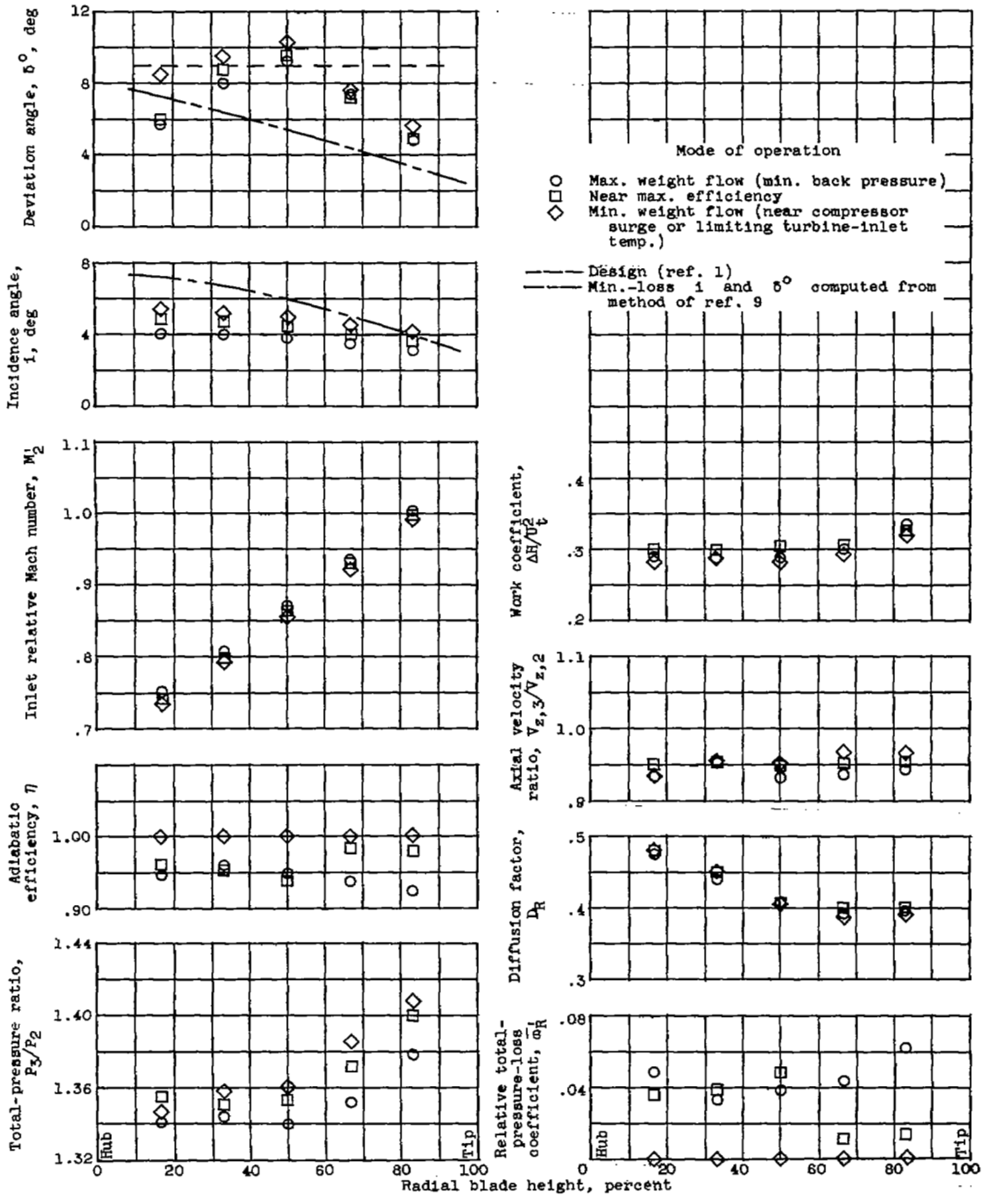

(1) First-stage rotor.

(c) Equivalent speed, 90-percent design.

Figure 8. - Continued. Radial variation of rotor blade-element characteristics.

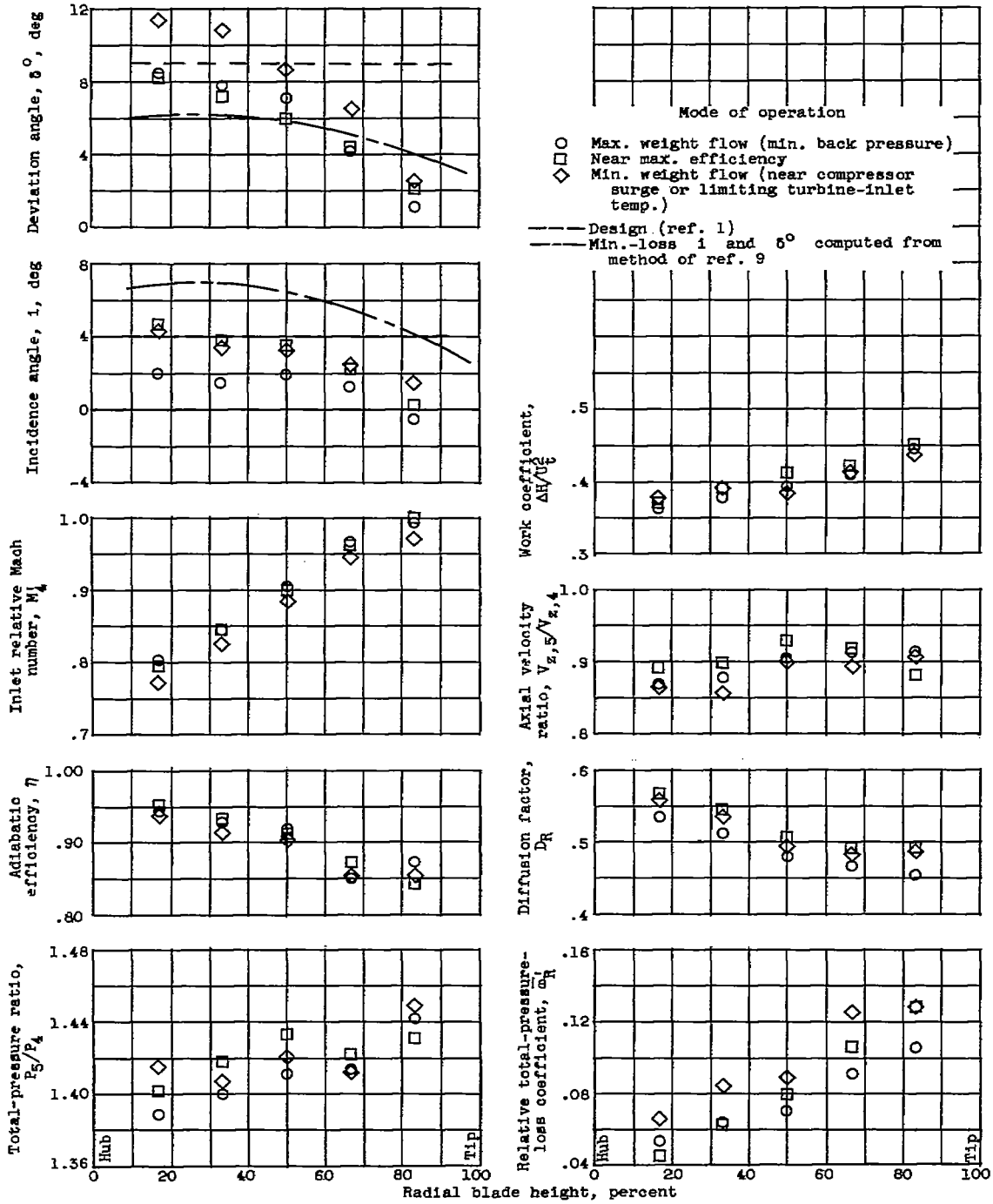

(2) Second-stage rotor.

(c) Continued. Equivalent speed, 90-percent design.

Figure 8. - Continued. Radial variation of rotor blade-element characteristics.

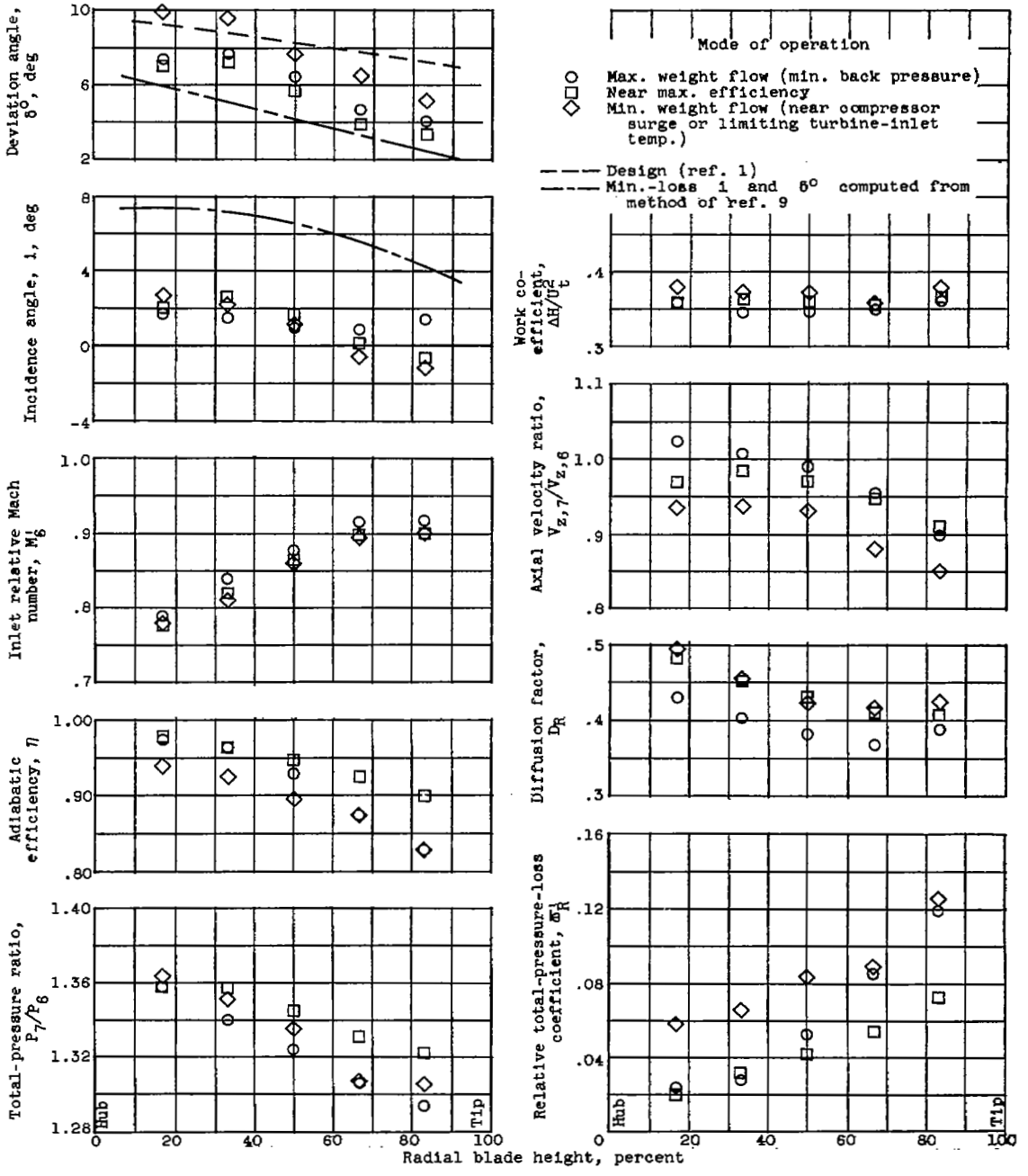

(3) Third-stage rotor.

(c) Continued. Equivalent speed, 90-percent design.

Figure 8. - Continued. Radial variation of rotor blade-element characteristics.

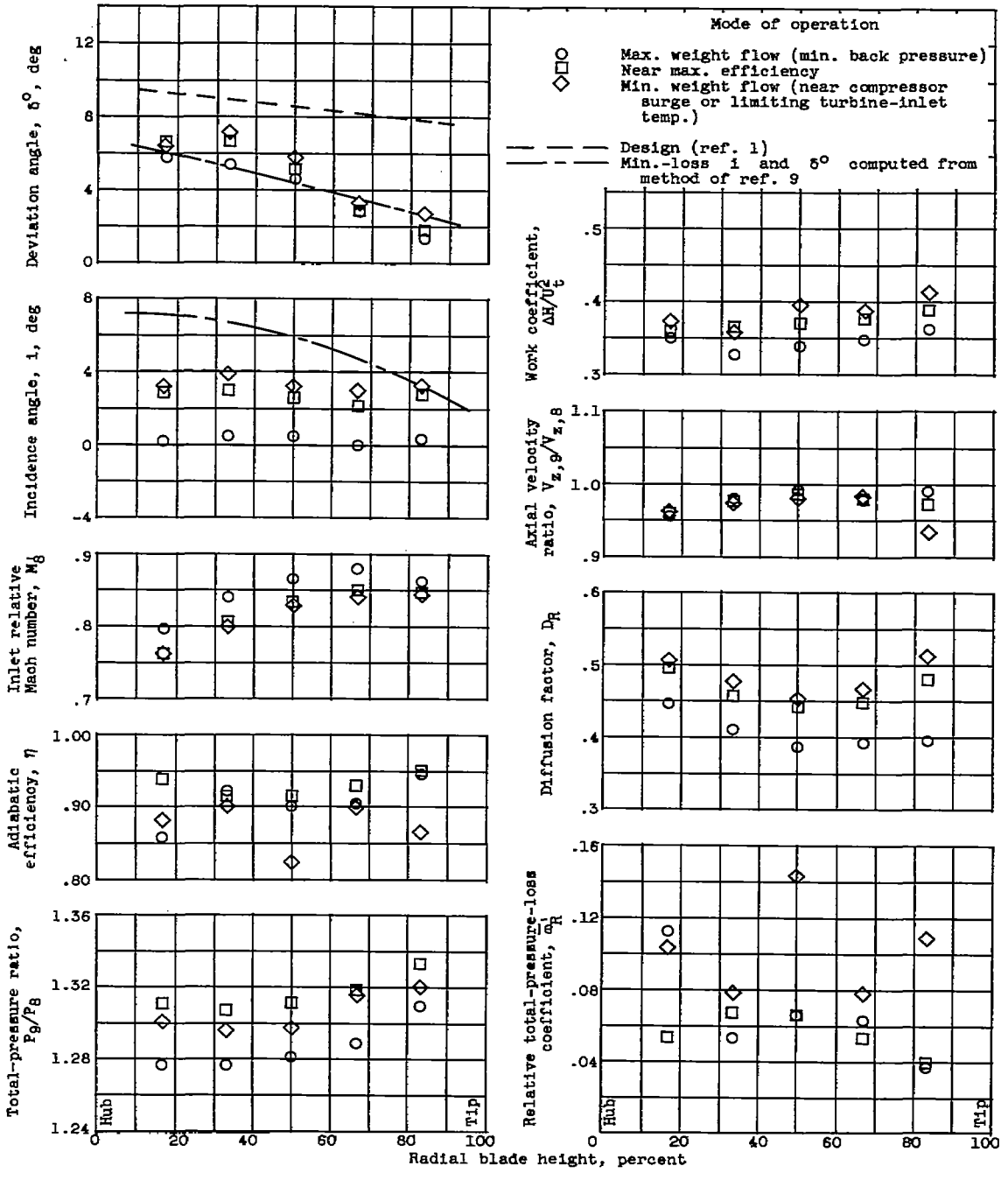

(4) Fourth-stage rotor.

(c) Continued. Equivalent speed, 90-percent design.

Figure 8. - Continued. Radial variation of rotor blade-element characteristics.

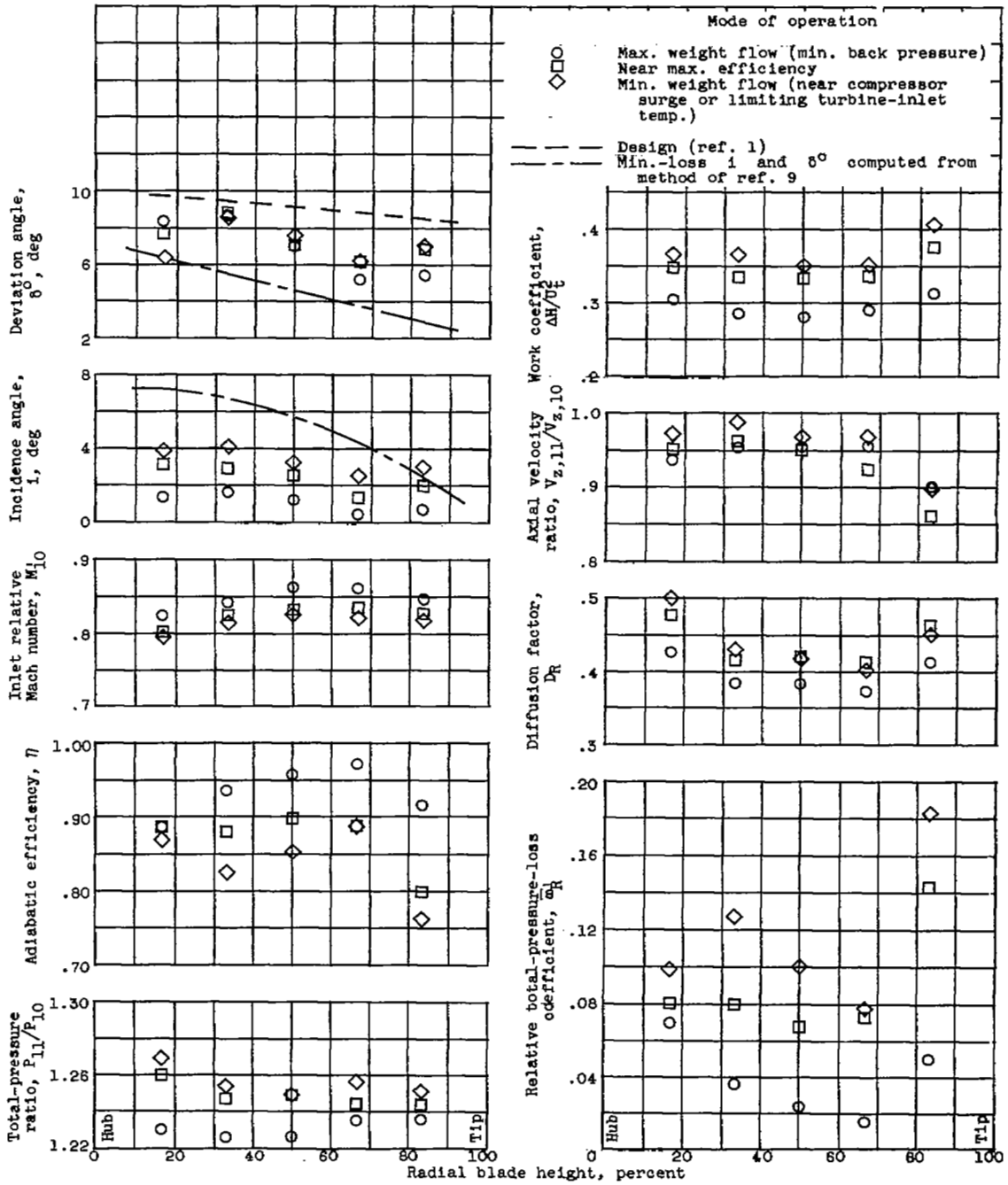

(5) Fifth-stage rotor.

(c) Concluded. Equivalent speed, 90-percent design.

Figure 8. - Continued. Radial variation of rotor blade-element characteristics.

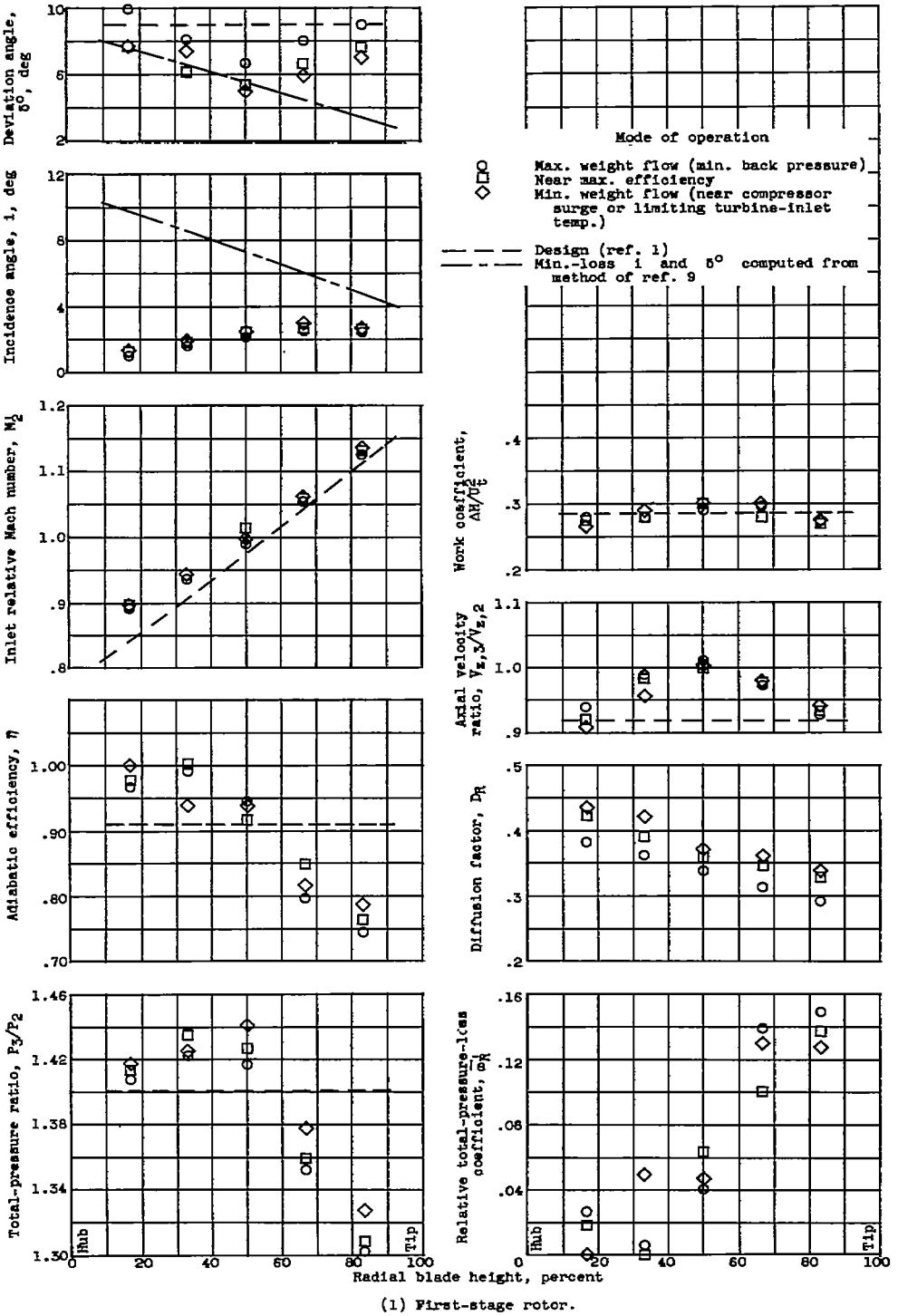

(1) First-stage rotor.

(d) Equivalent speed, 100-percent design.

Figure 8. - Continued. Radial variation of rotor blade-element characteristics.

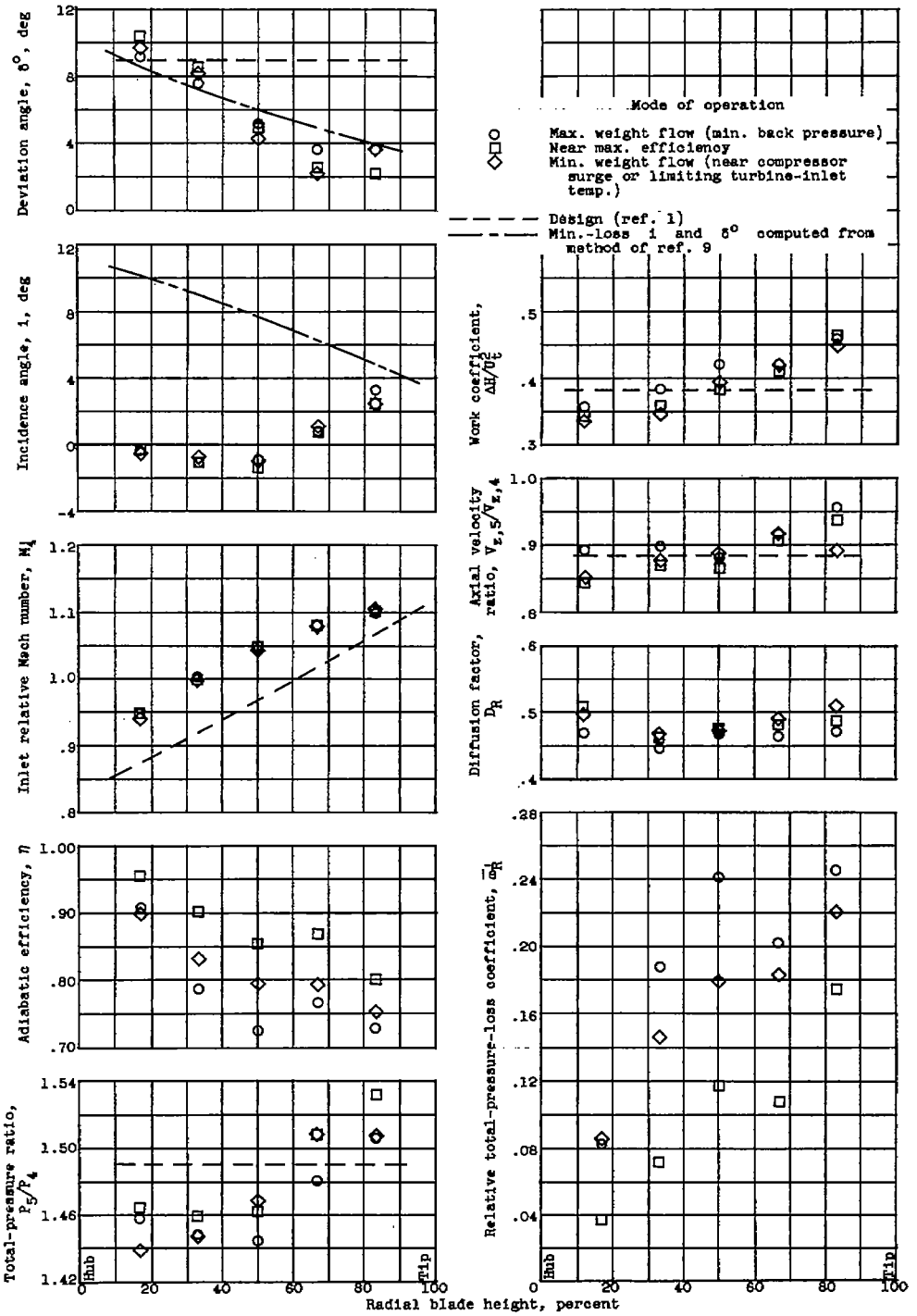

(2) Second-stage rotor.

(d) Continued. Equivalent speed, 100-percent design.

Figure 8. - Continued. Radial variation of rotor blade-element characteristics.

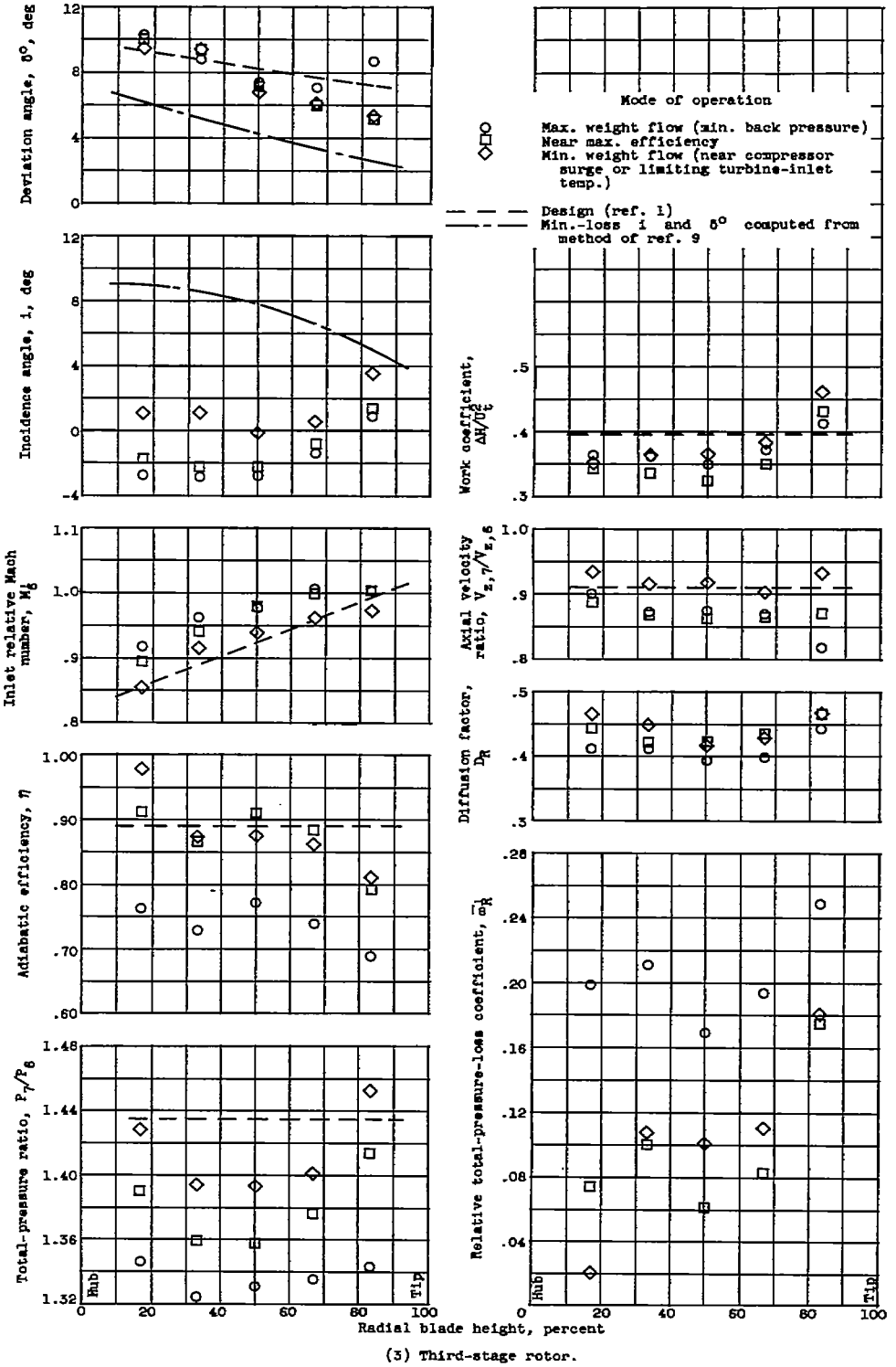

(3) Third-stage rotor.

(d) Continued. Equivalent speed, 100-percent design.

Figure 8. - Continued. Radial variation of rotor blade-element characteristics.

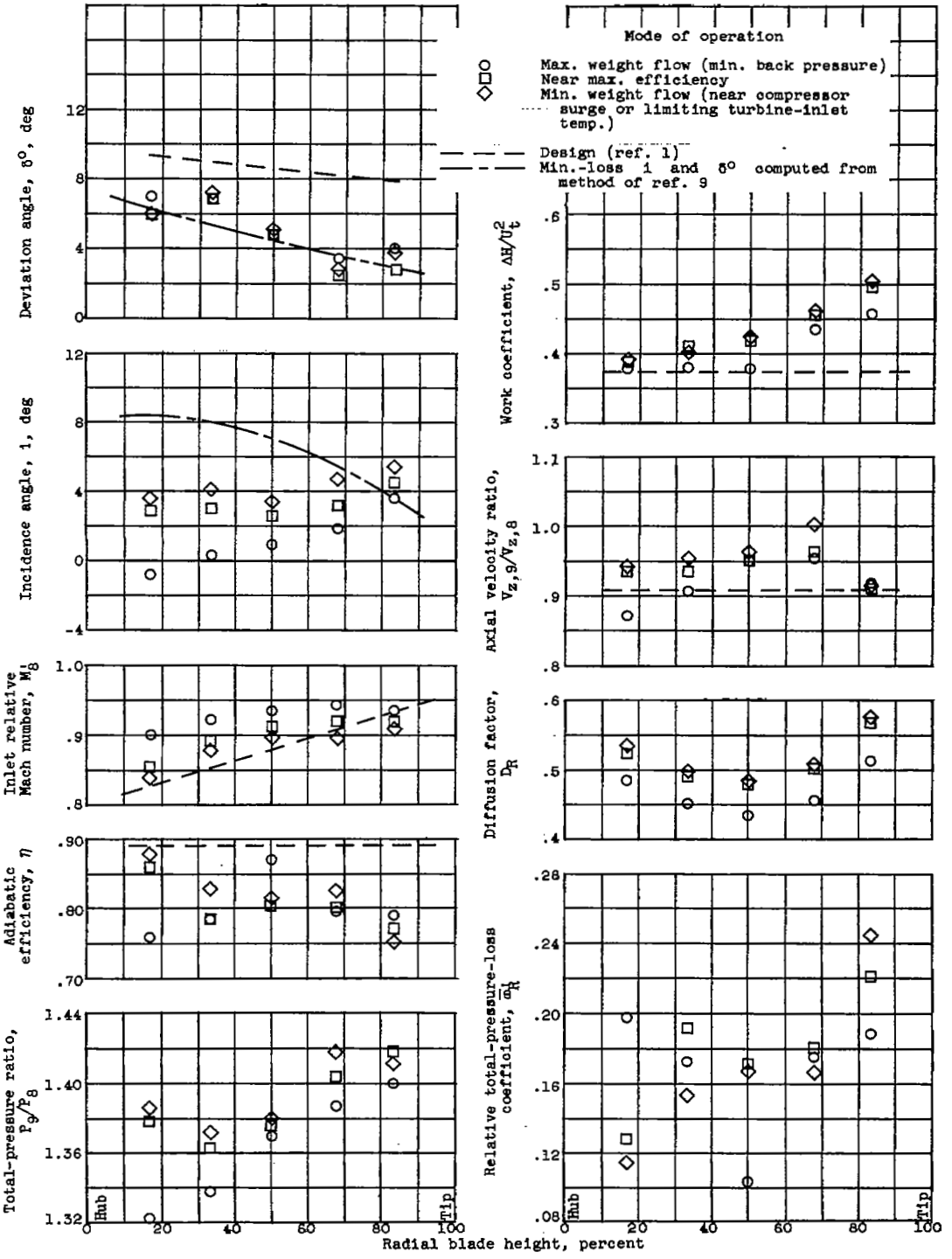

(4) Fourth-stage rotor.

(d) Continued. Equivalent speed, 100-percent design.

Figure 8. - Continued. Radial variation of rotor blade-element characteristics.

[redacted]

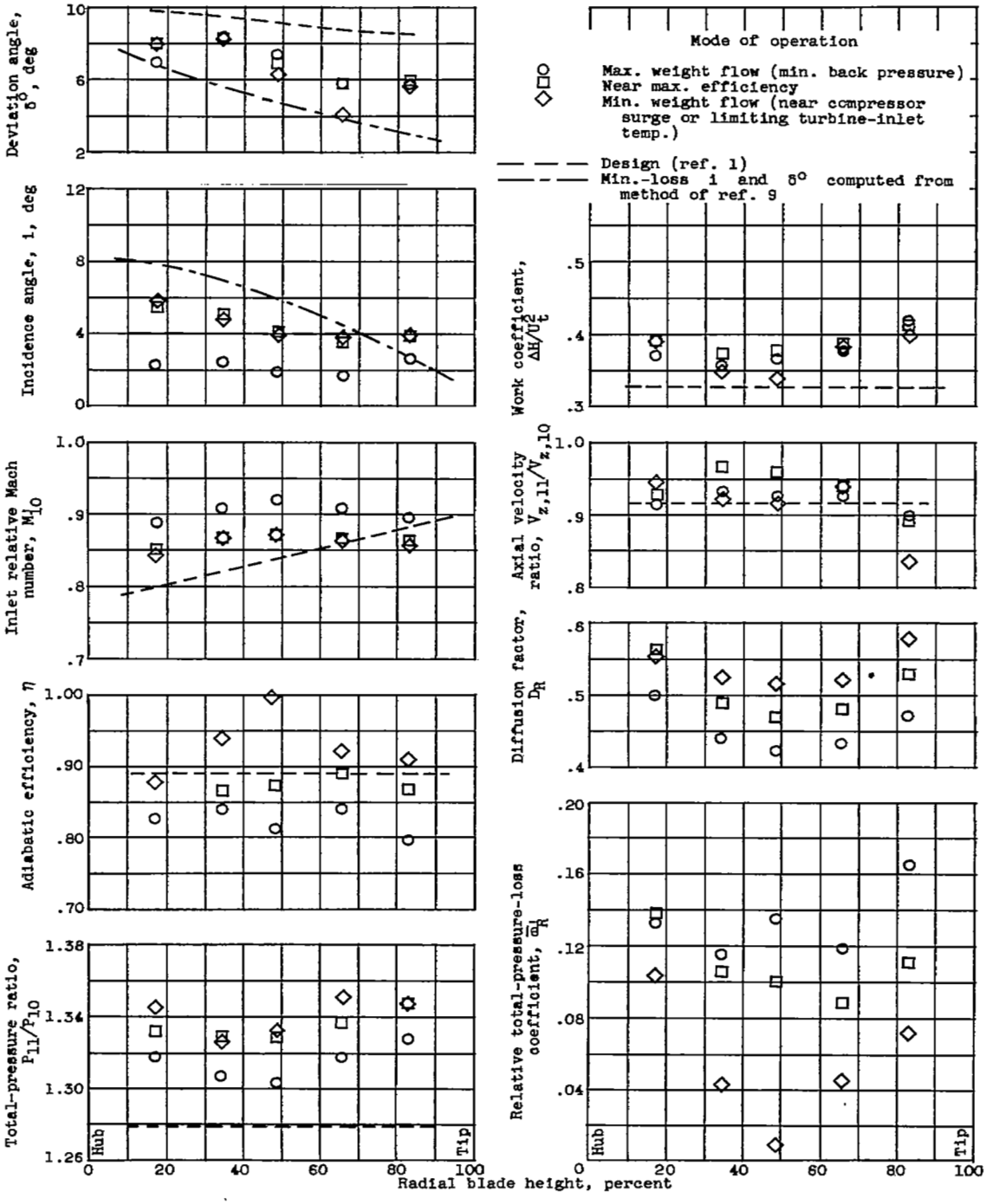

(5) Fifth-stage rotor.

(d) Concluded. Equivalent speed, 100-percent design.

Figure 8. - Concluded. Radial variation of rotor blade-element characteristics.

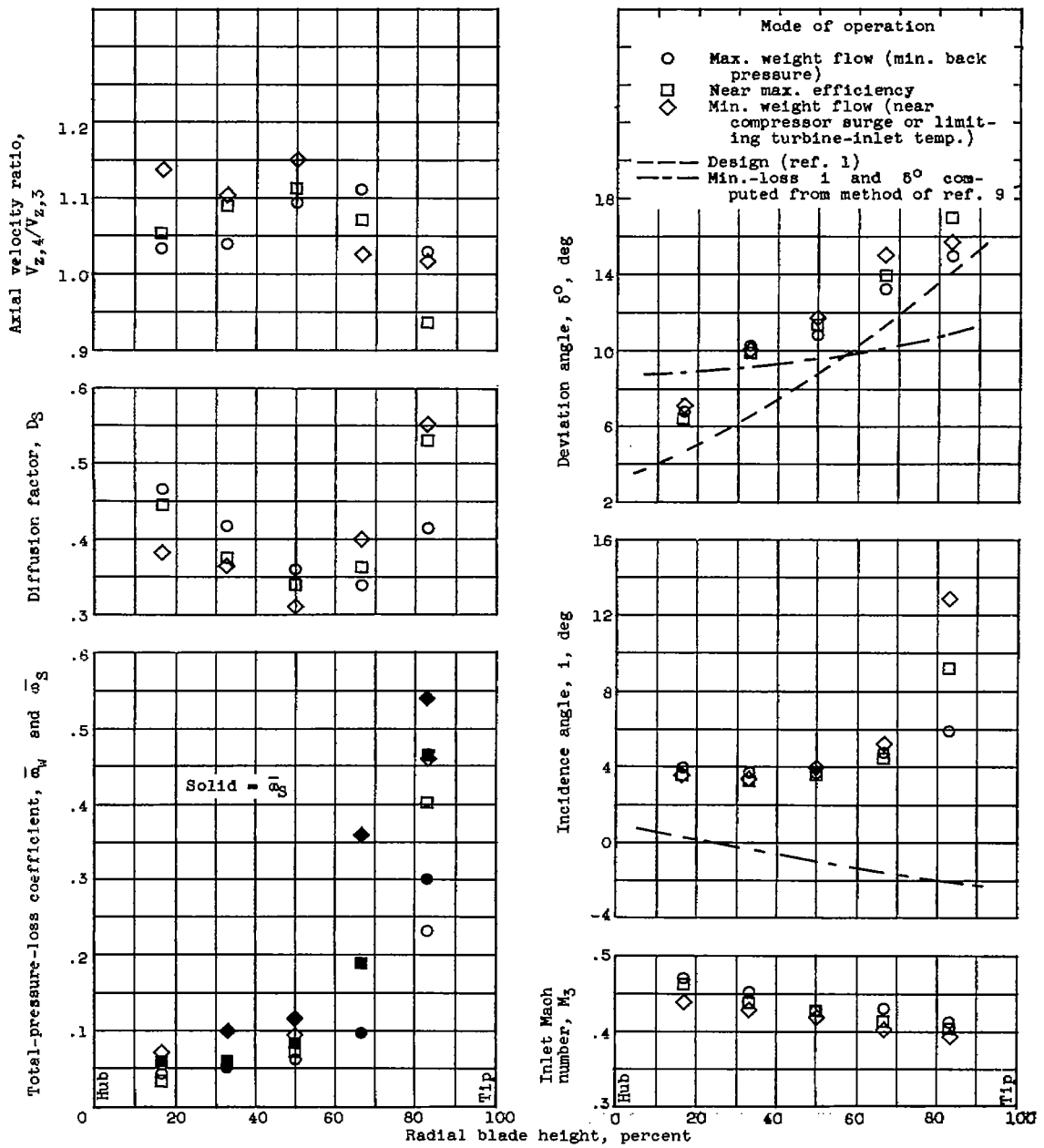

(1) First-stage stator.

(a) Equivalent speed, 70-percent design.

Figure 9. - Radial variation of stator blade-element characteristics.

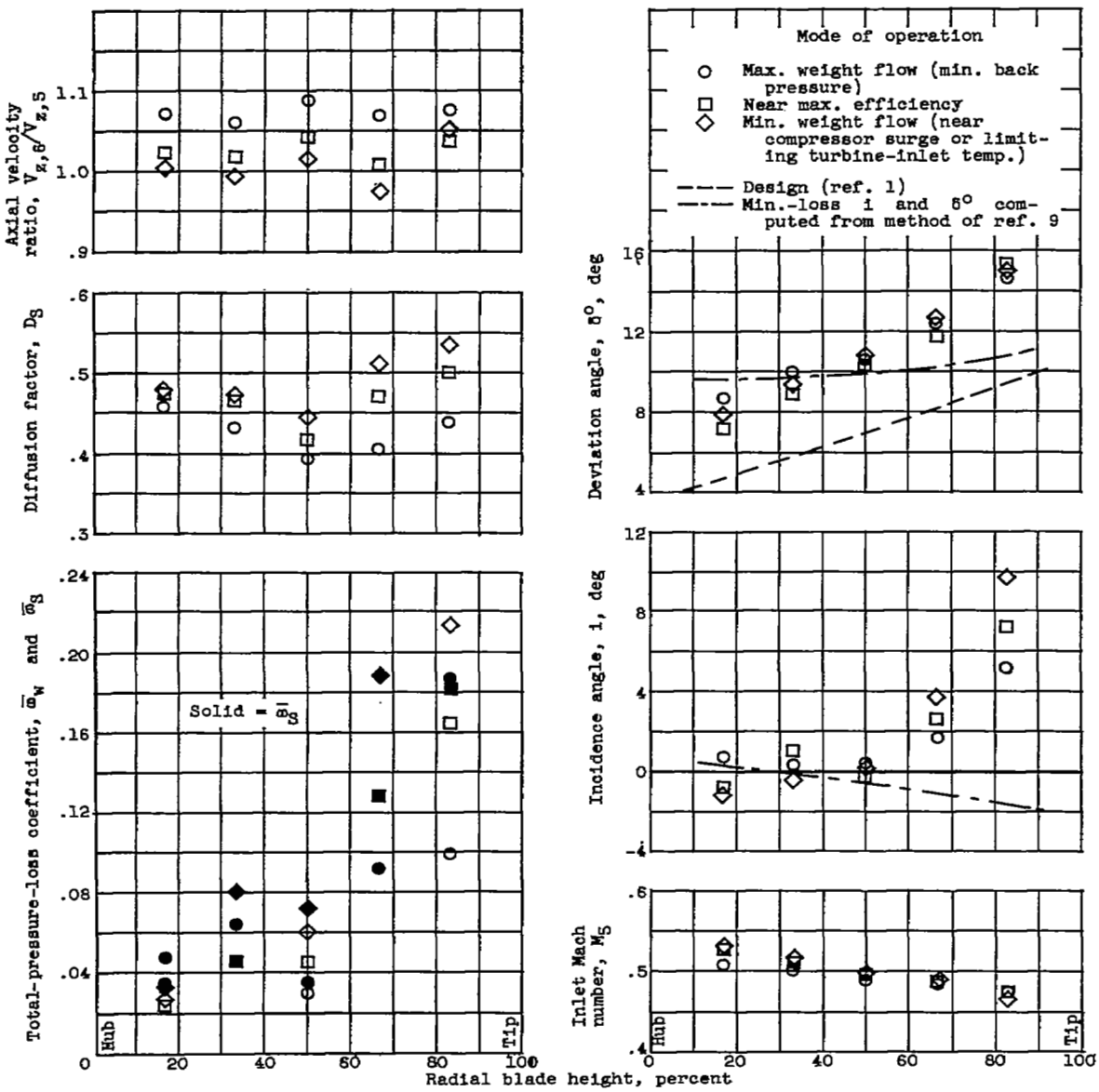

(2) Second-stage stator.

(a) Continued. Equivalent speed, 70-percent design.

Figure 9. - Continued. Radial variation of stator blade-element characteristics.

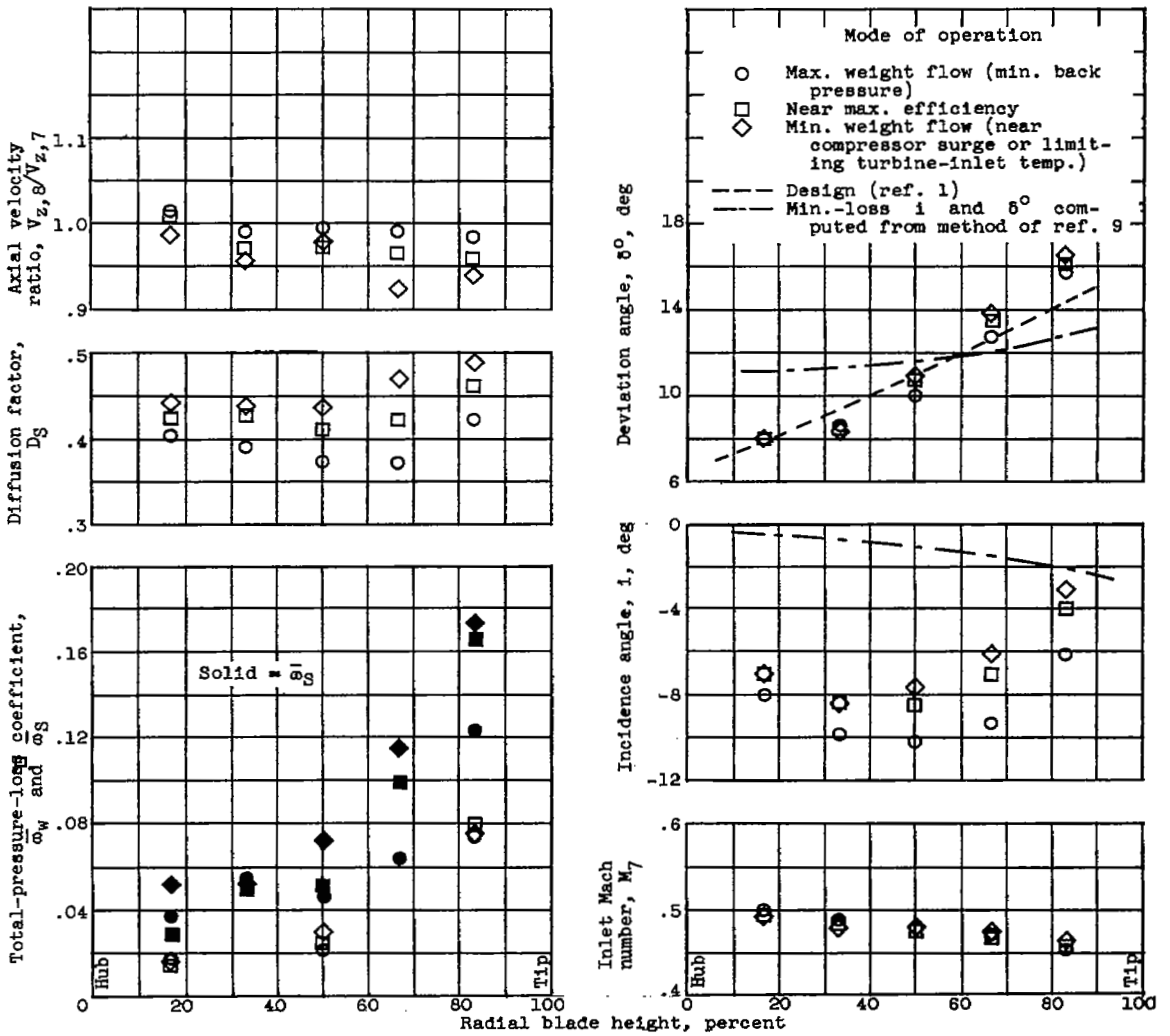

(3) Third-stage stator.

(a) Continued. Equivalent speed, 70-percent design.

Figure 9. - Continued. Radial variation of stator blade-element characteristics.

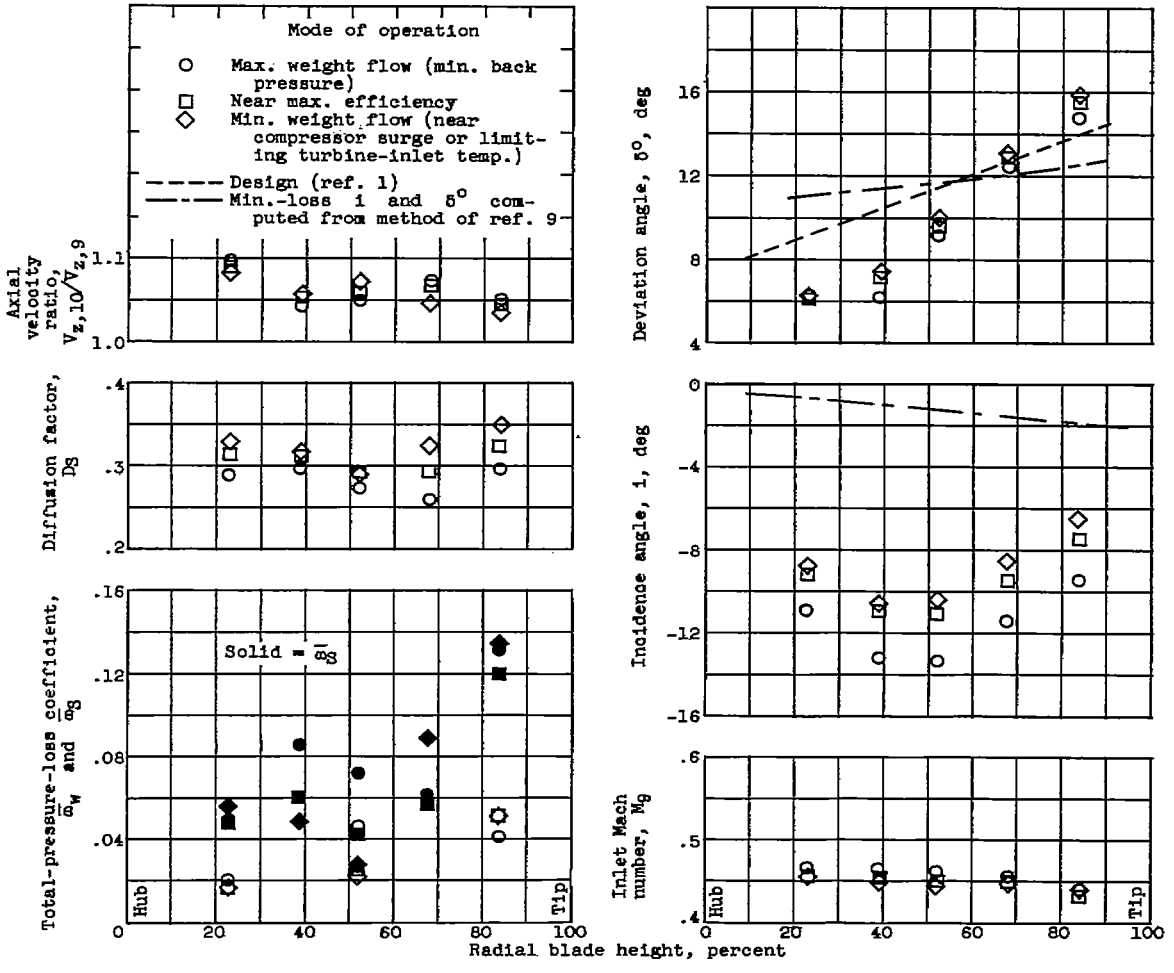

(4) Fourth-stage stator.

(a) Continued. Equivalent speed, 70-percent design.

Figure 9. - Continued. Radial variation of stator blade-element characteristics.

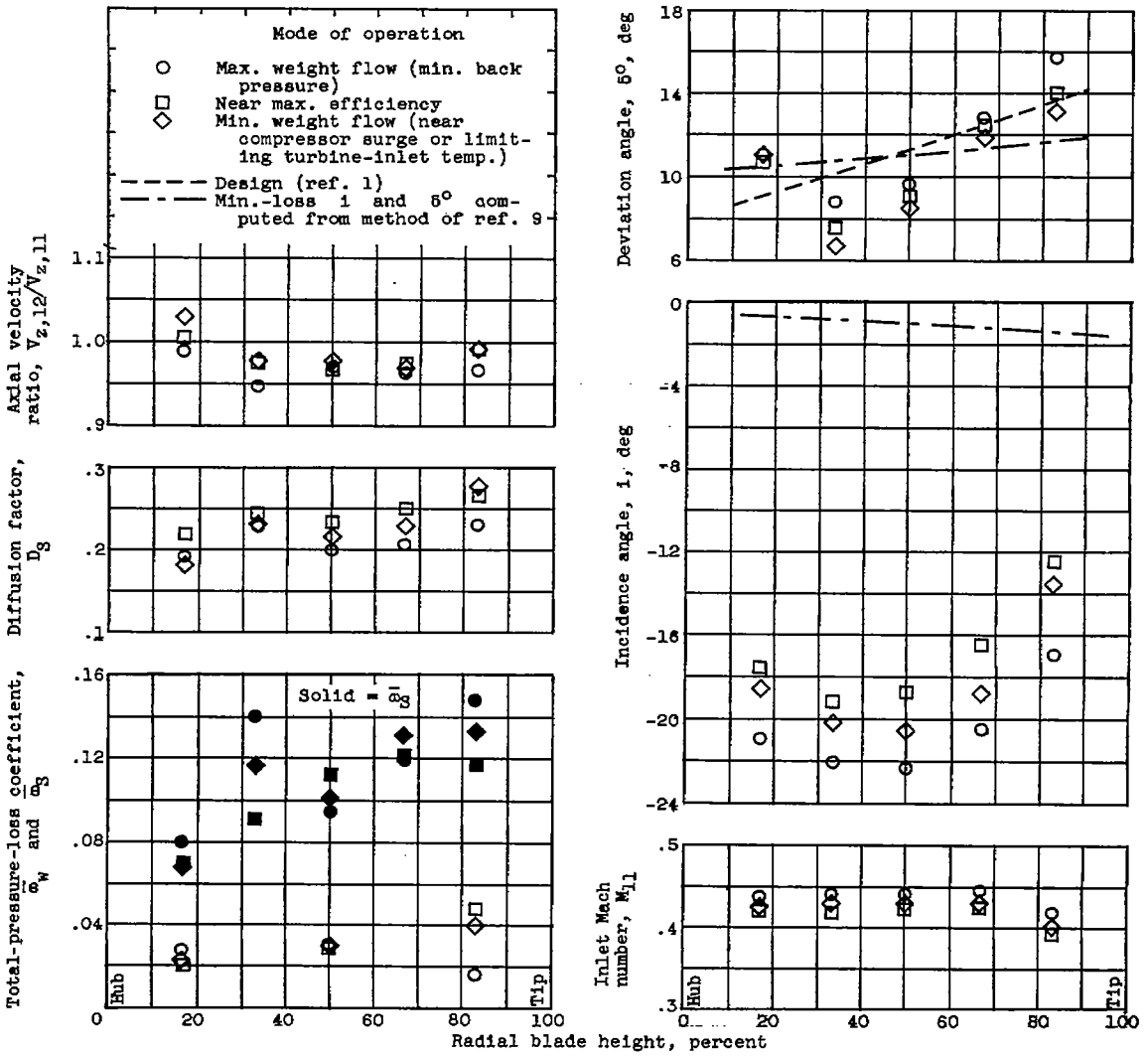

(5) Fifth-stage stator.

(a) Concluded. Equivalent speed, 70-percent design.

Figure 9. - Continued. Radial variation of stator blade-element characteristics.

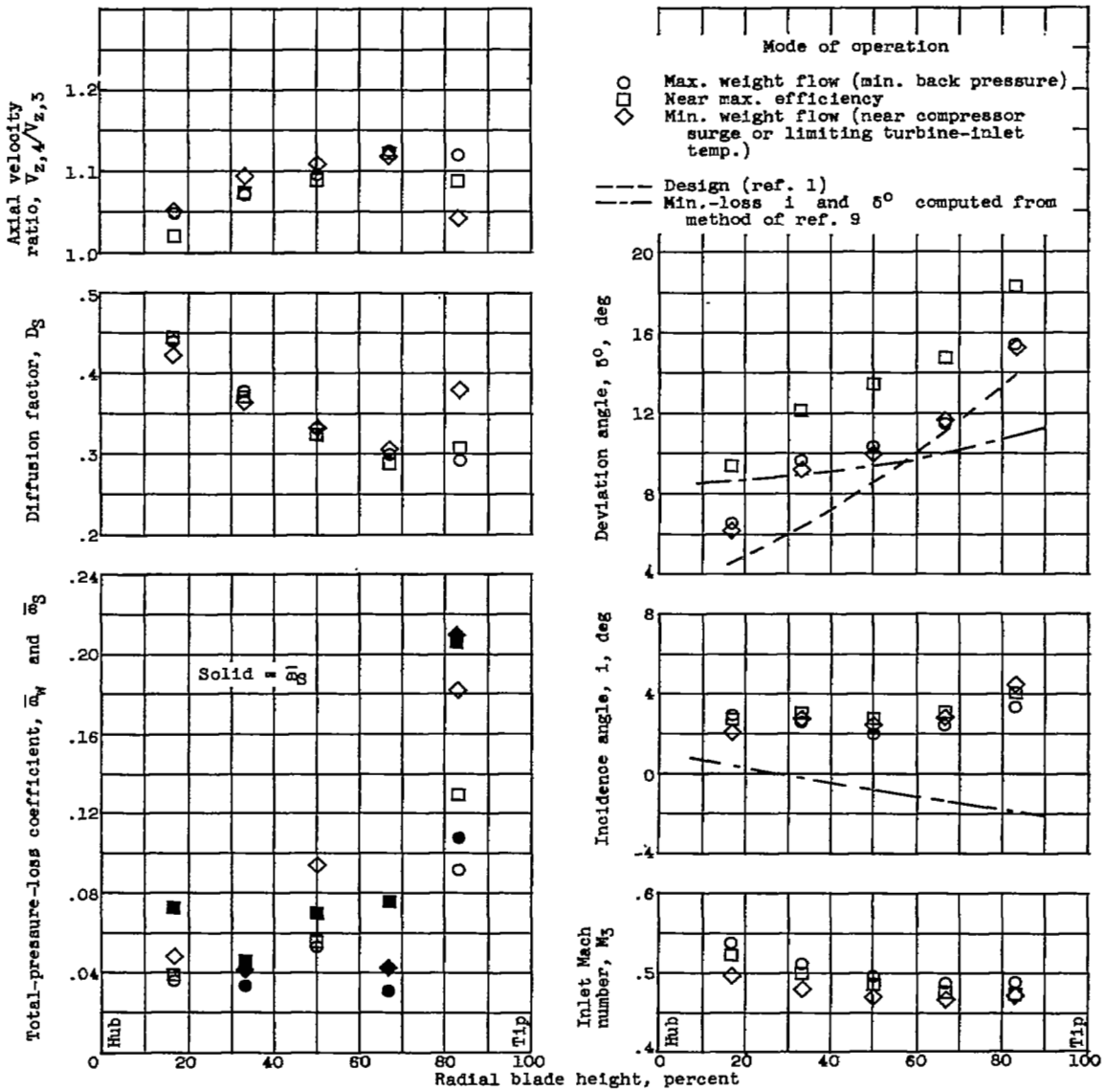

(1) First-stage stator.

(b) Equivalent speed, 80-percent design.

Figure 9. - Continued. Radial variation of stator blade-element characteristics.

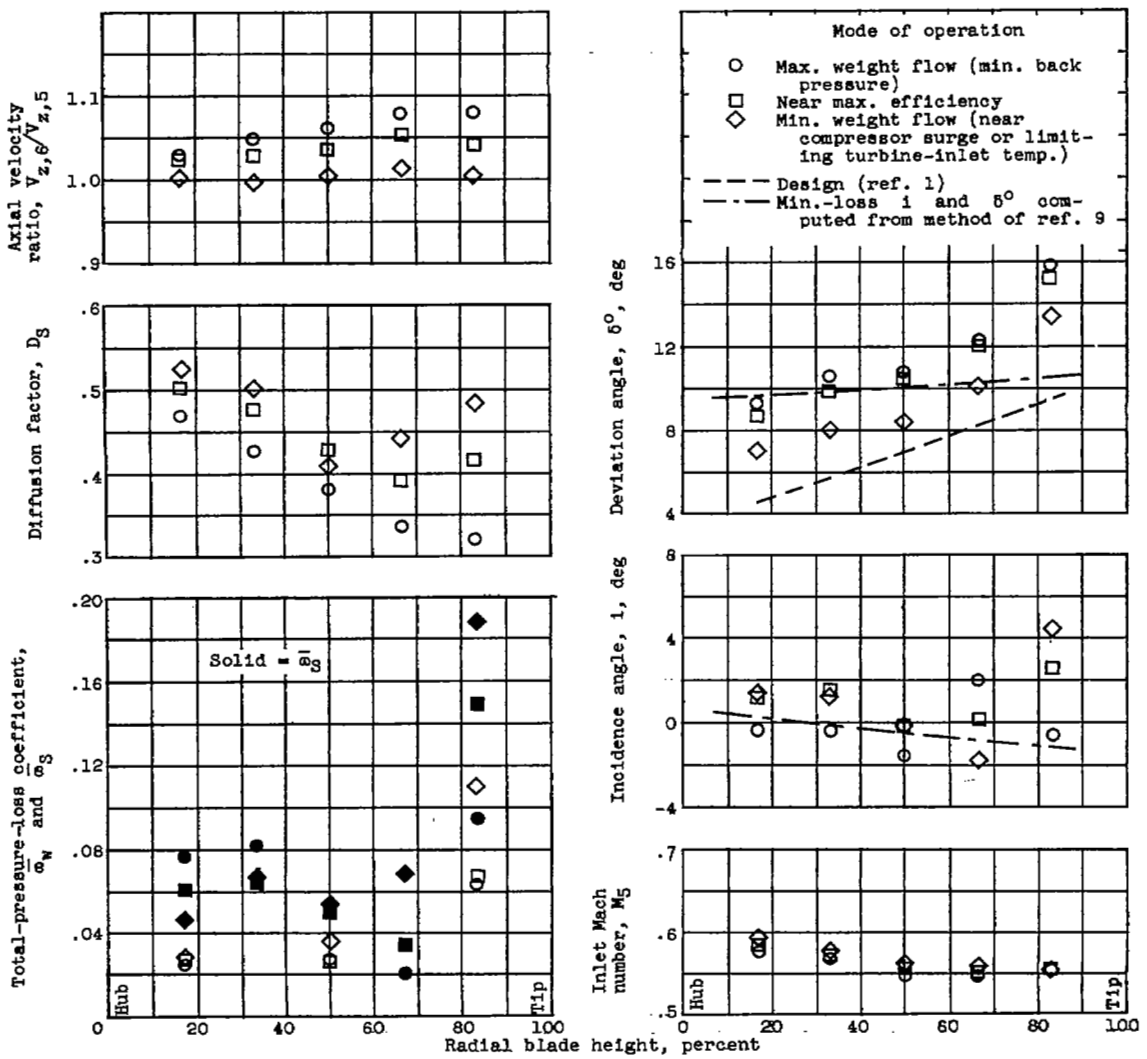

(2) Second-stage stator.

(b) Continued. Equivalent speed, 80-percent design.

Figure 9. - Continued. Radial variation of stator blade-element characteristics.

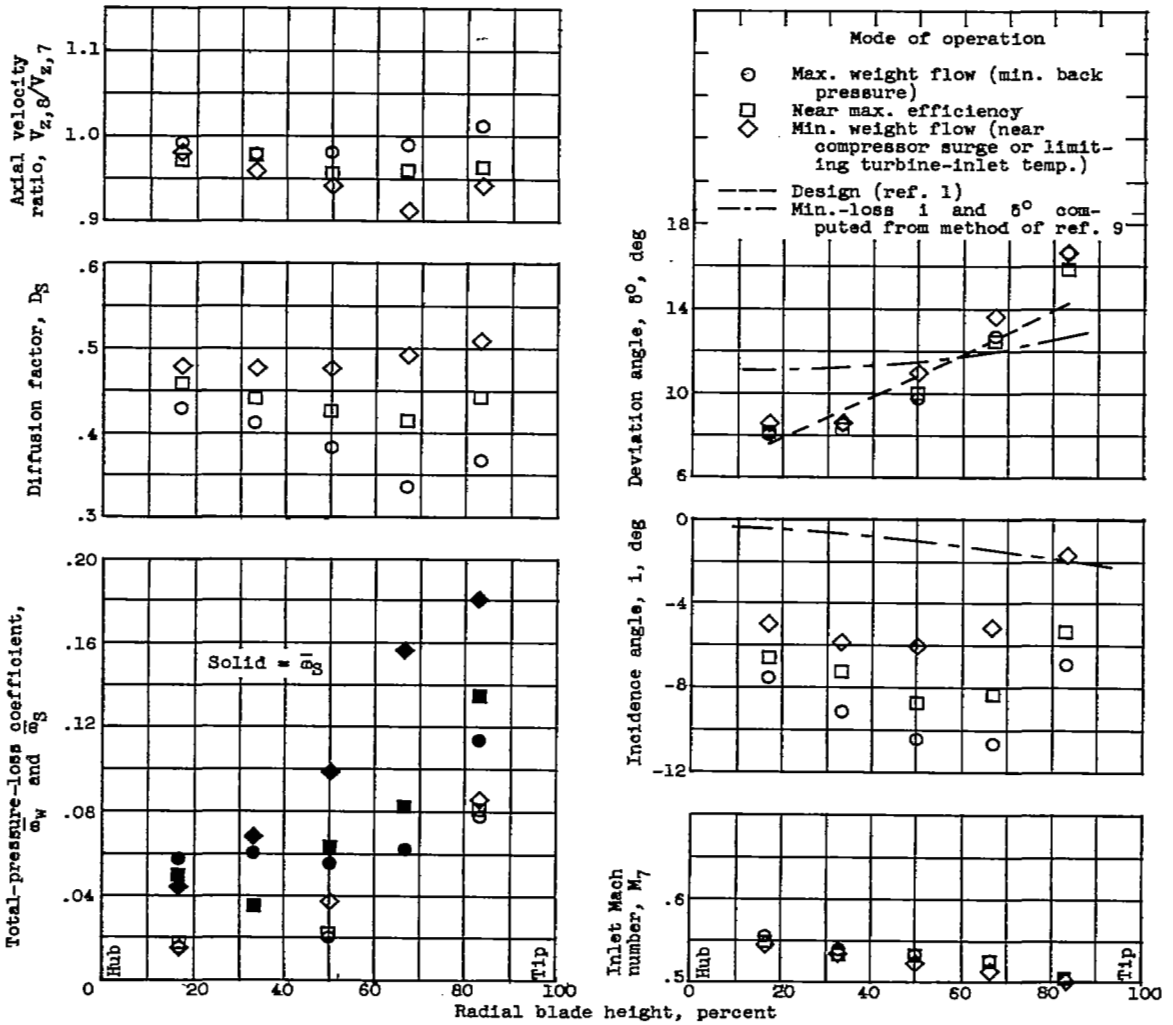

(3) Third-stage stator.

(b) Continued. Equivalent speed, 80-percent design.

Figure 9. - Continued. Radial variation of stator-blade-element characteristics.

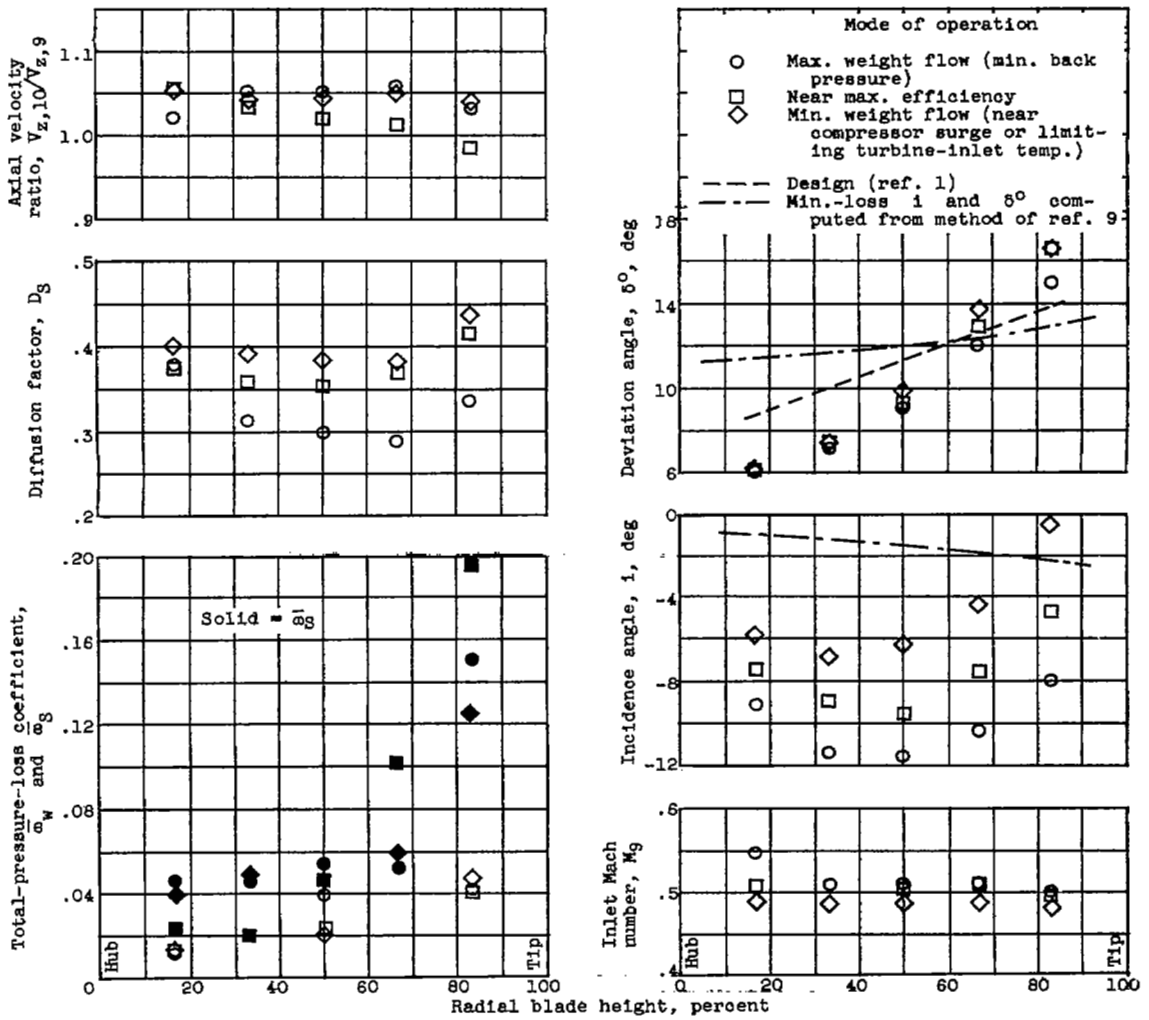

(4) Fourth-stage stator.

(b) Continued. Equivalent speed, 80-percent design.

Figure 9. - Continued. Radial variation of stator blade-element characteristics.

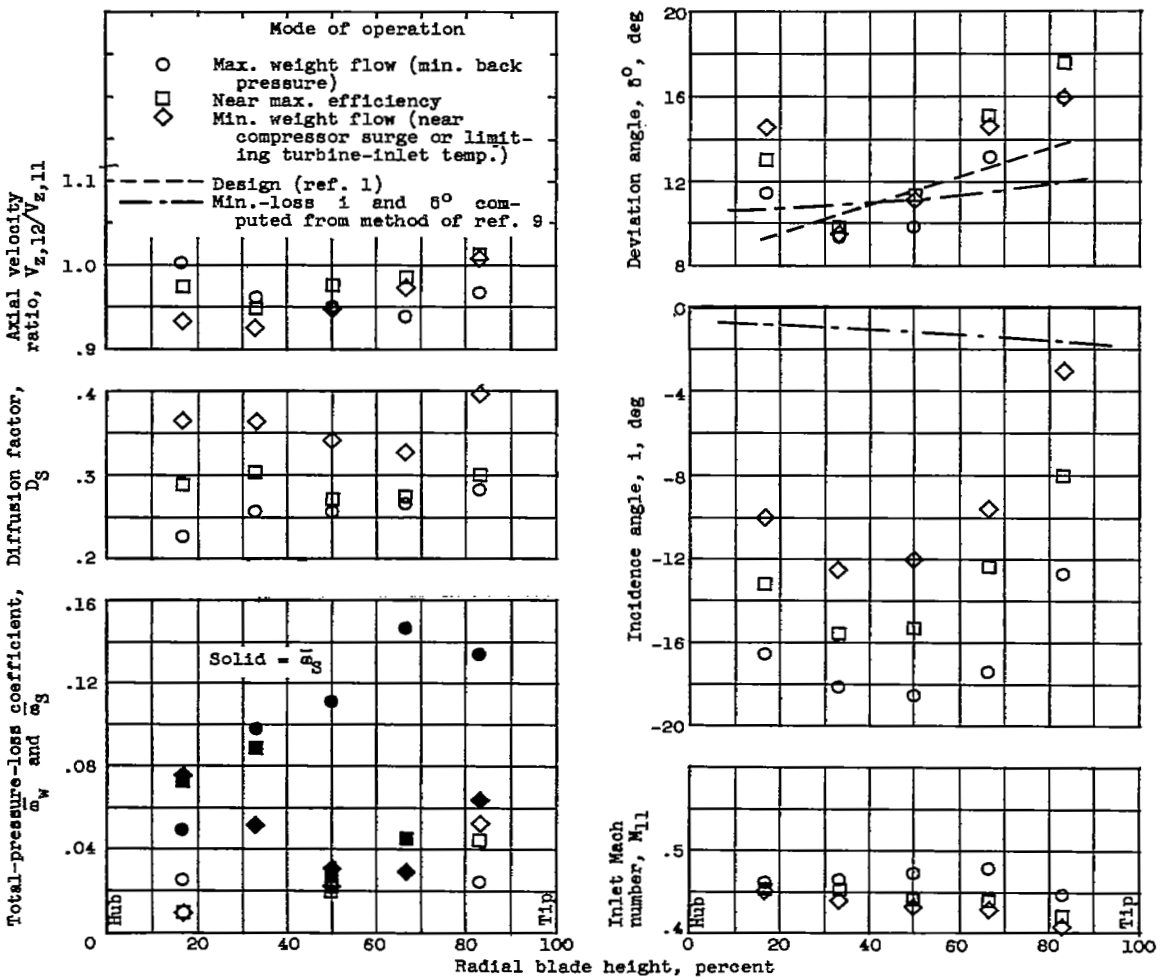

(5) Fifth-stage stator.

(b) Concluded. Equivalent speed, 80-percent design.

Figure 9. - Continued. Radial variation of stator blade-element characteristics.

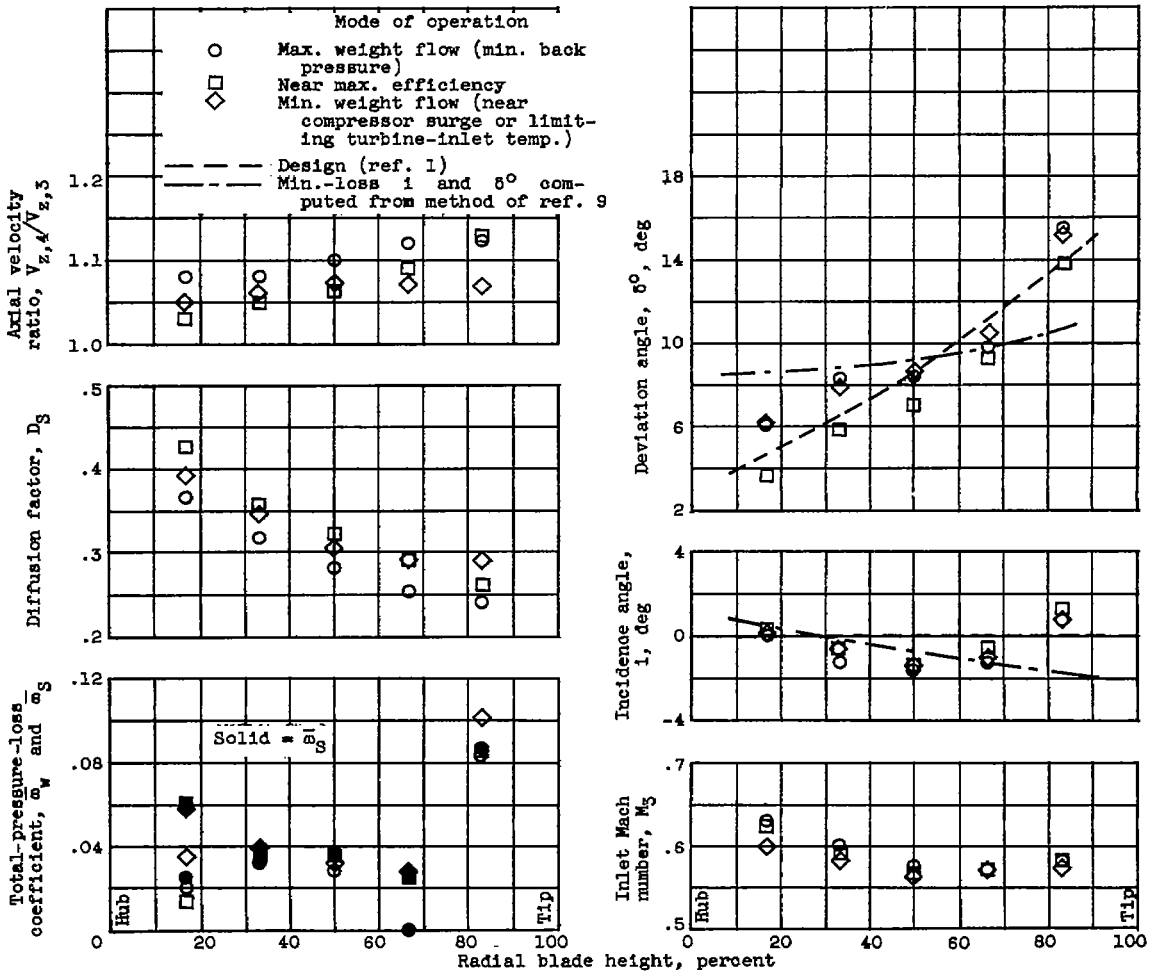

(l) First-stage stator.

(c) Equivalent speed, 90-percent design.

Figure 9. - Continued. Radial variation of stator blade-element characteristics.

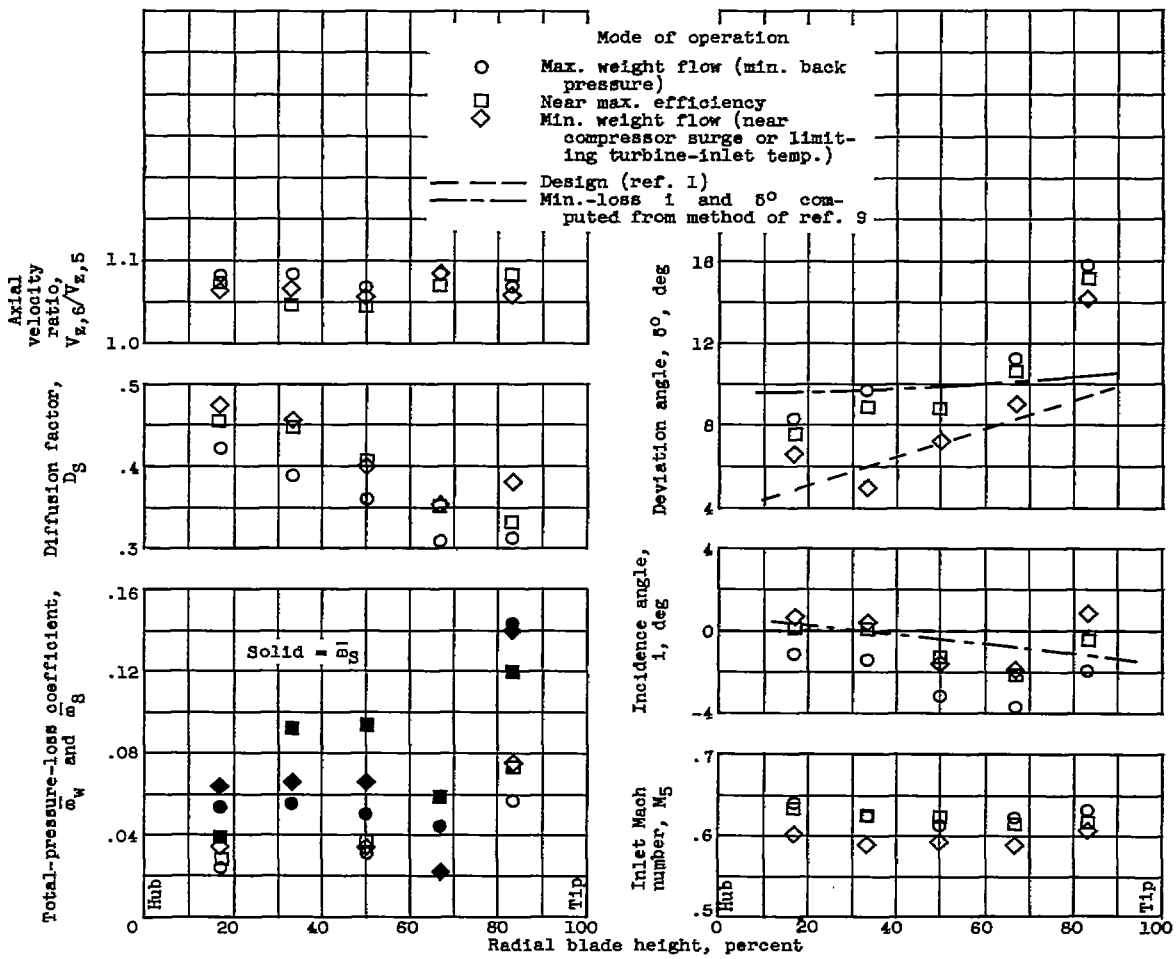

(2) Second-stage stator.

(c) Continued. Equivalent speed, 90-percent design.

Figure 9. - Continued. Radial variation of stator blade-element characteristics.

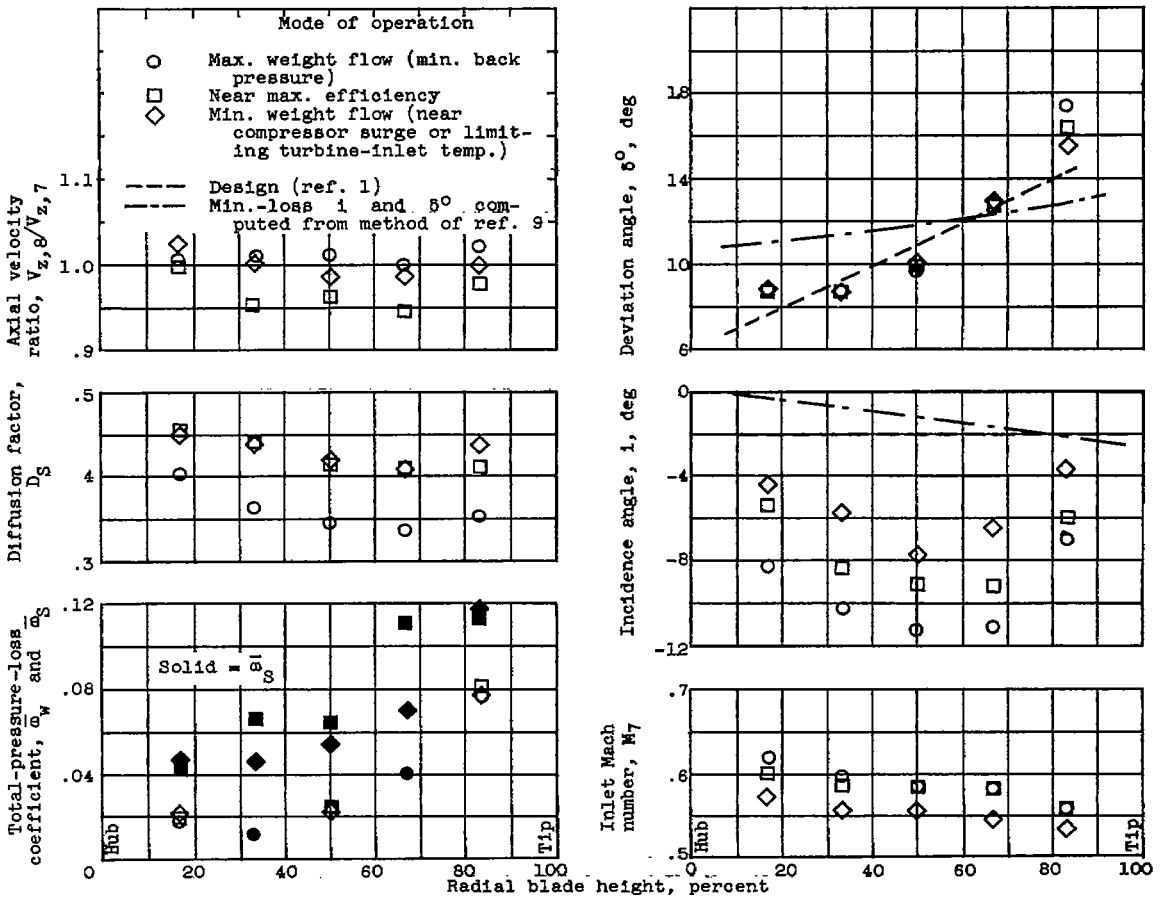

(3) Third-stage stator.

(c) Continued. Equivalent speed, 90-percent design.

Figure 9. - Continued. Radial variation of stator blade-element characteristics.

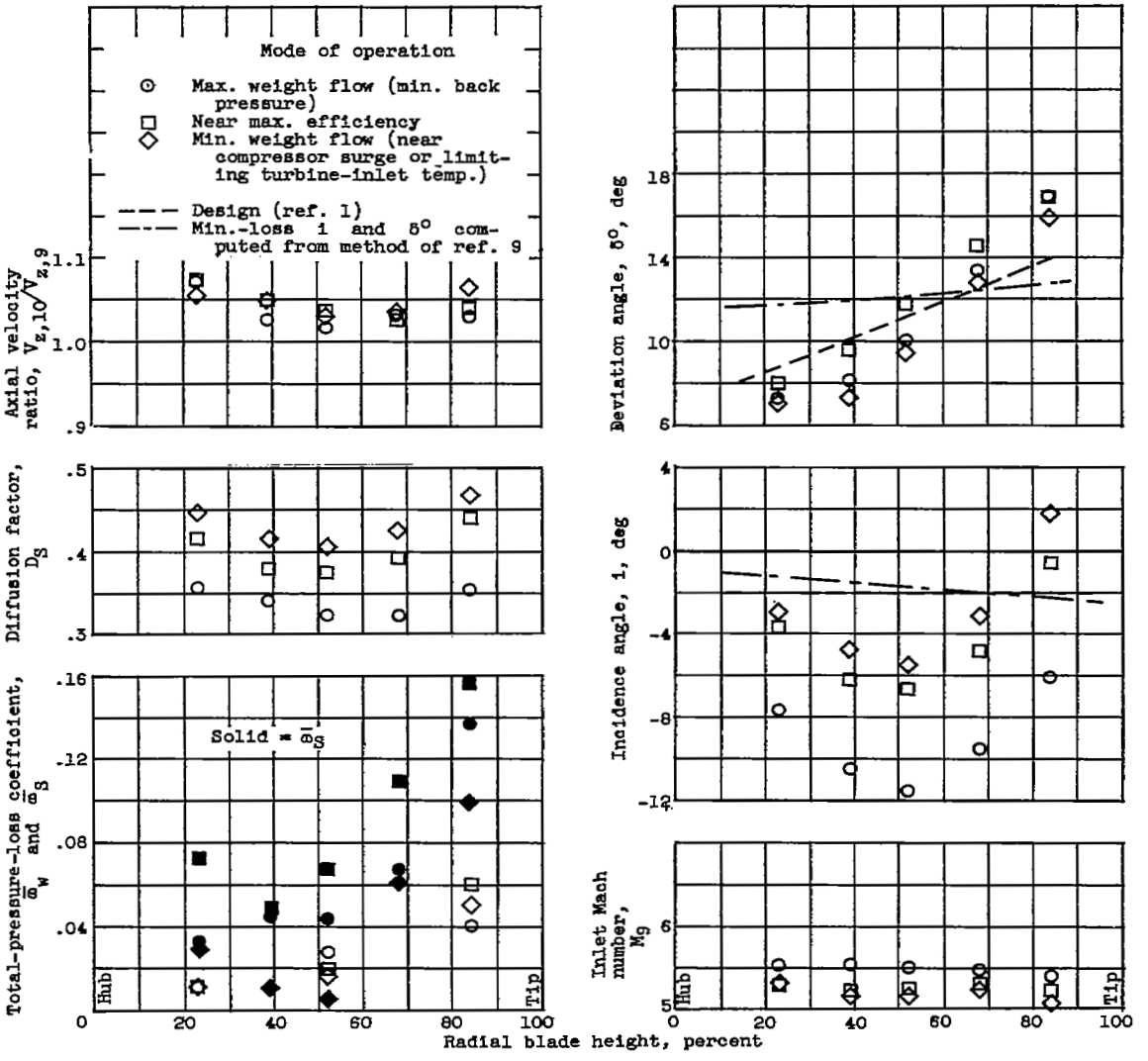

(4) Fourth-stage stator.

(c) Continued. Equivalent speed, 90-percent design.

Figure 9. - Continued. Radial variation of stator blade-element characteristics.

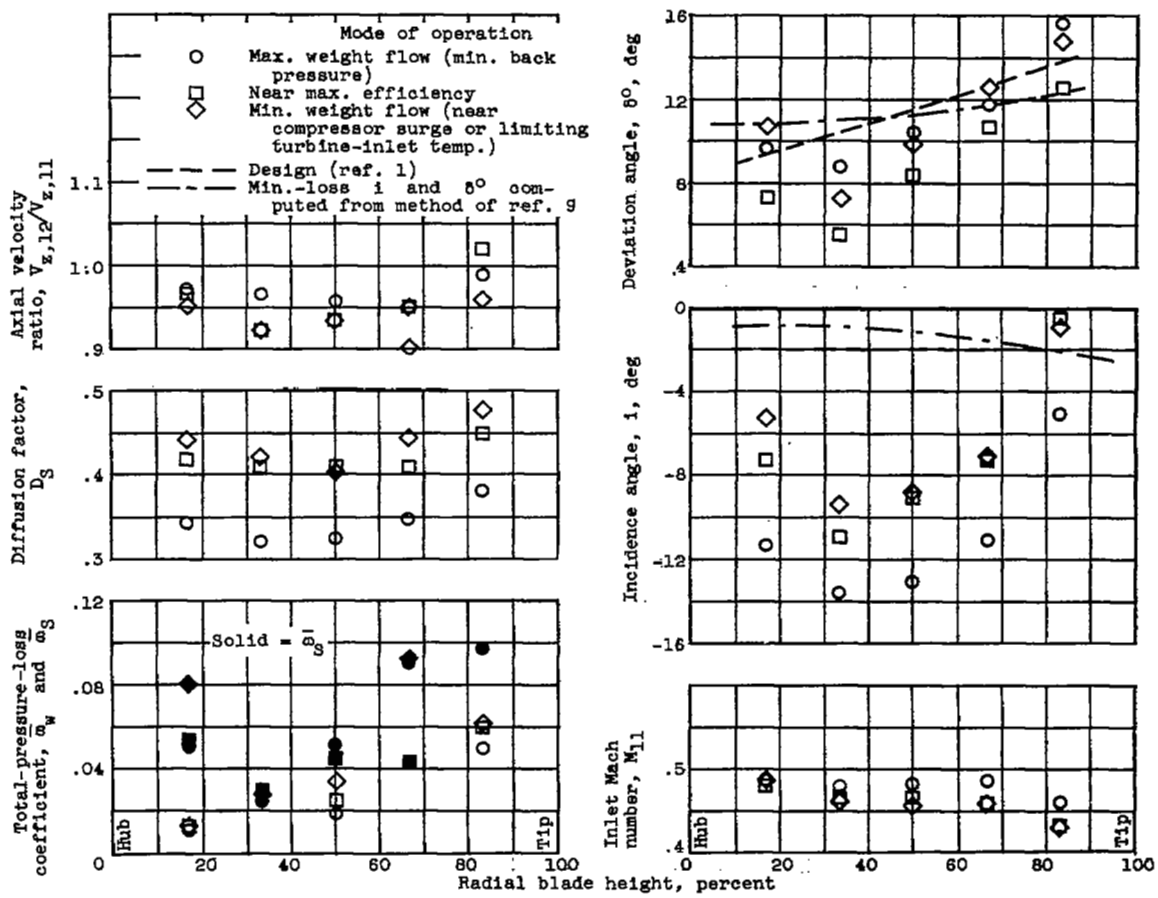

(5) Fifth-stage stator.

(c) Concluded. Equivalent speed, 90-percent design.

Figure 9. - Continued. Radial variation of stator blade-element characteristics.

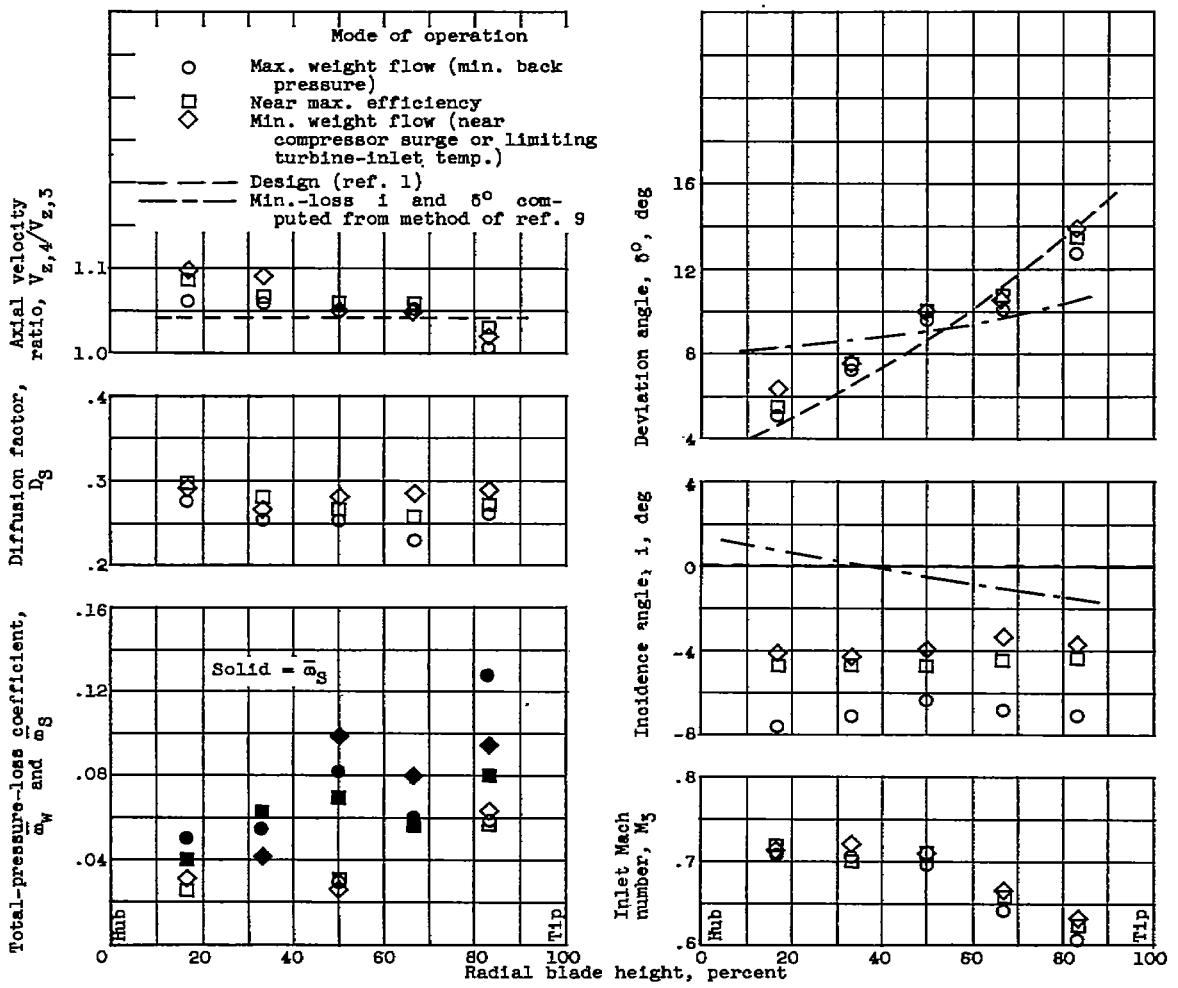

(1) First-stage stator.

(d) Equivalent speed, 100-percent design.

Figure 9. - Continued. Radial variation of stator blade-element characteristics.

[redacted]

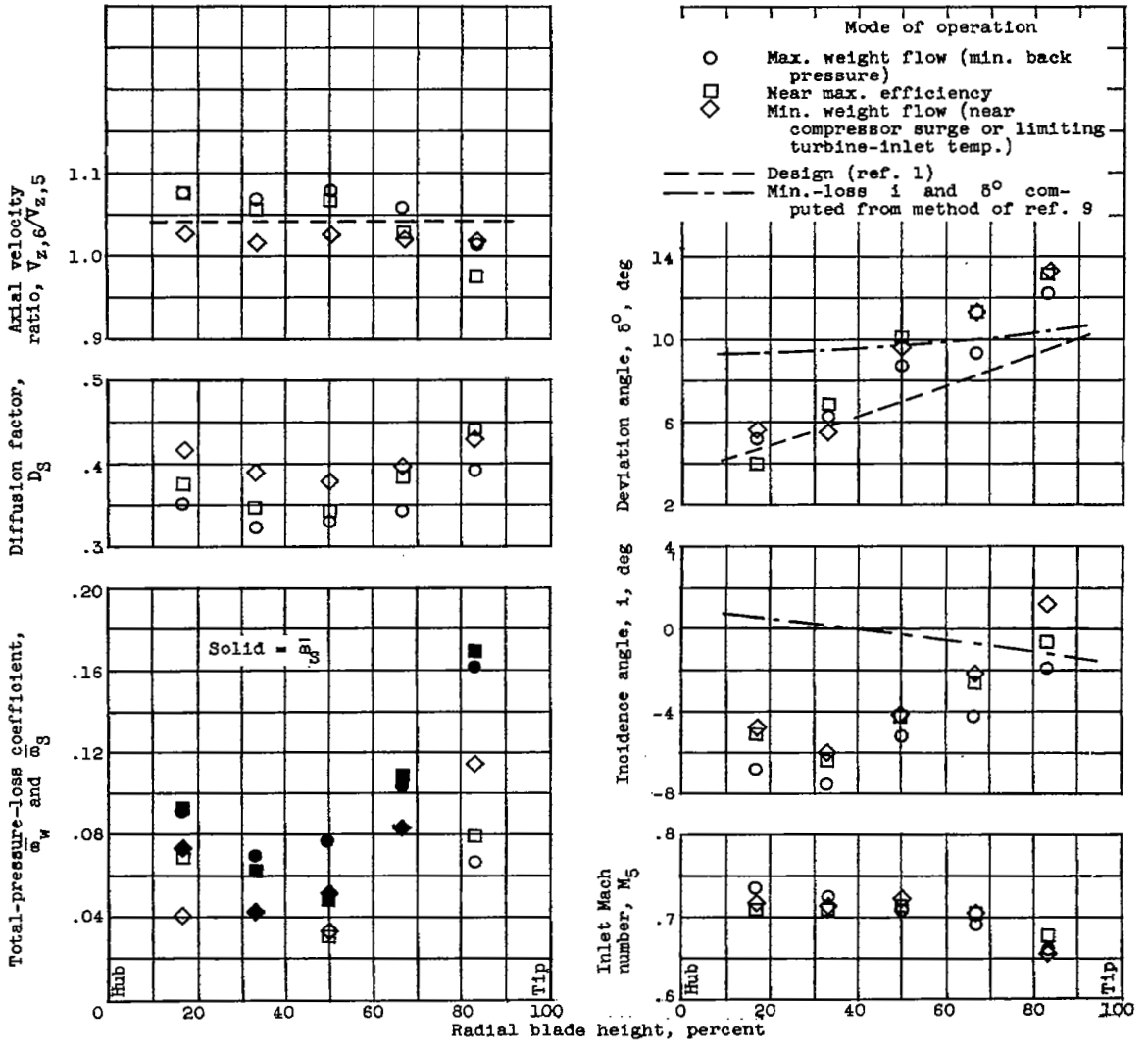

(2) Second-stage stator.

(d) Continued. Equivalent speed, 100-percent design.

Figure 9. - Continued. Radial variation of stator blade-element characteristics.

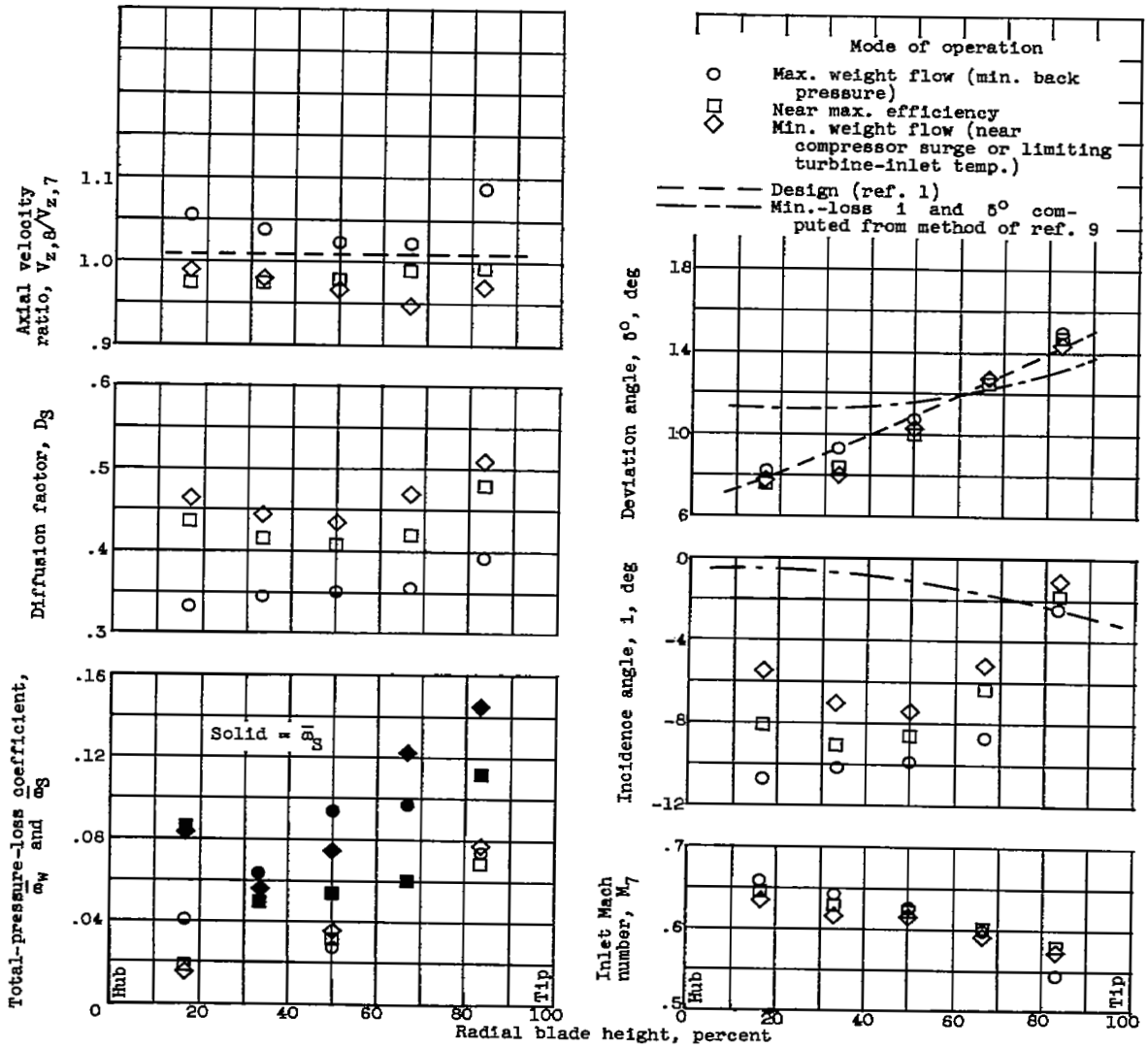

(3) Third-stage stator.

(d) Continued. Equivalent speed, 100-percent design.

Figure 9. - Continued. Radial variation of stator blade-element characteristics.

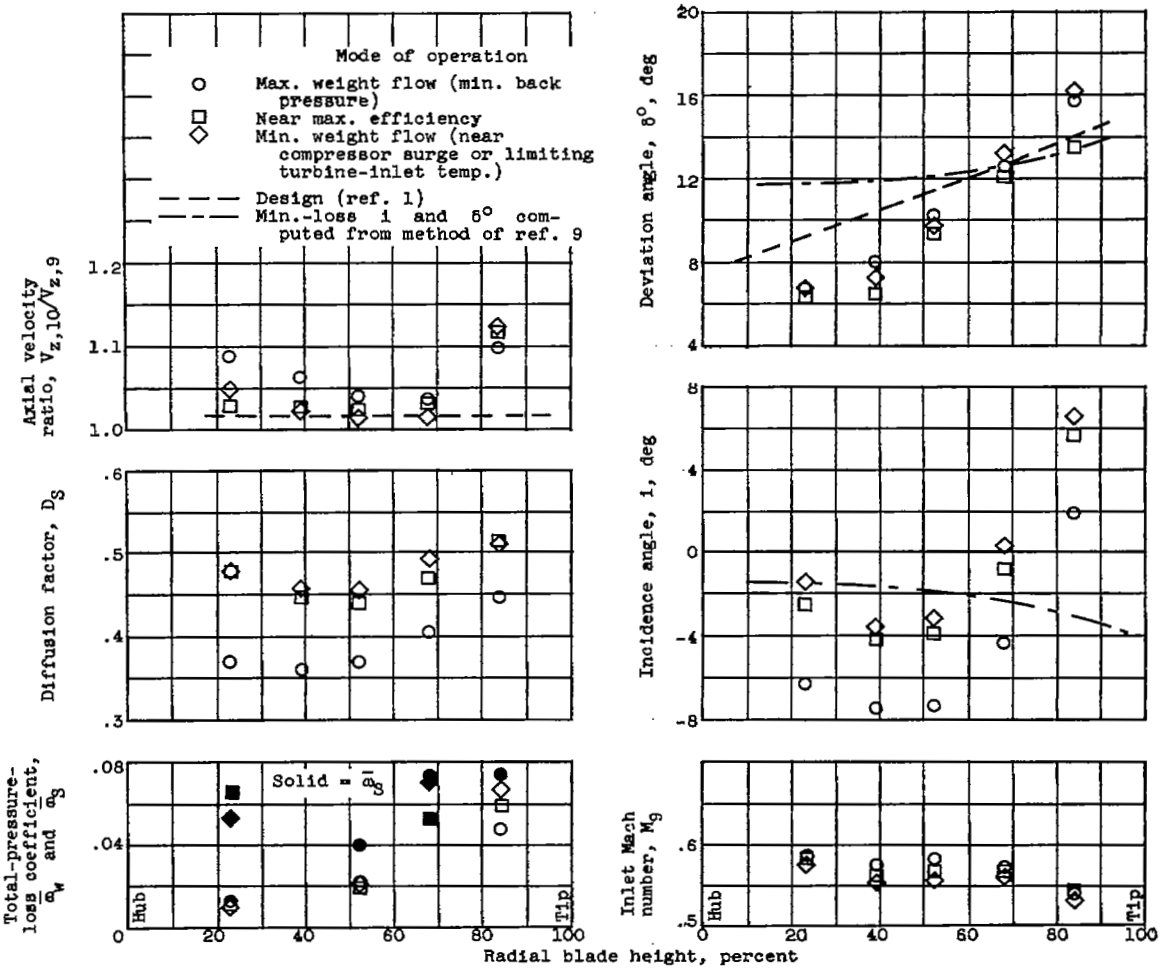

(4) Fourth-stage stator.

(d) Continued. Equivalent speed, 100-percent design.

Figure 9. - Continued. Radial variation of stator blade-element characteristics.

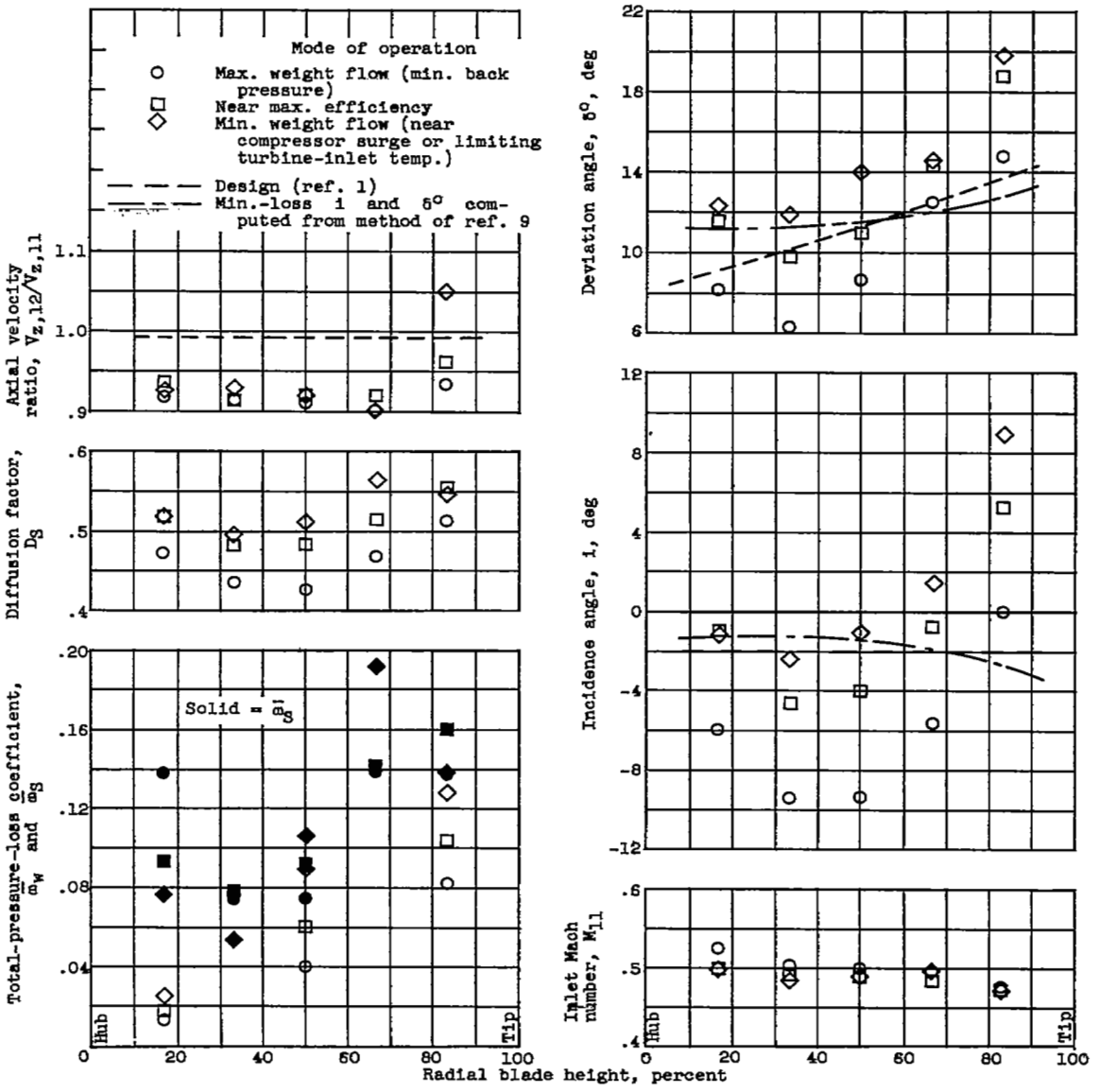

(5) Fifth-stage stator.

(d) Concluded. Equivalent speed, 100-percent design.

Figure 9. - Concluded. Radial variation of stator blade-element characteristics.

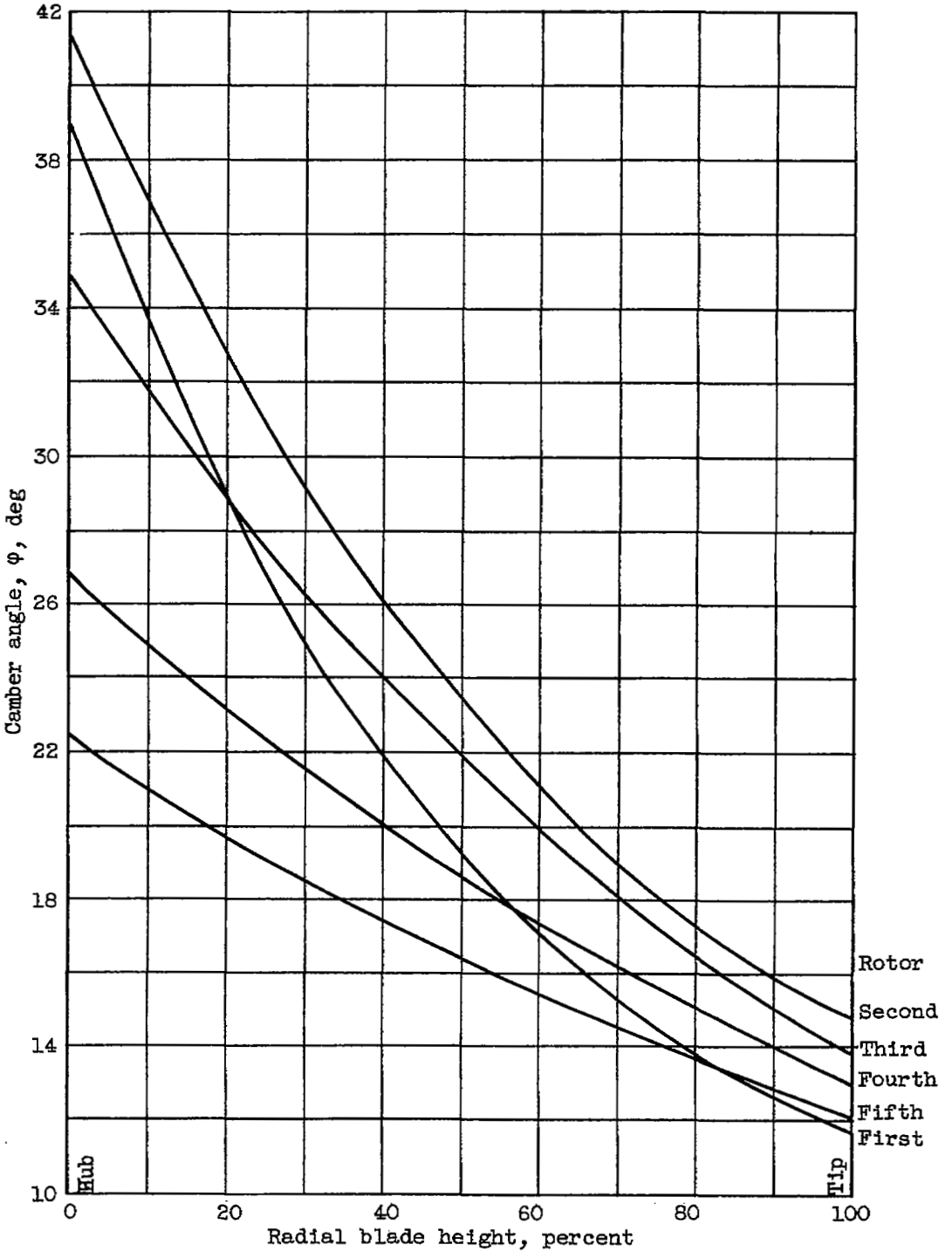

(a) Rotors.

Figure 10. - Radial distribution of blade camber angles.

[redacted]

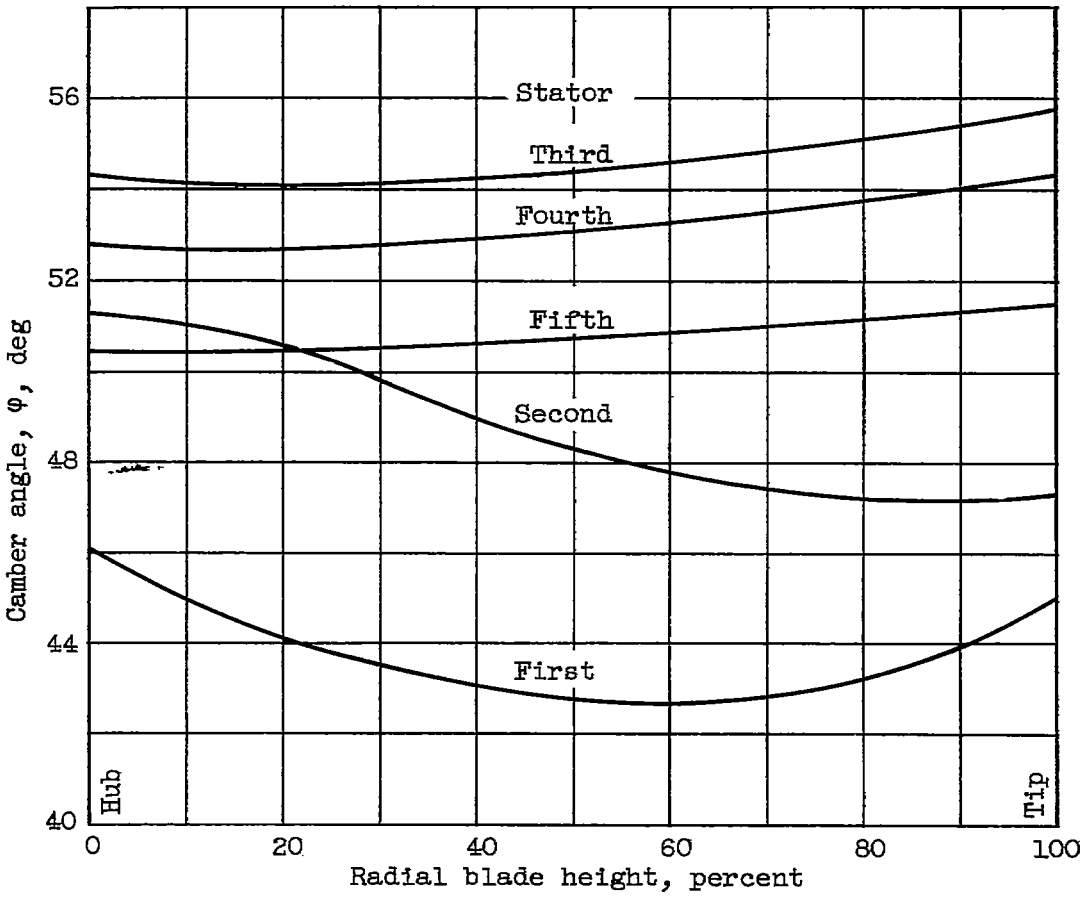

(b) Stators.

Figure 10. - Concluded. Radial distribution of blade camber angles.

[redacted]

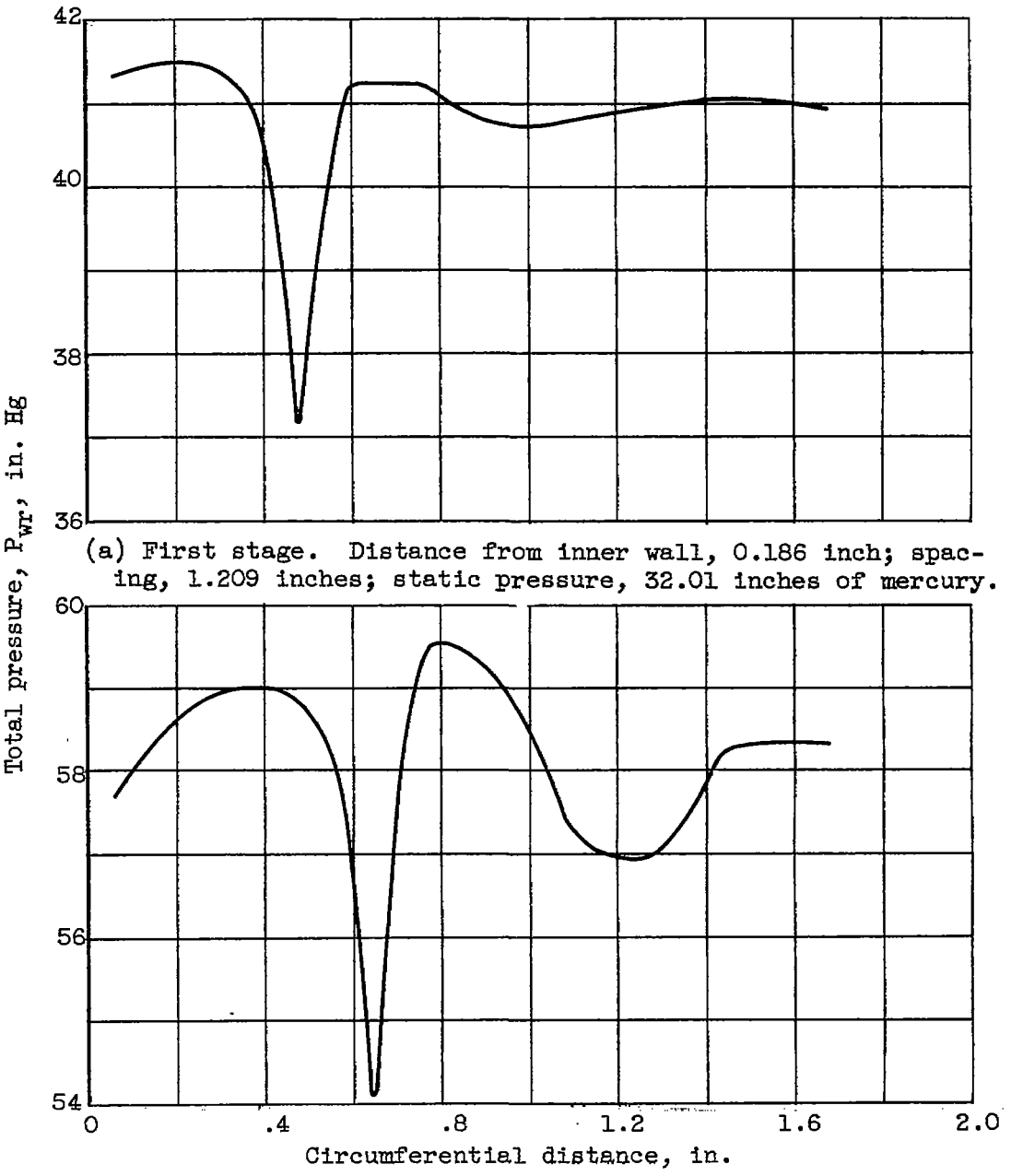

(a) First stage. Distance from inner wall, 0.186 inch; spacing, 1.209 inches; static pressure, 32.01 inches of mercury.

(b) Second stage. Distance from inner wall, 0.249 inch; spacing, 1.184 inches; static pressure, 47.76 inches of mercury.

Figure 11. - Circumferential variation of total pressure measured at exit of stator blade row. Equivalent speed, 100-percent design.

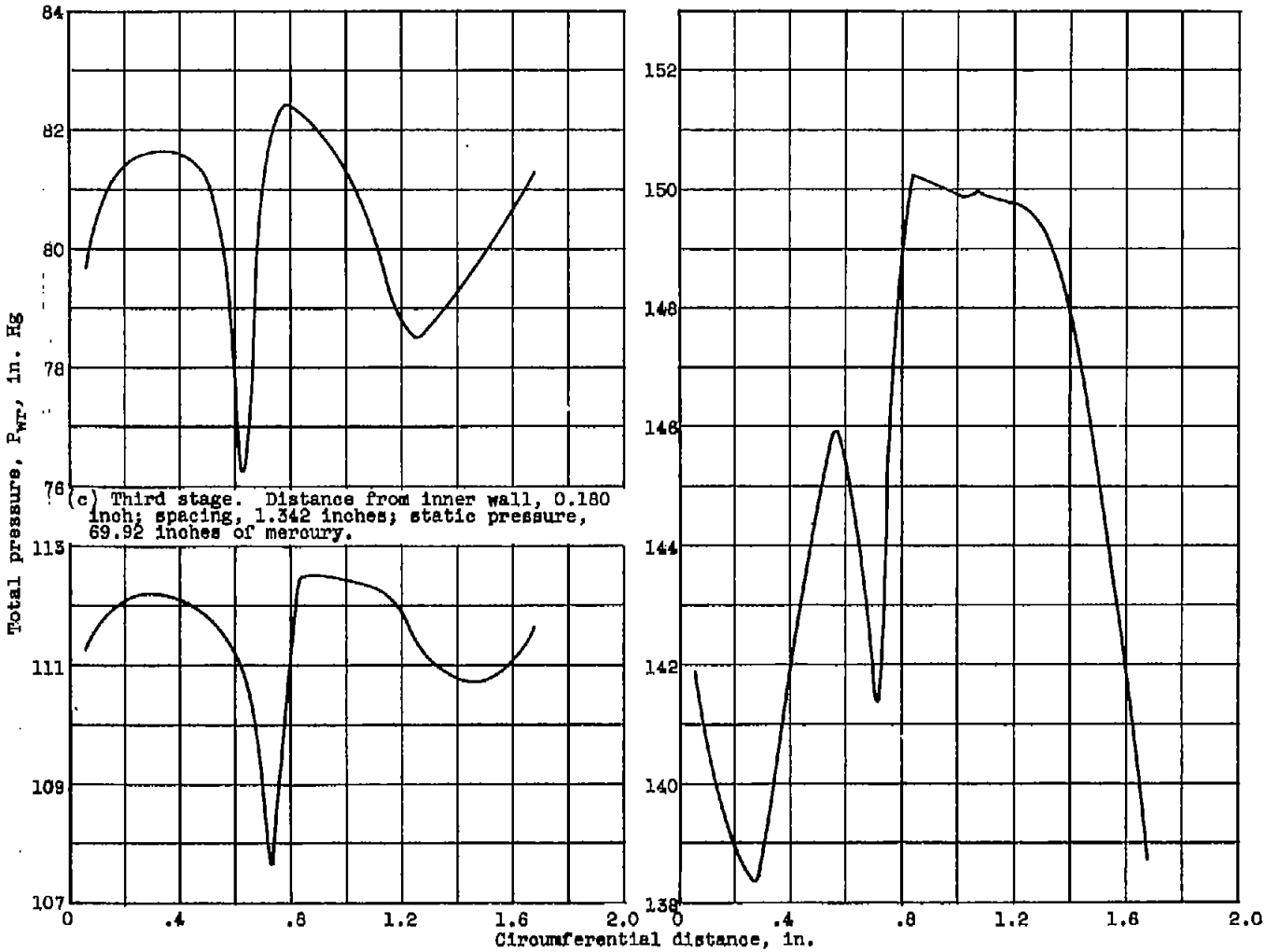

(c) Third stage. Distance from inner wall, 0.180 inch; spacing, 1.342 inches; static pressure, 69.92 inches of mercury.

(d) Fourth stage. Distance from inner wall, 0.286 inch; spacing, 1.466 inches; static pressure, 97.32 inches of mercury.

(e) Fifth stage. Distance from inner wall, 0.150 inch; spacing, 1.508 inches; static pressure, 133.98 inches of mercury.

Figure 11. - Concluded. Circumferential variation of total pressure measured at exit of stator blade row. Equivalent speed, 100-percent design.

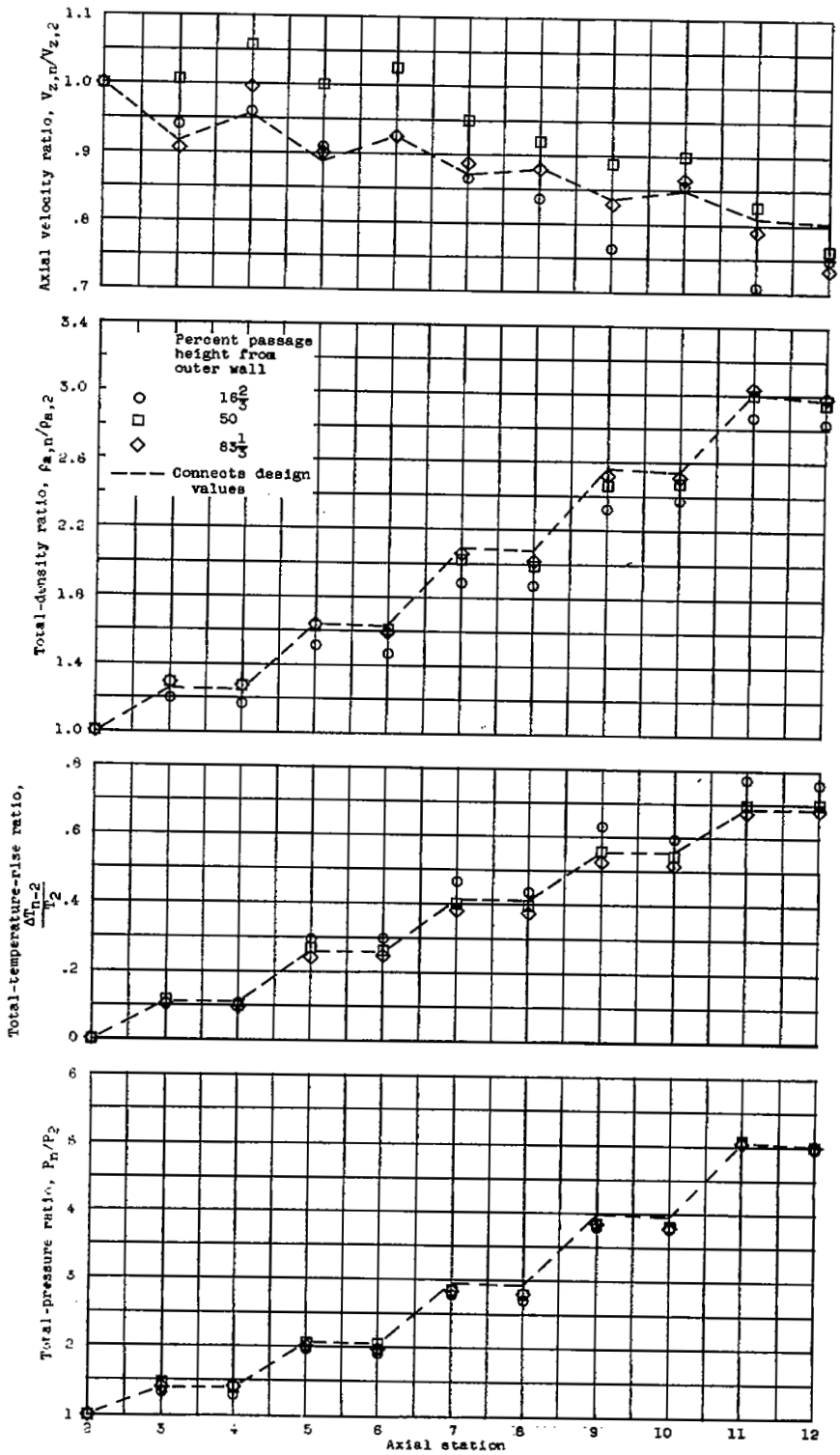

Figure 12. - Comparison of measured over-all performance at successive blade rows with values used in design.

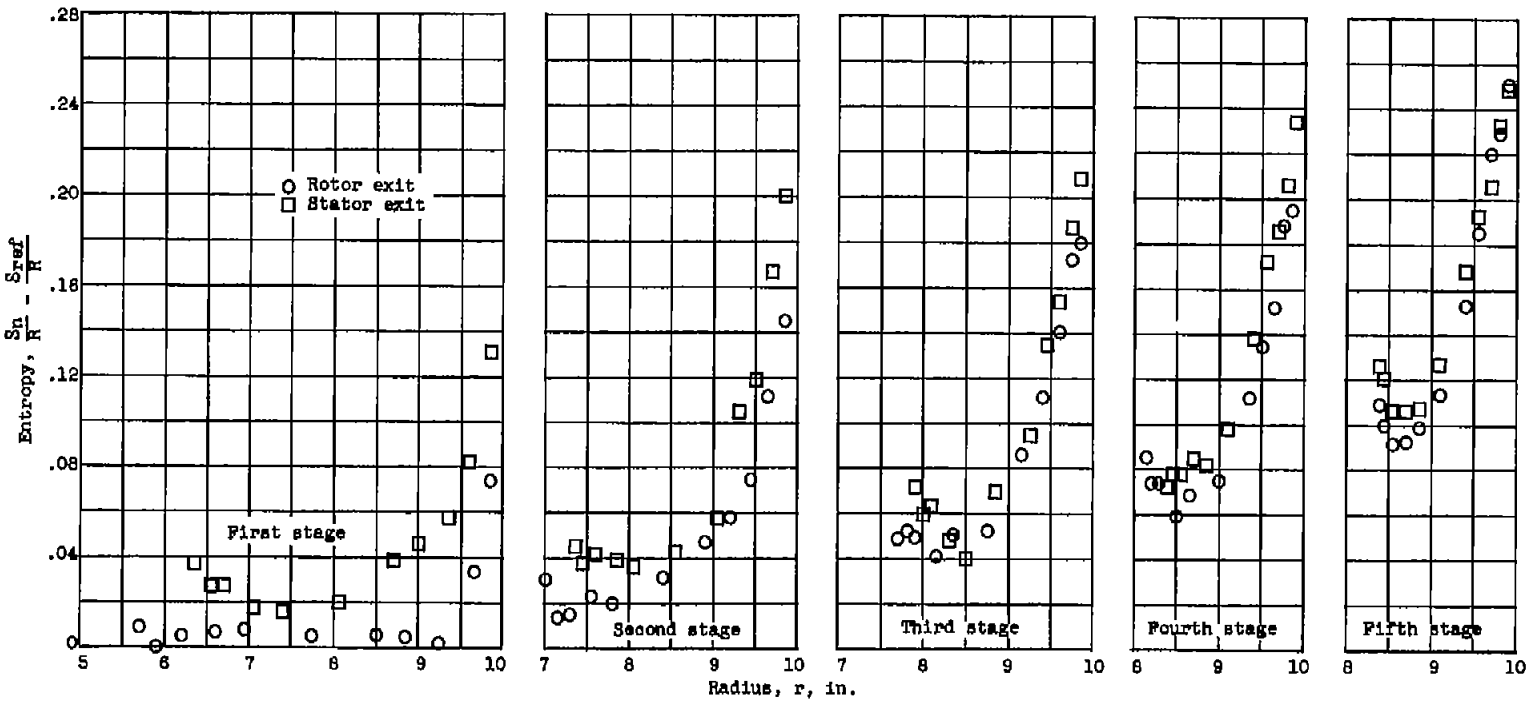

(a) Equivalent speed, 80-percent design. Operation near peak efficiency.

Figure 13. - Radial variation of entropy measured behind each blade row of five-stage transonic compressor.

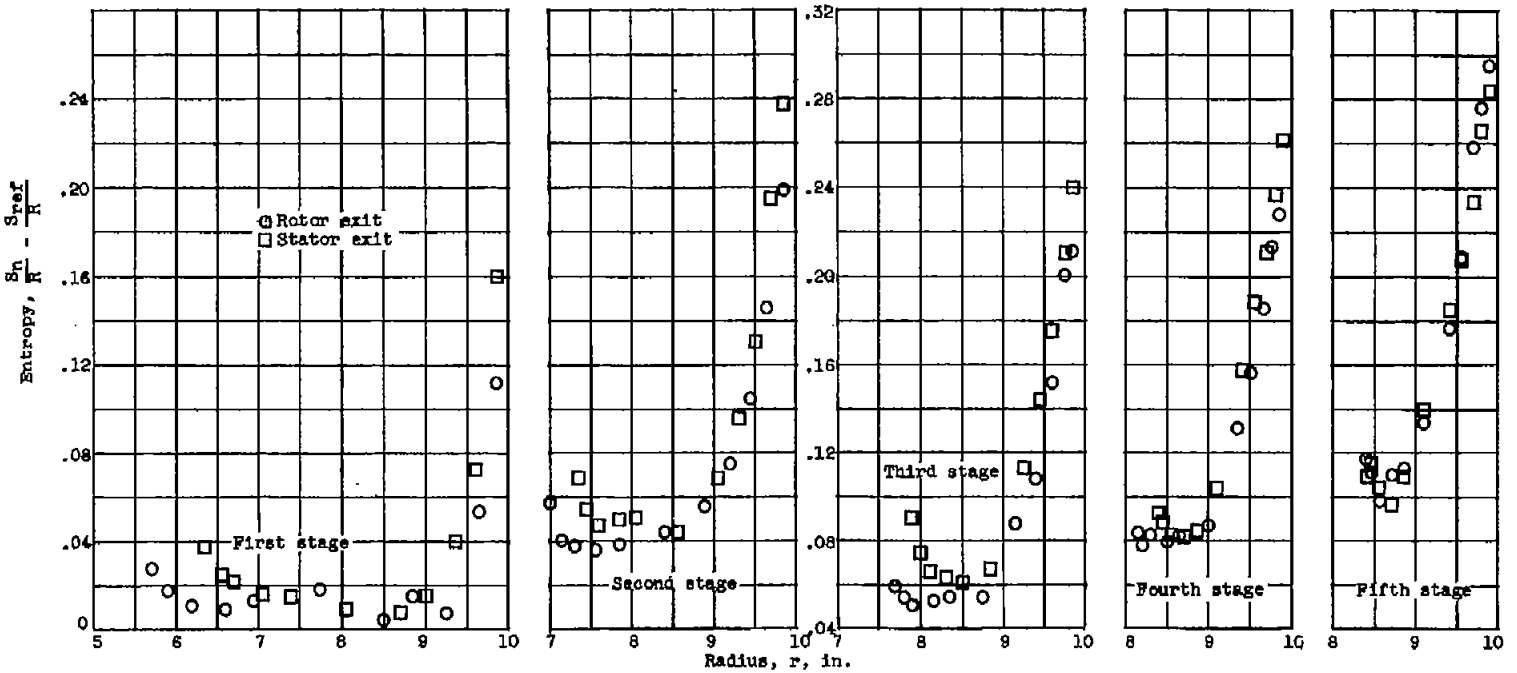

(b) Equivalent speed, 90-percent design. Operation near peak efficiency.

Figure 13. - Continued. Radial variation of entropy measured behind each blade row of five-stage transonic compressor.

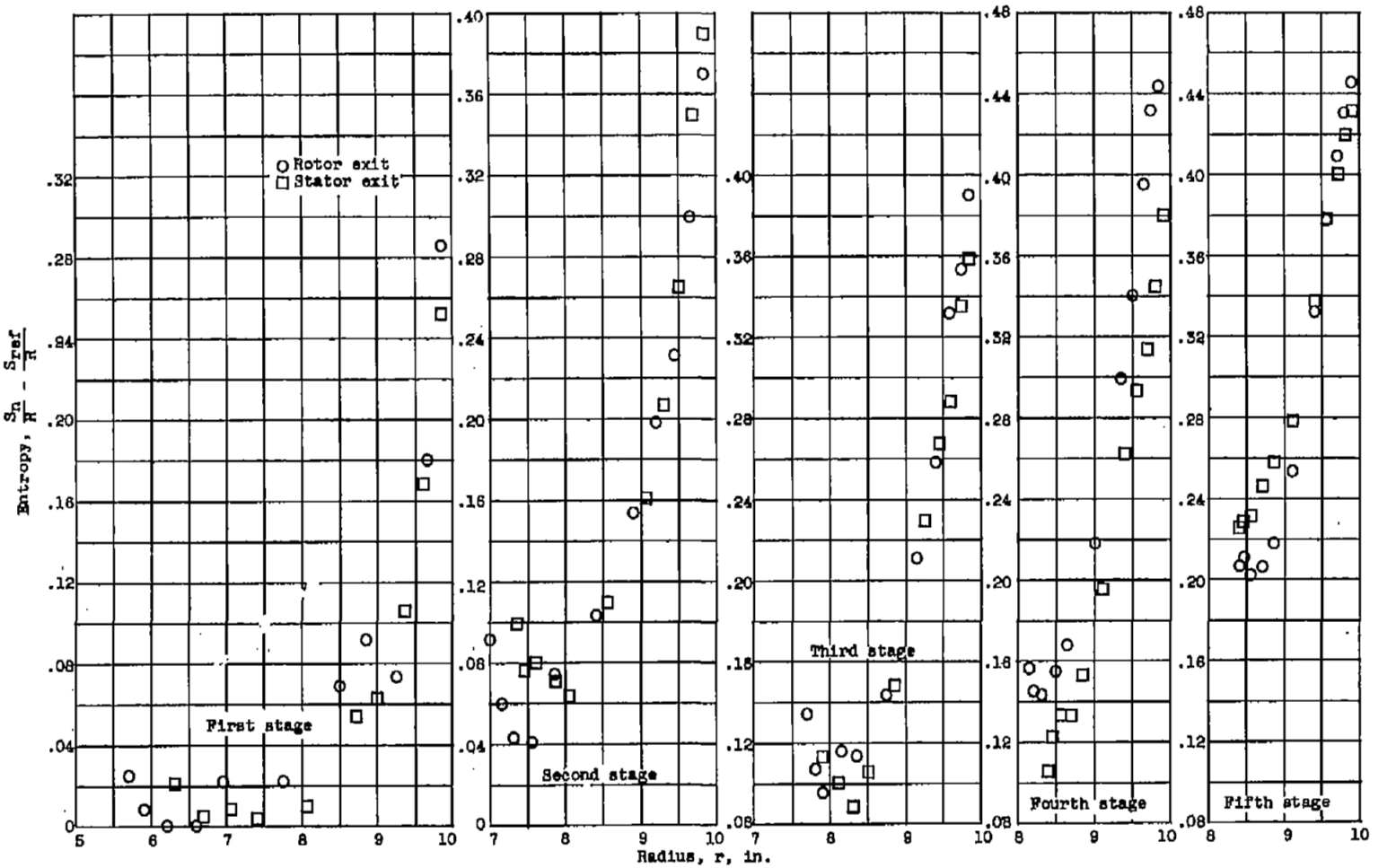

(c) Equivalent speed, 100-percent design. Operation at design pressure ratio.

Figure 13. - Concluded. Radial variation of entropy measured behind each blade row of five-stage transonic compressor.

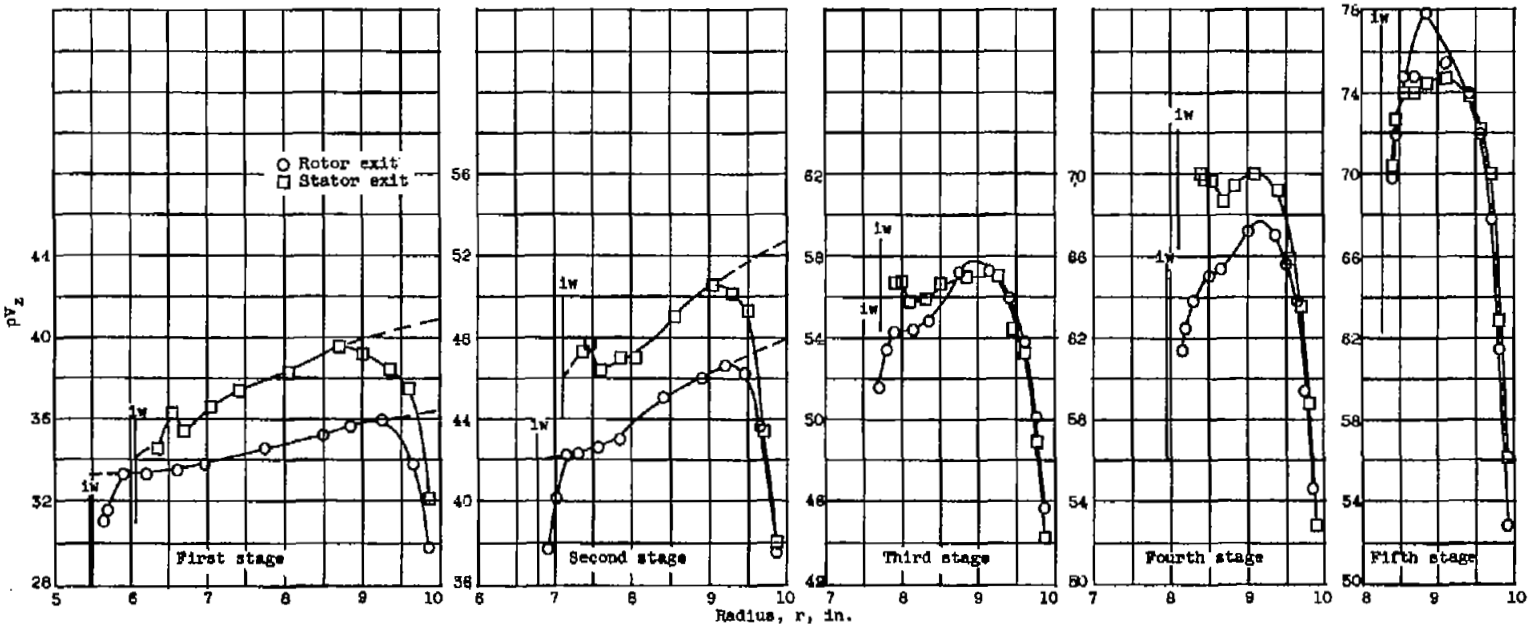

(a) Equivalent speed, 80-percent design. Operation near peak efficiency.

Figure 14 - Radial distributions of ρV_z product. (Outer wall constant at 10 in.; lw = inner wall.)

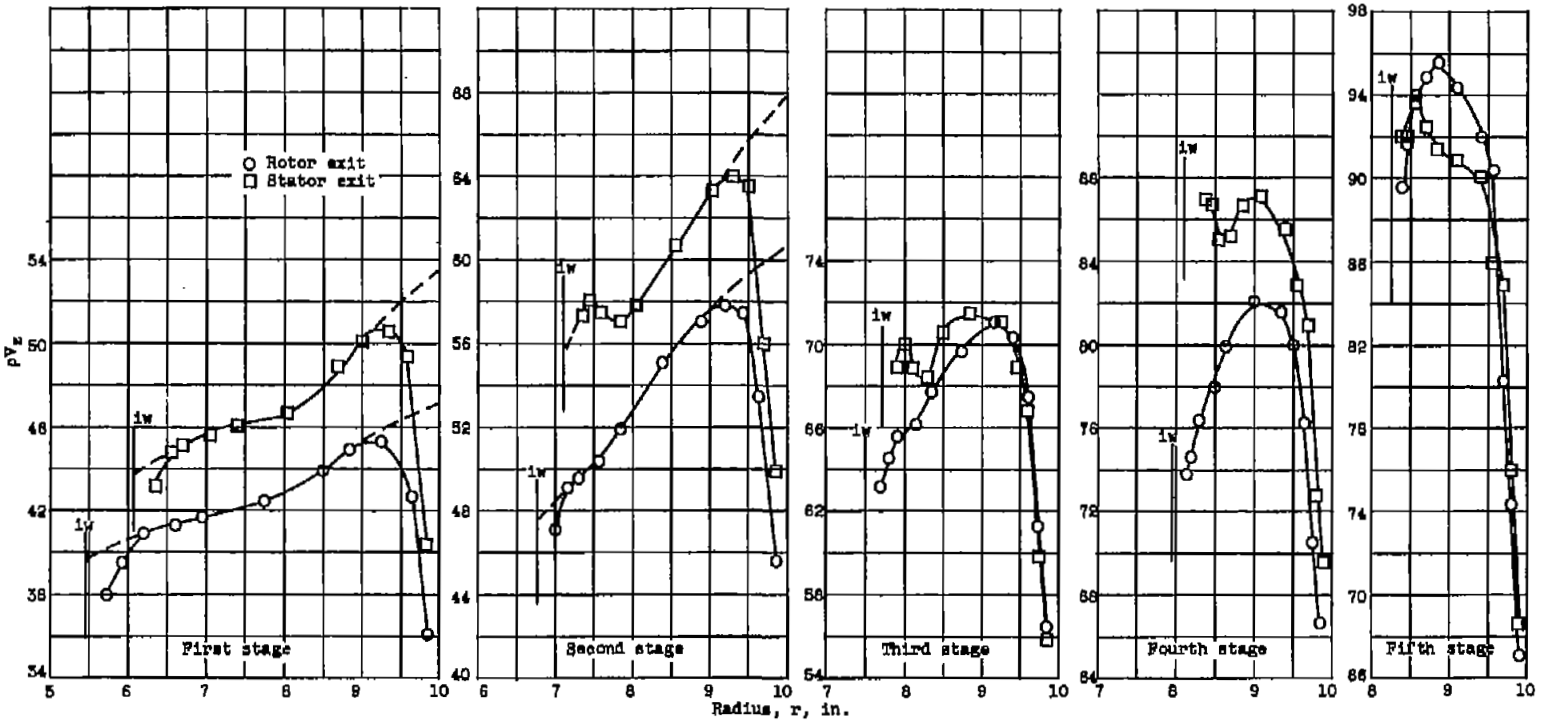

(b) Equivalent speed, 90-percent design. Operation near peak efficiency.

Figure 14. - Continued. Radial distributions of ρV_z product. (Outer wall constant at 10 in.; iw = inner wall.)

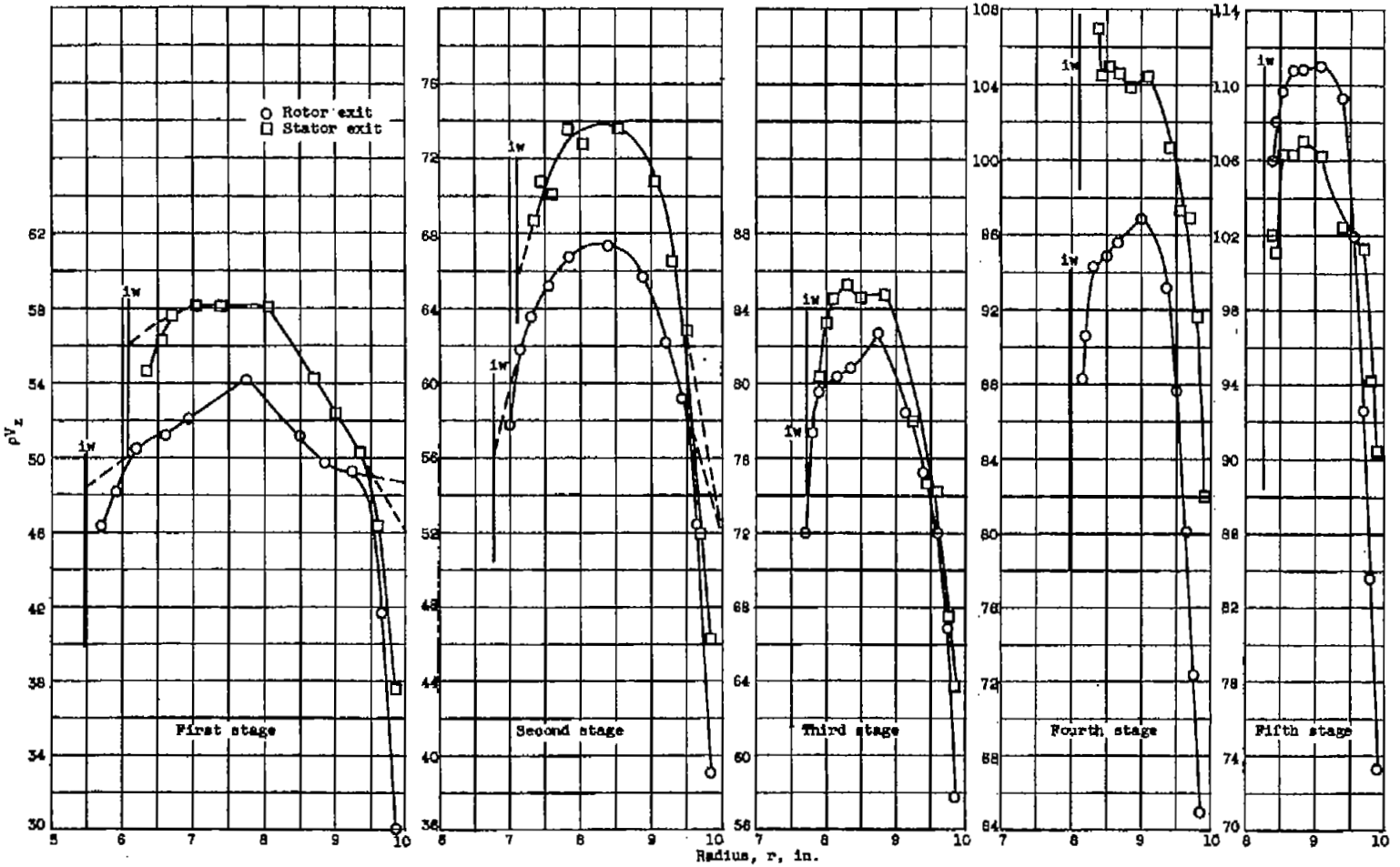

(c) Equivalent speed, 100-percent design. Operation at design pressure ratio.

Figure 14. - Concluded. Radial distributions of ρV_z product. (Outer wall constant at 10 in.; iw = inner wall.)

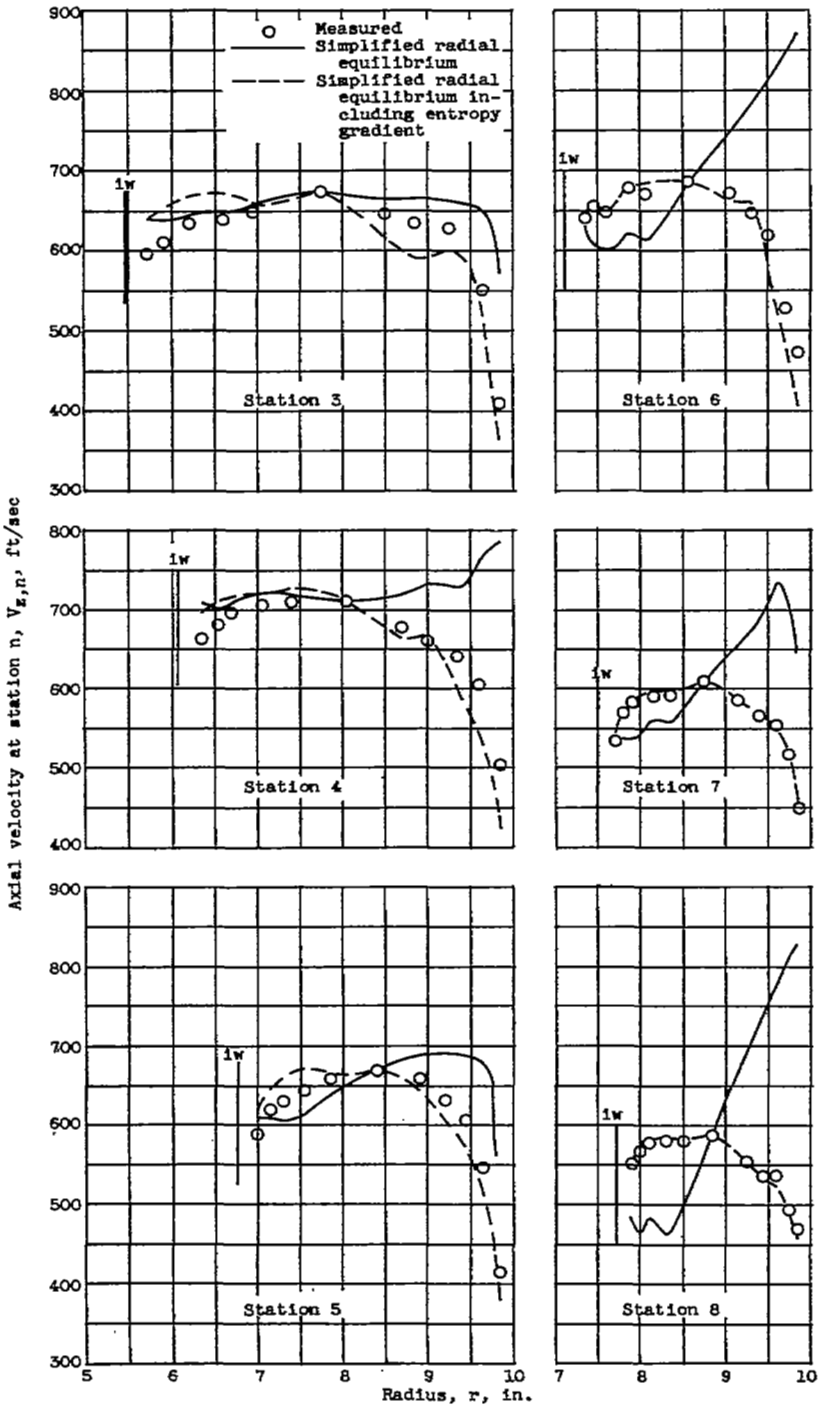

(a) Stations 3 to 8.

Figure 15. - Comparison of radial distribution of measured axial velocities with axial velocities computed from simplified-radial-equilibrium equations. Equivalent speed, 100-percent design; operation at design pressure ratio. (Outer wall constant at 10 in.; iw = inner wall.)

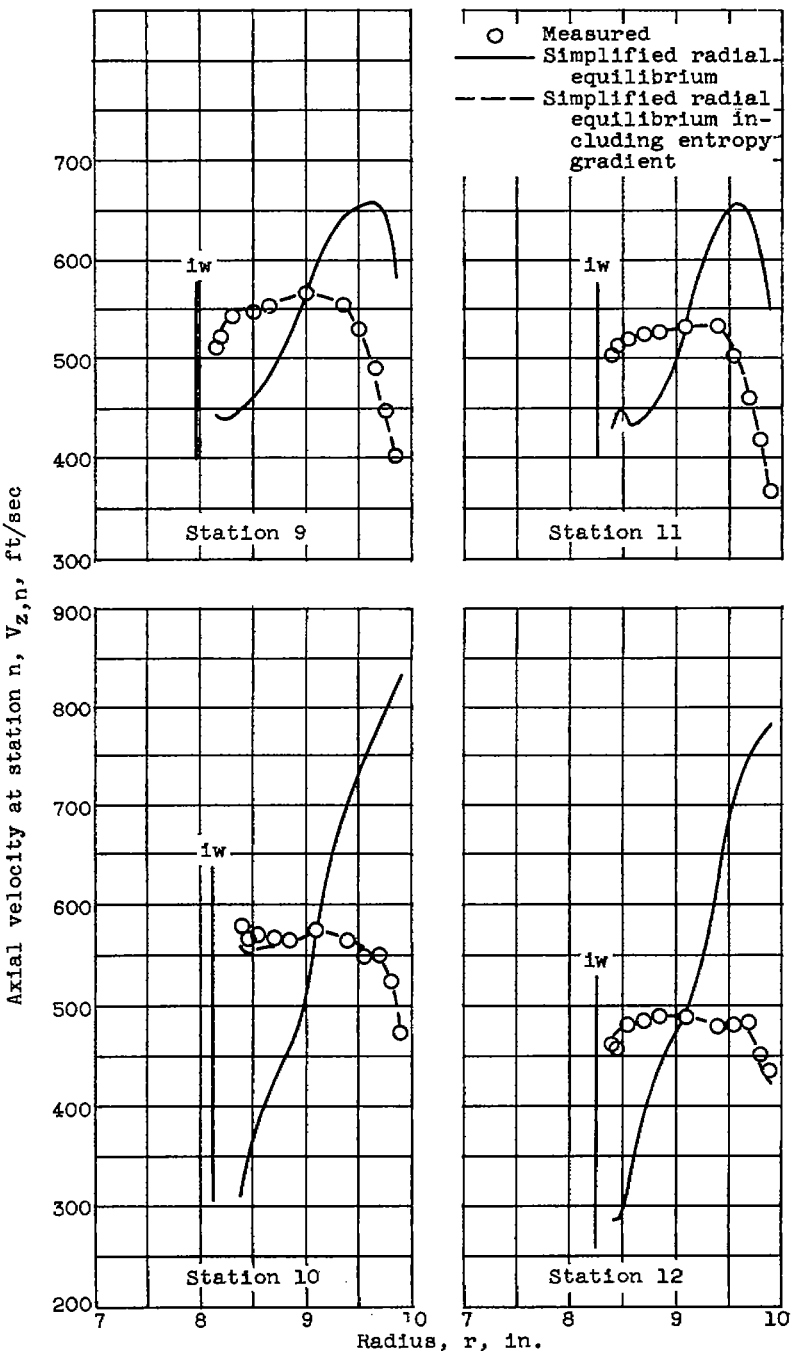

(b) Stations 9 to 12.

Figure 15. - Concluded. Comparison of radial distribution of measured axial velocities with axial velocities computed from simplified-radial-equilibrium equations. Equivalent speed, 100-percent design; operation at design pressure ratio. (Outer wall constant at 10 in; iw = inner wall.)